

THE FLORIDA STATE UNIVERSITY  
COLLEGE OF ARTS AND SCIENCES

A STUDY OF THE SINGLE NEUTRON KNOCKOUT REACTION FROM SI-26 AND

S-30

By

ROBERT R. REYNOLDS, JR.

A Dissertation submitted to the  
Department of Physics  
in partial fulfillment of the  
requirements for the degree of  
Doctor of Philosophy

Degree Awarded:  
Summer Semester, 2010

UMI Number: 3462402

All rights reserved

INFORMATION TO ALL USERS

The quality of this reproduction is dependent on the quality of the copy submitted.

In the unlikely event that the author did not send a complete manuscript and there are missing pages, these will be noted. Also, if material had to be removed, a note will indicate the deletion.



UMI 3462402

Copyright 2011 by ProQuest LLC.

All rights reserved. This edition of the work is protected against unauthorized copying under Title 17, United States Code.



ProQuest LLC.  
789 East Eisenhower Parkway  
P.O. Box 1346  
Ann Arbor, MI 48106 - 1346

The members of the committee approve the dissertation of Robert R. Reynolds, Jr. defended on June 30, 2010.

---

Paul Cottle  
Professor Directing Dissertation

---

Linda DeBrunner  
University Representative

---

Jorge Piekarewicz  
Committee Member

---

Ingo Wiedenhöver  
Committee Member

---

Hon-Kie Ng  
Committee Member

Approved:

---

Mark Riley, Chair, Department of Physics

---

Joseph Travis, Dean, College of Arts and Sciences

The Graduate School has verified and approved the above-named committee members.

To Mom and Dad, and especially my loving wife Kristin.

# TABLE OF CONTENTS

List of Tables . . . . .	vi
List of Figures . . . . .	vii
Abstract . . . . .	x
<b>1. INTRODUCTION . . . . .</b>	<b>1</b>
<b>2. THEORETICAL TREATMENT . . . . .</b>	<b>5</b>
2.1 The Shell Model . . . . .	5
2.1.1 Modern Shell Models . . . . .	6
2.1.2 Spectroscopic Information . . . . .	8
2.1.3 Electromagnetic Transitions . . . . .	18
2.2 Reaction Mechanism . . . . .	22
2.2.1 Single Nucleon Knockout Reactions . . . . .	22
<b>3. EXPERIMENTAL DETAILS . . . . .</b>	<b>26</b>
3.1 Rare Isotope Beam Production . . . . .	26
3.1.1 Coupled Cyclotron Facility . . . . .	26
3.1.2 A1900 Fragment Separator . . . . .	27
3.2 The S800 Spectrograph . . . . .	30
3.2.1 Analysis Line . . . . .	31
3.2.2 Spectrograph and Focal Plane Detectors . . . . .	31
3.2.3 Particle Identification . . . . .	39
3.2.4 Particle Detection Efficiency . . . . .	40
3.3 The Segmented High Purity Germanium Detector Array (SeGA) . . . . .	50
3.3.1 Doppler Effects . . . . .	51
3.3.2 Energy Calibration . . . . .	56
3.3.3 Detection Efficiency . . . . .	58
3.3.4 Timing Signal . . . . .	61
3.4 Data Acquisition Triggers and Signal Timing . . . . .	74
<b>4. ANALYSIS AND CONCLUSIONS . . . . .</b>	<b>78</b>
4.1 Analysis Procedure . . . . .	78
4.1.1 Cross Section Calculation . . . . .	78
4.1.2 $\gamma$ -Ray Analysis . . . . .	82

4.1.3	Longitudinal Momentum Distribution . . . . .	86
4.2	Analysis of ${}^9\text{Be}({}^{26}\text{Si}, {}^{25}\text{Si}+\gamma)$ . . . . .	87
4.2.1	Inclusive Reaction Measurements . . . . .	88
4.2.2	$\gamma$ -Ray Analysis . . . . .	90
4.2.3	Longitudinal Momentum Distributions . . . . .	97
4.3	Analysis of ${}^9\text{Be}({}^{30}\text{S}, {}^{29}\text{S}+\gamma)$ . . . . .	102
4.3.1	Inclusive Reaction Measurements . . . . .	102
4.3.2	$\gamma$ -Ray Analysis . . . . .	105
4.3.3	Longitudinal Momentum Distributions . . . . .	108
<b>5.</b>	<b>DISCUSSION AND CONCLUSIONS</b> . . . . .	<b>120</b>
	REFERENCES . . . . .	125
	BIOGRAPHICAL SKETCH . . . . .	131

## LIST OF TABLES

2.1	<sup>25</sup> Si Shell Model Energy Levels and $C^2S$ . . . . .	9
2.2	<sup>29</sup> S Shell Model Energy Levels and $C^2S$ . . . . .	9
2.3	<i>USDA</i> E&M Transition Calculations . . . . .	20
2.4	<i>USDB</i> E&M Transition Calculations . . . . .	21
2.5	<sup>9</sup> Be( <sup>26</sup> Si, <sup>25</sup> Si) Theoretical Cross Sections . . . . .	24
2.6	<sup>9</sup> Be( <sup>30</sup> S, <sup>29</sup> S) Theoretical Cross Sections . . . . .	24
3.1	Calibration Source Energy and Intensity . . . . .	57
3.2	Calibration Source Runs . . . . .	58
3.3	SeGA Photopeak Energy Resolution . . . . .	59
4.1	Expected <sup>25</sup> Si Energy Levels . . . . .	88
4.2	<sup>26</sup> Si Beam Normalization . . . . .	88
4.3	Expected <sup>29</sup> S Energy Levels . . . . .	102
4.4	<sup>30</sup> S Beam Normalization . . . . .	103
4.5	<sup>29</sup> S $\gamma$ -ray Intensities . . . . .	106
5.1	Data Summary and Reduction Factors . . . . .	121
5.2	( $e, e'p$ ) Reduction Factors . . . . .	123
5.3	Proton Knockout Reduction Factors . . . . .	123
5.4	Neutron Knockout Reduction Factors . . . . .	124

# LIST OF FIGURES

2.1	Naive Shell Model Energy Levels . . . . .	11
2.2	$^{26}\text{Si}$ Filled Shells . . . . .	12
2.3	$^{30}\text{S}$ Filled Shells . . . . .	13
2.4	USD Parameterization States . . . . .	14
2.5	Spectroscopy Diagram . . . . .	15
2.6	$^{25}\text{Si}$ Shell Model Level Diagram . . . . .	16
2.7	$^{29}\text{S}$ Shell Model Level Diagram . . . . .	17
2.8	Single Nucleon Knockout Reaction Diagram . . . . .	25
3.1	Basic Cyclotron Diagram . . . . .	27
3.2	Coupled-Cyclotron Facility and A1900 Fragment Separator . . . . .	28
3.3	S800 Spectrometer . . . . .	30
3.4	S800 Focal Plane Detectors . . . . .	32
3.5	CRDC Pad Calibration . . . . .	34
3.6	CRDC Mask Diagram . . . . .	35
3.7	CRDC Mask Calibration . . . . .	36
3.8	CRDC X and Y Plots . . . . .	42
3.9	CRDC Dispersive Angle . . . . .	43
3.10	Ion Chamber $\Delta E$ for $^{26}\text{Si}$ . . . . .	44
3.11	Ion Chamber $\Delta E$ for $^{30}\text{S}$ . . . . .	45
3.12	TOF between XFP and OBJ for $^{26}\text{Si}$ . . . . .	46
3.13	TOF between XFP and OBJ for $^{30}\text{S}$ . . . . .	47

3.14	AFP Correction for TOF . . . . .	48
3.15	Effects of AFP Correction on PID Spectra . . . . .	49
3.16	SeGA's Crystal Segmentation. . . . .	53
3.17	Schematic of SeGA's Detector Rings. . . . .	54
3.18	SeGA Detector Configuration at the S800 Entry. . . . .	55
3.19	Determining Proper Target Location . . . . .	62
3.20	SeGA Energy Calibration Comparison . . . . .	63
3.21	Calibration Sources Energy Spectra . . . . .	64
3.22	SeGA Segment Calibrations . . . . .	65
3.23	Simulated Stationary Source Photon Events . . . . .	66
3.24	Simulated Stationary Source Photon Efficiency . . . . .	67
3.25	Total SeGA Efficiency for $^{152}\text{Eu}$ . . . . .	68
3.26	Total SeGA Efficiency for $^{152}\text{Eu}$ and $^{56}\text{Co}$ . . . . .	69
3.27	Measured to Simulated Efficiency Ratio . . . . .	70
3.28	Measured to Corrected Simulated Efficiency Ratio . . . . .	71
3.29	SeGA Timing Gates . . . . .	72
3.30	Effects of SeGA Timing Gates . . . . .	73
3.31	Data Packet Processing . . . . .	77
4.1	$^{26}\text{Si}$ Secondary Beam PID . . . . .	89
4.2	$^{25}\text{Si}$ Gated PID Spectrum . . . . .	90
4.3	$^{26}\text{Si}$ Gated XFP-OBJ TOF Spectrum . . . . .	91
4.4	$^{26}\text{Si}$ OBJ Beam Rate . . . . .	92
4.5	$^{25}\text{Si}$ Particle Detection Efficiency . . . . .	93
4.6	$^{25}\text{Si}$ Live-Time Corrections . . . . .	94
4.7	$^{25}\text{Si}$ Fragmentation Reaction Rate . . . . .	95
4.8	$^{25}\text{Si}$ $\gamma$ -ray Spectrum . . . . .	96

4.9	Simulated Photopeaks Fit to $^{25}\text{Si}$ Spectrum . . . . .	97
4.10	Alternative $\gamma$ -rays from $^{25}\text{Si}$ . . . . .	99
4.11	$^{25}\text{Si}$ Level Diagram . . . . .	100
4.12	$^{25}\text{Si}$ Momentum Distributions . . . . .	101
4.13	$^{30}\text{S}$ Secondary Beam PID . . . . .	104
4.14	$^{29}\text{S}$ Gated PID Spectrum . . . . .	109
4.15	$^{30}\text{S}$ Gated XFP-OBJ TOF Spectrum . . . . .	110
4.16	$^{30}\text{S}$ OBJ Beam Rate . . . . .	111
4.17	$^{29}\text{S}$ Particle Detection Efficiency . . . . .	112
4.18	$^{29}\text{S}$ Live-Time Corrections . . . . .	113
4.19	$^{29}\text{S}$ Fragmentation Reaction Rate . . . . .	114
4.20	$^{29}\text{S}$ $\gamma$ -ray Spectrum . . . . .	115
4.21	Simulated Photopeaks Fit to $^{29}\text{S}$ Spectrum . . . . .	116
4.22	Alternative $\gamma$ -ray from $^{29}\text{S}$ . . . . .	117
4.23	$^{29}\text{S}$ Level Diagram . . . . .	118
4.24	$^{29}\text{S}$ Momentum Distributions . . . . .	119
5.1	$R_S$ vs. $\Delta S$ . . . . .	122

# ABSTRACT

The use of single nucleon and two-like nucleon knockout reactions of medium to heavy mass exotic beams on light targets has proven an invaluable tool in exploring nuclear properties away from the valley of  $\beta$ -stability up to the proton and neutron drip-lines. The nuclear shell model has had a great amount of success in describing structural properties of nucleons populating states from the  $1s1p$ -shells up to the  $2p1f$ -shells, of particular interest is the success of the USD shell model used in the truncated  $2s1d$ -shell space. The USD Hamiltonian was updated in 2005 to include the effects of exotic nuclei. Using relativistic beam velocities greater than 30% of the speed of light allows for the direct exploration of underlying single particle valence state structure. Comparisons between current shell models and experimental results are showing discrepancies between measured and theoretical cross sections.

The focus of the present work is on the single neutron knockout reactions  ${}^9\text{Be}({}^{26}\text{Si}, {}^{25}\text{Si}+\gamma)$  and  ${}^9\text{Be}({}^{30}\text{S}, {}^{29}\text{S}+\gamma)$ . Relativistic beams containing  ${}^{26}\text{Si}$  and  ${}^{30}\text{S}$  were created at the National Superconducting Cyclotron Laboratory's Coupled-Cyclotron Facility using the A1900 fragment separator. The secondary 376 mg/cm<sup>2</sup> thick  ${}^9\text{Be}$  target was located at the pivot point of the S800, a large-acceptance, high-resolution spectrometer with a specialized detector system that allowed for accurate event-by-event particle identification of the incident and residual particles based on their mass and charge, as well as providing accurate longitudinal momentum distribution measurements of the post-target beam. The secondary target was also surrounded by SeGA, a  $\gamma$ -ray detector array specifically designed for accurate Doppler reconstruction of observable  $\gamma$ -rays into the emitting particles rest frame. Measurements were made of the direct inclusive and individual state population cross sections in the residual states, as well as the first measurements of electromagnetic transitions between energy levels in both  ${}^{25}\text{Si}$  and  ${}^{29}\text{S}$ .

Two new  $\gamma$ -rays were observed for  ${}^{25}\text{Si}$  at 821(15) keV and 1088(22) keV. The 821(15)

keV  $\gamma$ -ray is a direct decay from the first  $1/2^+$  state to the  $5/2^+$  ground state, while the 1088(22) keV  $\gamma$ -ray is actually a result of a  $3/2^+$  state at 1909(27) keV feeding into the  $1/2^+$  state at 821(15) keV. The measured cross sections for the  $^{26}\text{Si}\rightarrow^{25}\text{Si}$  reaction were  $\sigma(\textit{inclusive}) = 26.1(35)$  mb,  $\sigma(1909\textit{keV}) = 1.06(21)$  mb, and  $\sigma(821\textit{keV}) = 4.06(61)$  mb.

There were three new  $\gamma$ -ray transitions seen for  $^{29}\text{S}$  with energies of 1160(16) keV, 1222(20) keV, and 1727(37) keV, which correspond to the first experimental observation of excited states in  $^{29}\text{S}$ . The 1222(20) keV decay is the direct decay from the  $1/2^+$  first excited state to the  $5/2^+$  ground state, while the 1727(37) keV  $\gamma$ -ray is the decay of the  $7/2^+$  state to the ground state, however the 1727(37) keV state is only populated by direct feeding from the  $5/2^+$  state at 2887(40) keV by the observed 1160(16) keV  $\gamma$ -ray. The measured cross sections for the  $^{30}\text{S}\rightarrow^{29}\text{S}$  reaction were  $\sigma(\textit{inclusive}) = 27.5(26)$  mb,  $\sigma(1222\textit{keV}) = 3.09(33)$  mb, and  $\sigma(2887\textit{keV}) = 1.86(15)$  mb.

The reduction factor to the shell model spectroscopic strength for the inclusive cross section for the  $^{26}\text{Si}\rightarrow^{25}\text{Si}$  reaction is 0.55(7) and the reduction factor for the inclusive cross section for the  $^{30}\text{S}\rightarrow^{29}\text{S}$  reaction is 0.46(4). With valence binding separation energy differences of  $\Delta S = 13.5$  MeV for  $^{26}\text{Si}$  and  $\Delta S = 14.6$  MeV for  $^{30}\text{S}$ , these reduction factors are in good agreement with the systematic behavior of reduction factors from other single nucleon knockout reaction studies. The calculated electromagnetic multipole transition strengths in both  $^{25}\text{Si}$  and  $^{29}\text{S}$ , when taken into consideration with the observed decay branching ratios, allows some speculation that these nuclei are well-deformed and that the known region of deformation in the  $sd$ -shell extends out to both. Based on the evidence in the current work, intermediate-energy Coulomb excitation studies would help in completing the level schemes and also verify the branching strength of the  $E2$  transitions characteristic of deformed nuclei.

# CHAPTER 1

## INTRODUCTION

Nuclear structure physics has been evolving to adapt to the growing knowledge of the nuclear landscape since the conception of an atomic nuclear core by Rutherford's early 1900s scattering experiments (Ref. [1]). Even before these experiments, there was some concept of a substance that contained all the atom's positive charge and the large majority of the atomic mass. The discovery of the proton as a fundamental particle was attributed to Rutherford in 1919 in Ref. [2]. However, it was not until the work of Chadwick in 1932's Ref. [3], that the existence of the neutron as a fundamental particle was also discovered. Around the same time as these two essential discoveries, the pivotal field of quantum mechanics was also emerging to prominence. Viewing the atomic nucleus as a composite system of positively charged protons and neutrally charged neutrons, each with relatively equivalent masses and behaving under quantum mechanical rules, explained the observable masses and charges of the atomic nuclei. Because of their similarities, a proton or a neutron can also be referred to generically as a nucleon. With the introduction of quantum mechanics, the problems of nuclear structural physics became a clearly complicated quantum many-body problem with no simple or analytic answer. There are three fundamental force interactions that dominate the structure of the nucleus: the first is the strong nuclear interaction force that binds nuclei together; the second is the weak interaction that allows for a proton to change to a neutron and vice-versa by  $\beta$ -decay; the third is the electromagnetic force that is responsible for a repulsive force between electrically charged protons, and is the mechanism for photon emission in nuclear  $\gamma$ -ray decay. The collective goal of nuclear physics is to determine a set of rules that govern all interactions between nuclei. Experimental work is performed with a goal of creating a complete set of observable phenomena in which evolving nuclear structure theories and interaction mechanisms can be tested.

The current standard particle model shows that the protons and neutrons are actually composites of particles called quarks. However for the purposes of this study, it is safe to assume that the quark interactions between separate nucleons can be described as a net force that binds nucleons on a whole to one another and each nucleon can be considered an individual fermionic particle. The nuclear force appears to be equivalent for proton-proton, neutron-neutron, and proton-neutron interactions, where the only differences arise from the Pauli exclusion force and Coulomb repulsion. As a result of this, a nucleon's label as a proton or neutron can be considered as just another quantum label on the nucleon that is called isospin. The molecular and chemical properties of a particular nucleus are almost completely dependent on the number of protons in its core which bind the orbiting electrons to the atom, so chemically there is little difference between groups of nuclei with the same number of protons and a differing number of neutrons. A group of atoms with the same number of protons are called isotopes. Each isotope group is denoted either by the number of protons  $Z$ , or its equivalent element on the Periodic Table, for which there is one element for every known isotope group. Similarly, nuclei with the same number of neutrons and differing number of protons are called isotones, and nuclei with the same number of total nucleons can be referred to as isobars. The convention for labeling a nucleus is by its total number of nucleons  $A$  and its isotope group's chemical symbol.

There are a number of nuclear structure models in circulation, and as previously stated, the main problem is that of a quantum many-body system of interacting particles. One view that has a proven applicability is that of the shell model which pictures nuclear structure as a summed effect of each individual nucleon in a mean potential field with effective residual interactions among the nucleons. The shell models have worked well in describing low energy structural configurations of light to medium mass nuclei where the nucleon interactions are manageable and collective effects are less dominant. This is especially true in the  $sd$ -shells, in which nuclear phenomena can be contributed to the shifting of a minimum number of nuclei out of their ground state configurations. The first part of Chapter 2 will give an overview of the nuclear shell models and in particular the  $sd$ -shell  $USD$  Hamiltonian models.

A strong test of single particle structure is the determination of nucleon occupational probabilities in the valence shells of light to medium nuclei. The extraction of occupation probabilities from measured cross sections is heavily reliant on an accurate reaction model. For several decades, probes of this type were mostly restricted to single nucleon transfer

reactions at low energies. Reactions of this type are very dependent on well defined potentials and parameters that are at present poorly defined for nuclei further from the valley of  $\beta$ -stability. Because of this, the use of single nucleon transfer reactions has been restricted mainly to light beams on stable targets, and even then their ability to acquire absolute as opposed to relative spectroscopic information has been brought into question (see Ref. [4], and references therein). Since the 1980s, the use of electrons for  $(e, e'p)$  reactions have been providing valuable insight into absolute spectroscopic information (see Ref. [5]), however these experiments are still restricted to experiments on stable nuclei. With the advent of high-energy exotic beam facilities such as the National Superconducting Cyclotron Laboratory (NSCL), direct single nucleon knockout reactions have become a powerful tool for measuring single particle spectroscopic information (see Refs. [4, 6]). The use of knockout reactions has been successfully implemented for a number of nuclear structure experiments in the  $A < 50$  mass range. Because of the nature of the knockout reaction, it is a very good probe of low energy single particle structure phenomena. Another benefit of the single nucleon knockout reaction is that it can be performed on nuclei far from the limitations of  $\beta$ -stability, in the region of very short lived exotic nuclei both on the proton rich and neutron rich side of the valley of stable nuclei. Chapter 2 will also tie in the relationship between experimental observables and their comparable predictions.

The NSCL provides facilities for the creation and monitoring of radioactive particle beams, and also a special set of detection equipment designed for the specific purpose of measuring radiation emission and reaction products from nuclear collisions of heavier mass relativistic projectiles on lighter mass target particles. Chapter 3 will present a discussion of the experimental techniques and devices used in the current work.

Chapter 4 presents the analysis and results of the single neutron knockout reactions  ${}^9\text{Be}({}^{26}\text{Si}, {}^{25}\text{Si} + \gamma)$  and  ${}^9\text{Be}({}^{30}\text{S}, {}^{29}\text{S} + \gamma)$ . This work marks the first  $\gamma$ -ray spectroscopy of both  ${}^{25}\text{Si}$  and  ${}^{29}\text{S}$  as well as the first exploration of the excited state level structure of  ${}^{29}\text{S}$ . The spectroscopic strengths of valence neutron shell states in  ${}^{26}\text{Si}$  and  ${}^{30}\text{S}$  are evaluated and compared to the updated *USD* shell model theoretical calculations. These results are in good agreement with the results obtained from other single nucleon knockout reactions, in which a noticeable reduction of the single particle model occupation strength appears to be related to the proton-neutron separation energy differences.

Chapter 5 will provide a summary review of the significant experimental results and

their implications on current nuclear structure and reaction theories. This chapter will also present current and relevant open topics for future experimental and theoretical studies.

# CHAPTER 2

## THEORETICAL TREATMENT

This chapter will cover the various theoretical tools used for the work at hand. The theoretical descriptions of the nuclear structure, decay, and reactions will be described in this chapter. The theory can be divided into two main categories, the nuclear structure theory and the reaction model theory. The first is discussed in Sec. 2.1 and the latter in Sec. 2.2.

### 2.1 The Shell Model

The first nuclear shell model was built upon the success of the original atomic electron shell model and the collected observations made by Maria Goeppert-Mayer in Ref. [7]. The first nuclear shell model was introduced in 1949 by Goeppert-Mayer in Ref. [8], and Haxel, Jensen, and Suess in Ref. [9]. This first model is often referred to as the *naive shell model* or the *independent particle shell model*. The naive shell model was based on the observations of particularly stable configurations of nuclei with neutron or proton numbers of  $N, Z=8, 20, 28, 50, 82,$  and  $126$ , which are commonly referred to as *magic numbers*. The naive shell model assumes that the nucleus is a collection of independent nucleons, each of which moves in a potential that includes an orbital angular momentum term and a strong spin-orbit coupling term. The naive shell model uses harmonic oscillator basis states with orbital angular momentum ( $\ell$ ) and spin ( $s$ ) quantum numbers. The main oscillator level numbers  $N$  typically associated with the harmonic oscillator Hamiltonian are now given by  $N = 2(n - 1) + \ell$ , where  $n$  is referred to as the nucleon's primary or radial quantum number. The nucleons fill the lowest energy levels first and must obey Fermi-Dirac statistics. The relative energy levels of the naive shell model are shown in Fig. 2.1, in which each shell is distinguished by its orbital angular momentum  $\ell$ , radial quantum number  $n$ , and total angular momentum  $j$  which is the coupling of the orbital and spin angular momenta. The

naive shell model does explain the appearance of magic numbers as shell closures, however it never proved to be a robust method for predicting other structural properties of nuclei, and as described in Ref. [10] and the references there in, the traditional magic numbers of stable nuclei resulting from shell closures are not quite as magic for exotic nuclei. Regardless, the naive shell model is still a good starting point for a first guess approach at the structure of nuclei. The filled neutron and proton shells of  $^{26}\text{Si}$  in the naive shell model are shown in Fig. 2.2, and likewise for  $^{30}\text{S}$  in Fig. 2.3.

### 2.1.1 Modern Shell Models

There are volumes of written material describing the shell model approach to nuclear structure, e.g., Refs. [11, 12, 13]. The shell model approach pivots on a fundamental assumption that the nucleus can be described by a mean field potential and residual nucleon interactions. Shell models use linear combinations of the independent particle model states to describe the observable nucleus. The complete shell model Hamiltonian can then be written as

$$\mathcal{H} = \sum_{i=1}^A h_i + \mathcal{R}, \quad (2.1)$$

where  $h_i$  is a sum over single particle Hamiltonians (often referred to as the *Single Particle Energy* or *SPE*) and  $\mathcal{R}$  is the residual interactions between the nucleons. The residual interaction term can then be reduced to only account for two-body interactions so that

$$\mathcal{R} = \sum_{i<j=1}^A V_{ij} - \sum_{i=1}^A v_i, \quad (2.2)$$

where  $V_{ij}$  is the two-body interaction between nucleon  $i$  and nucleon  $j$ , and  $v_i$  is the single particle potential energy that is already accounted for in  $h_i$ .

There are several nuclear structure models in current circulation (see Refs. [14, 10, 6]), however the large number of free parameters in most of the models built from realistic nucleon-nucleon interactions is often prohibitive and unwieldy for predictive use in experiments. As the number of nucleons increases, so too does the number and complexity of the residual nucleon interactions. The nuclear region of protons and neutrons in what is referred to as the *sd*-shell ( $8 \leq (N, Z) < 20$ ) which consist of the  $2s_{1/2}$ ,  $1d_{3/2}$ , and  $1d_{5/2}$  shells, is a particularly well suited region for shell model studies, in that the number

of nucleons is enough to allow for an appreciable, yet manageable, number of residual interactions. Hopefully, as more and better experimental data becomes available an accurate parameterization of more complex nuclear shell models will become possible.

### 2.1.1.1 The USD Shell Models

The *Universal sd*-shell model (*USD*), as described in Refs. [15, 16, 17] has shown a tremendous amount of predictive reliability in its applicable nuclear region for over two decades. The USD shell model is a phenomenological model of the truncated *sd*-shell, meaning that it assumes an inert core of  $^{16}\text{O}$  and does not directly account for any nucleon wave-functions from outside of the *sd*-shell. The USD Hamiltonian is defined as

$$\mathcal{H} = \sum_a \epsilon_a \hat{n}_a + \sum_{a \leq b, c \leq d} \sum_{JT} V_{JT}(ab; cd) \hat{T}_{JT}(ab; cd), \quad (2.3)$$

where  $a$  represents a nucleon in an orbit with quantum numbers  $(n_a, \ell_a, j_a)$ , and similarly for  $b, c$ , and  $d$ , which are summed over all nucleons. The second term is summed over all possible angular momentum ( $J$ ) and isospin values ( $T$ ) possible from coupling the nucleons  $a, b$  and  $c, d$ .  $\hat{n}_a$  is the number operator for the nucleon orbit denoted by  $a$ , and likewise,  $\hat{T}_{JT}$  is the scalar two-body density operator for the nucleon pairs  $a, b$  and  $c, d$ . The values of  $\epsilon_a$  in the first term are the single particle energies (SPEs) mentioned previously and  $V_{JT}(ab; cd)$  contain the residual interaction potentials, also referred to as a *two-body matrix element* or *TBME*. Using Eq. 2.3, the USD shell model is defined by three SPEs and 63 TBMEs, for a total of 66 parameters. The original USD model was parameterized from a least squares fit of 380 well determined experimental energy data from 66 nuclei. In 2006, Ref. [18] recalculated the parameters of the original USD using improved computational power and a larger available data set of 608 well determined experimental states in 77 nuclei. The results of Ref. [18] were classified into two separate Hamiltonian parameter sets known as the *USDA* and the *USDB*. A comparison of the number of states included in the original USD interaction and the revamped *USDA* and *USDB* interactions are shown in Fig. 2.4. The distinction between the *USDA* and *USDB* parameter sets was the number of linear combinations of TBMEs and SPEs used in the fitting routine as described in Ref. [18]. The *USDA* parameter set was determined from a fit of 30 of the most well defined linear combinations, while the *USDB* parameters were determined from a fit of 56 linear combinations. In both cases the remaining poorly defined parameters are assigned values from an effective nucleon-nucleon

interaction as described in Ref. [18]. Upon conception, the USDB model fit more closely to the experimental data, so it is typically used for direct experimental comparisons and the USDA is reserved for a measure of theoretical uncertainty, which is the justification laid out for creating two Hamiltonians in Ref. [18].

### 2.1.2 Spectroscopic Information

A keystone for testing any nuclear structure theory is the ability to accurately predict energy levels of bound states, and in the case of the shell model approach, the ability to calculate individual nucleon wave-function contributions to the total nuclear wave-function. Shell models, by nature, allow for calculations of single nucleon occupation probabilities in each shell. Single nucleon removal reactions serve as an excellent probe of the single nucleon wave-function contributions to the valence nucleon shell structure. The single nucleon occupational probability determined from a single nucleon removal reaction is typically referred to as a *spectroscopic factor* or commonly written as  $C^2S$ . A spectroscopic factor is the measurement of a single particle orbital occupational strength in a nucleus of  $A$  nucleons. This is done by coupling a single nucleon to a specific state of the  $(A - 1)$  nucleon system, and taking the overlap of this coupled system to a specific state (the ground state for this work) in the  $A$  nucleon system as shown by

$$C^2S(\mu, \lambda) = | \langle \Phi_{(A-1)}^\mu | a(\lambda) | \Phi_A^0 \rangle |^2 . \quad (2.4)$$

$\Phi_A^0$  represents the ground state wave-function of the  $A$  nucleon system and  $\Phi_{(A-1)}^\mu$  is the specific state denoted by  $\mu$  of the  $(A - 1)$  nucleon system.  $a(\lambda)$  is the annihilation operator of a single nucleon with single particle basis state quantum numbers denoted by  $\lambda$ . The  $C^2$  term on the left-hand side of Eq. 2.4 is the explicit isospin  $(T, T_z)$  coupling Clebsch-Gordon factor that is usually separable from the rest of the single particle overlap. A figurative diagram of a spectroscopic factor is shown in Fig. 2.5. The energy levels and respective single neutron removal spectroscopic factors calculated with the USD, USDA, and USDB Hamiltonians for  $^{26}\text{Si} \rightarrow ^{25}\text{Si}$  reaction is shown in Table 2.1 and Fig. 2.6. The same calculations for  $^{30}\text{S} \rightarrow ^{29}\text{S}$  are shown in Table 2.2 and Fig. 2.7.

Table 2.1: The excited state energy levels of  $^{25}\text{Si}$  and single neutron knockout  $C^2S$  from  $^{26}\text{Si}$  calculated with the *USD*, *USDA*, and *USDB* shell model Hamiltonians. The far left column is the total angular momentum and parity  $J^\pi$  of each state.

$^{25}\text{Si}$ $J^\pi$	<i>USD</i>		<i>USDA</i>		<i>USDB</i>	
	$E(\text{keV})$	$C^2S$	$E(\text{keV})$	$C^2S$	$E(\text{keV})$	$C^2S$
$5/2^+$	0	2.80	0	2.65	0	2.73
$3/2^+$	132	0.12	181	0.13	114	0.12
$1/2^+$	1159	0.27	1028	0.25	966	0.25
$3/2^+$	2130	0.21	2015	0.21	1981	0.18

Table 2.2: The excited state energy levels of  $^{29}\text{S}$  and single neutron knockout  $C^2S$  from  $^{30}\text{S}$  calculated with the *USD*, *USDA*, and *USDB* shell model Hamiltonians. The far left column is the total angular momentum and parity  $J^\pi$  of each state.

$^{29}\text{S}$ $J^\pi$	<i>USD</i>		<i>USDA</i>		<i>USDB</i>	
	$E(\text{keV})$	$C^2S$	$E(\text{keV})$	$C^2S$	$E(\text{keV})$	$C^2S$
$5/2^+$	0	3.80	0	3.55	0	3.63
$1/2^+$	1214	0.35	1301	0.34	1214	0.36
$7/2^+$	1799	-	1854	-	1858	-
$3/2^+$	1959	0.02	2193	0.002	2076	0.02
$3/2^+$	2735	0.22	2617	0.28	2704	0.22
$5/2^+$	2801	0.71	3091	0.39	2993	0.80
$5/2^+$	3017	0.04	3116	0.49	3095	0.06

### 2.1.2.1 The Sum Rule and Quenching Reduction Factors

As shown in Refs. [11, 19], the independent particle model yields a novel solution for the upper limit of the summed spectroscopic factors for a single nucleon removal reaction. Assuming a nucleon must be removed from the valence shells before any nucleons from lower levels may be removed, the maximum number of nucleons that can participate in a single nucleon removal reaction is simply the number of nucleons of appropriate isospin in that valence shell. This is typically referred to as the *spectroscopic sum rule*, and for the case of  $^{26}\text{Si} \rightarrow ^{25}\text{Si}$  the summed  $C^2S$  is four while for the  $^{30}\text{S} \rightarrow ^{29}\text{S}$  reaction it is six. In the modern shell models such as the USD, the basis states are created as linear combinations of the independent particle model states, this causes a sort of smearing of the spectroscopic strengths across several different independent particle states. Every isotope has a nucleon separation energy that

serves as a rough cut-off for bound excited states. A portion of the spectroscopic strength can be even be pushed to energy levels above this separation energy. This effect is more noticeable in exotic nuclei as the nucleon separation energy becomes smaller.

There has been a pronounced systematic reduction of the spectroscopic strength from the shell model predictions in nucleon knockout and  $(e, e'p)$  reactions (see Refs. [4, 5, 20, 6]). This effect of losing spectroscopic strength in experimental measurements is known as *quenching*, which was quantified in Ref. [21] by the quenching *reduction factor*  $R_S$ . The reduction factor is the ratio of the experimentally determined spectroscopic factors to the spectroscopic factors from a shell model calculation. The present work utilizes the USDB Hamiltonian, but the reduction factor is dependent on the choice of shell model. Because the measurement of the occupational probabilities is highly dependent on the reaction, it is typically more convenient to determine the reduction factor from the ratio of the measured cross section ( $\sigma_{\text{exp}}$ ) to the theoretical cross section ( $\sigma_{\text{th}}$ , to be discussed in Sec. 2.2), which takes into account both the shell model nuclear structure contributions and the reaction components so that

$$R_S = \frac{\sigma_{\text{exp}}}{\sigma_{\text{th}}}. \quad (2.5)$$

It should be noted that this equality is only as accurate as the theoretical reaction model's accuracy. As reported in Refs. [20, 6, 4], the reduction factor is believed to be from correlation effects related to short-range and tensor nucleon-nucleon interactions, soft-core effects, and even collective excitation effects. As shown in Ref. [20], the reduction factors appear to be dependent on the asymmetry of the proton and neutron Fermi surface. This difference is quantified by the separation energy difference  $\Delta S$  between the proton separation energy  $S_p$  and the neutron separation energy  $S_n$  such that

$$\Delta S = \begin{cases} S_n - S_p & \text{for neutron removal,} \\ S_p - S_n & \text{for proton removal.} \end{cases} \quad (2.6)$$

For large negative values of  $\Delta S$ ,  $R_S$  approaches unity, implying that removal of a weakly bound nucleon more closely resembles the shell model interaction. As the energy of  $\Delta S$  increases, the spectroscopic strengths decrease in what appears to be a nearly linear manner to values as low as 20% of the predicted shell model values.

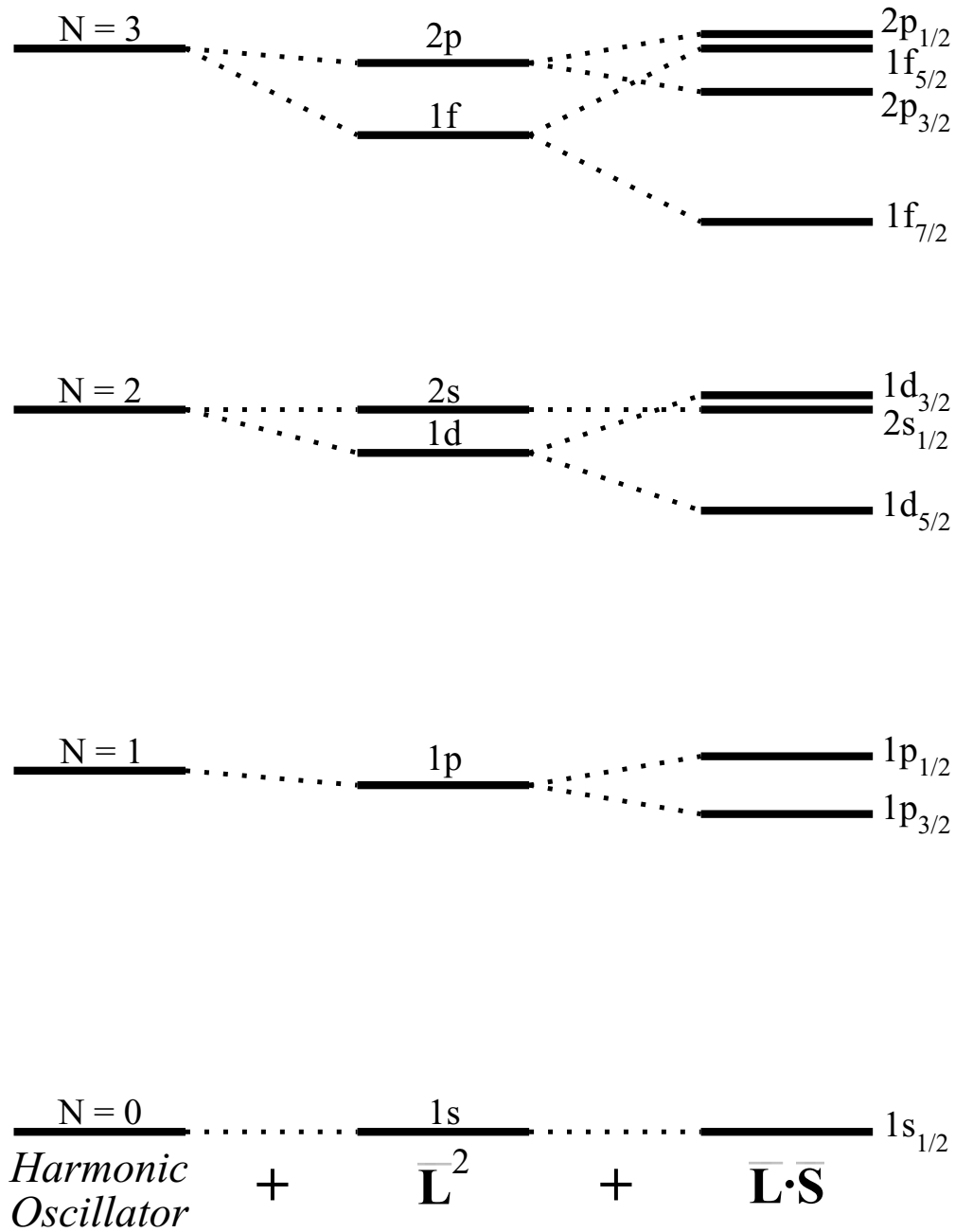


Figure 2.1: Energy levels of the naive nuclear shell model. The bottom of the plot represents the lowest energy level with excitation energy increasing upward. The left side represents the energy levels for a simple harmonic oscillator (*SHO*) potential. The middle depicts the energy level splitting as an orbital angular momentum term is added to the *SHO* potential. The right side shows the further splitting that occurs after adding an additional spin-orbit splitting terms to the Hamiltonian.

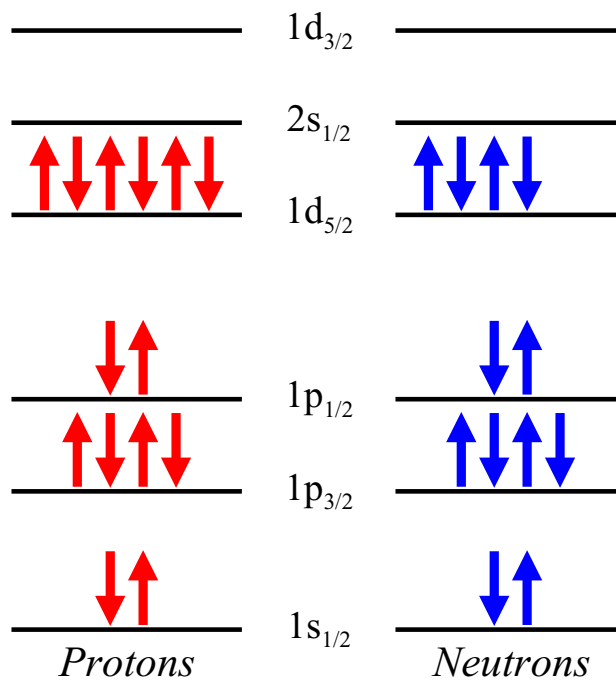


Figure 2.2: The filled proton and neutron shells of  $^{26}\text{Si}$  in the naive shell model. Protons fill their  $1d_{5/2}$  valence shell and there are two vacancies in the partially filled  $1d_{5/2}$  neutron valence shell.

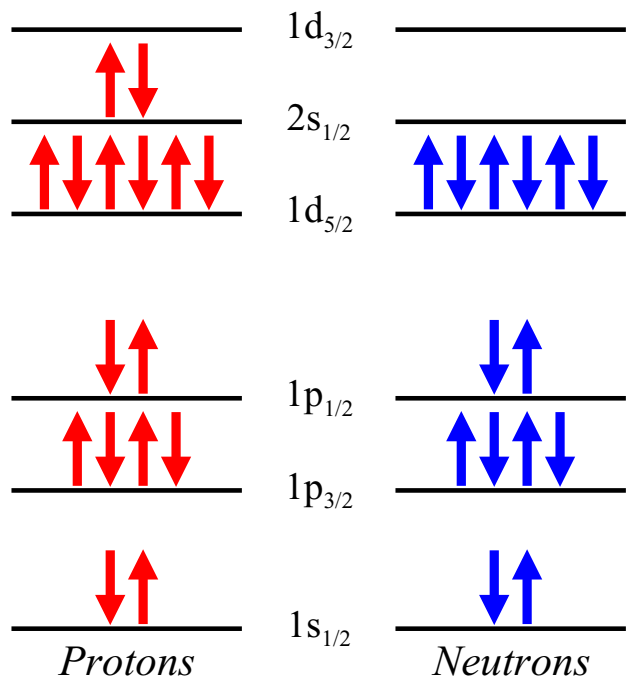


Figure 2.3: The filled proton and neutron shells of  $^{30}\text{S}$  in the naive shell model. Protons fill their  $2s_{1/2}$  valence shell and neutrons fill their  $1d_{5/2}$  valence shell.

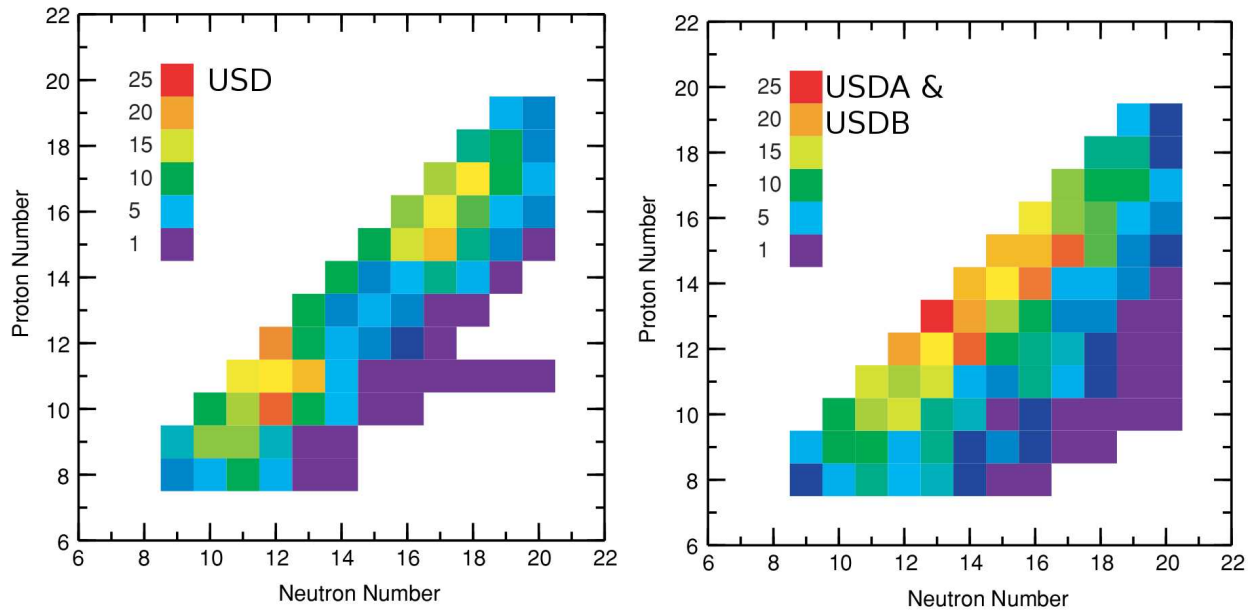


Figure 2.4: The figure on the left shows the number of states used for each nucleus to determine the USD Hamiltonian. Likewise, the figure on the right is the number of states used for each nucleus to determine the USDA and USDB Hamiltonians. Both figures were taken directly from Ref. [18].

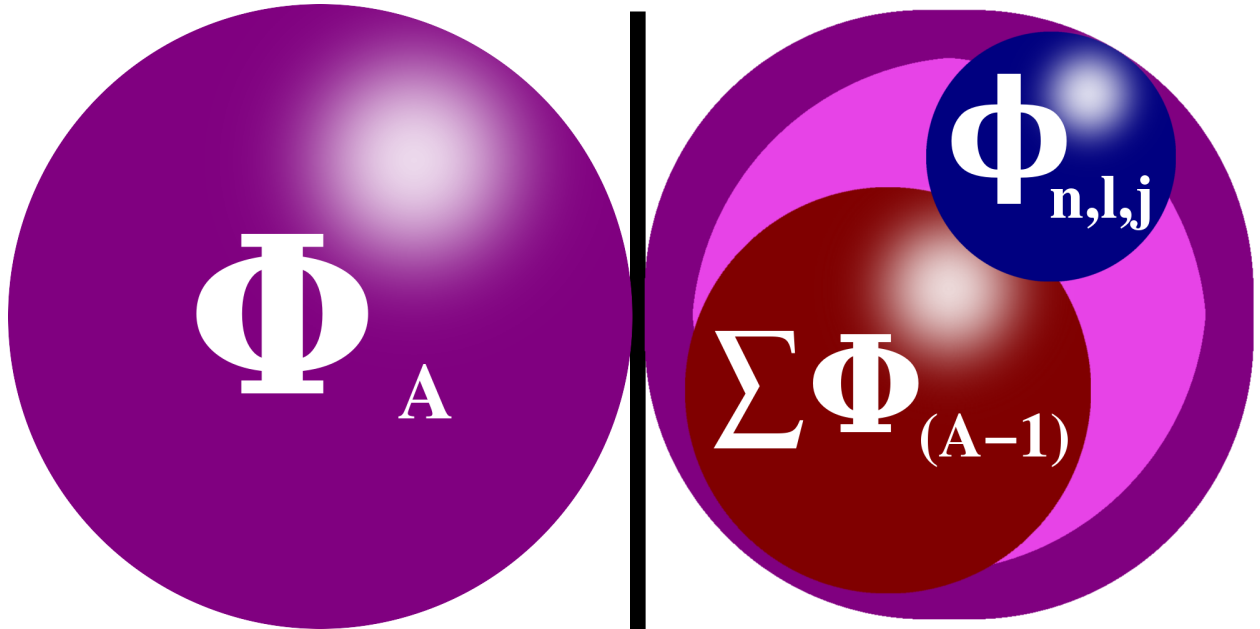


Figure 2.5: A depiction of the nuclear states measured by shell model spectroscopy given by Eq. 2.4. The left hand side represents a single state of the complete  $A$  nucleon system  $\Phi_A$ , while the right hand side represents the possible internal configurations of all the possible  $(A - 1)$  nucleon systems  $\Phi_{(A-1)}$  (hence the summation), coupled to a single nucleon in the  $(n, l, j)$  orbital.

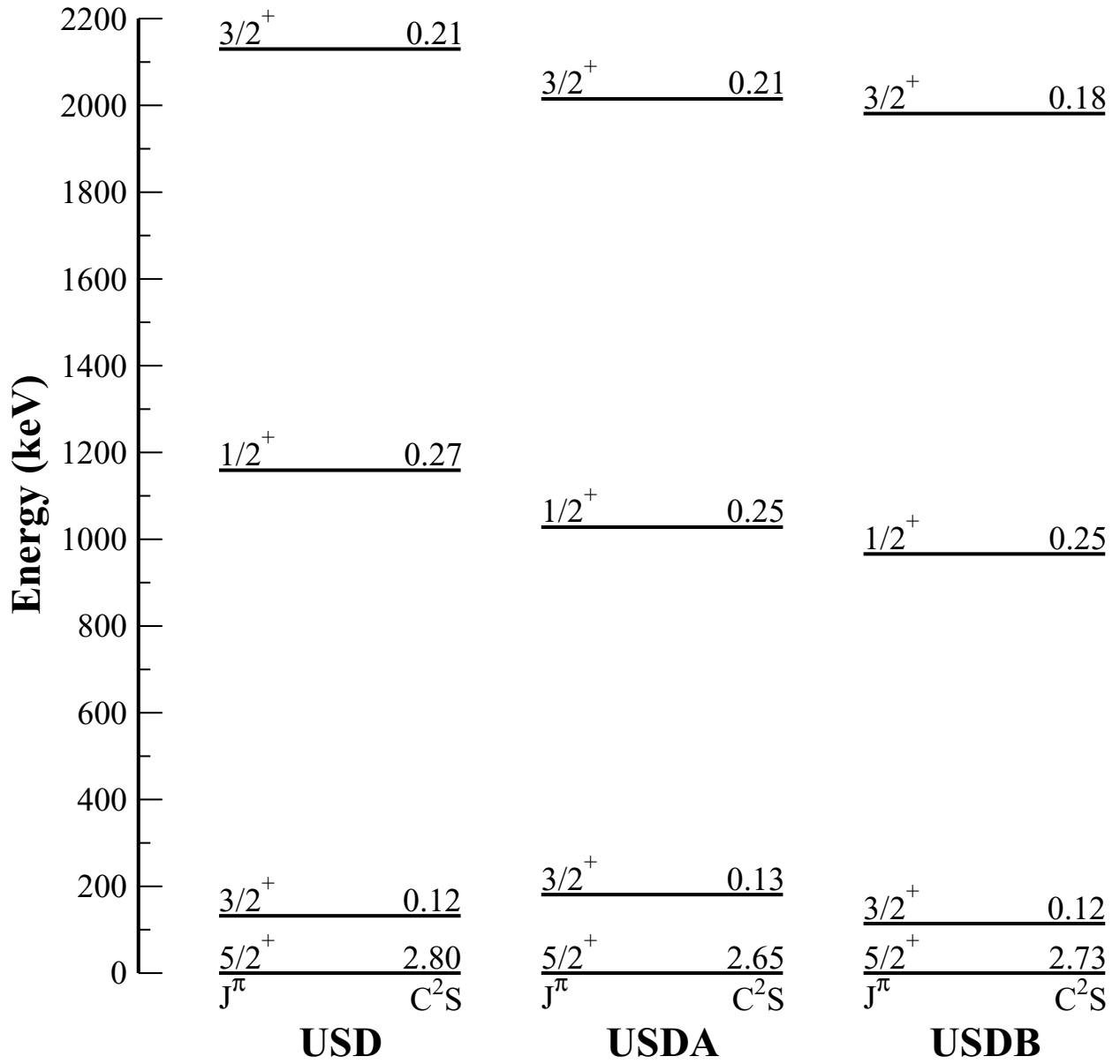


Figure 2.6: An energy level diagram of the *USD*, *USDA*, and *USDB* shell model calculations for  $^{25}\text{Si}$ . Each state is labeled by its total angular momentum and parity  $J^\pi$ , and its spectroscopic strength in  $^{26}\text{Si}$ .

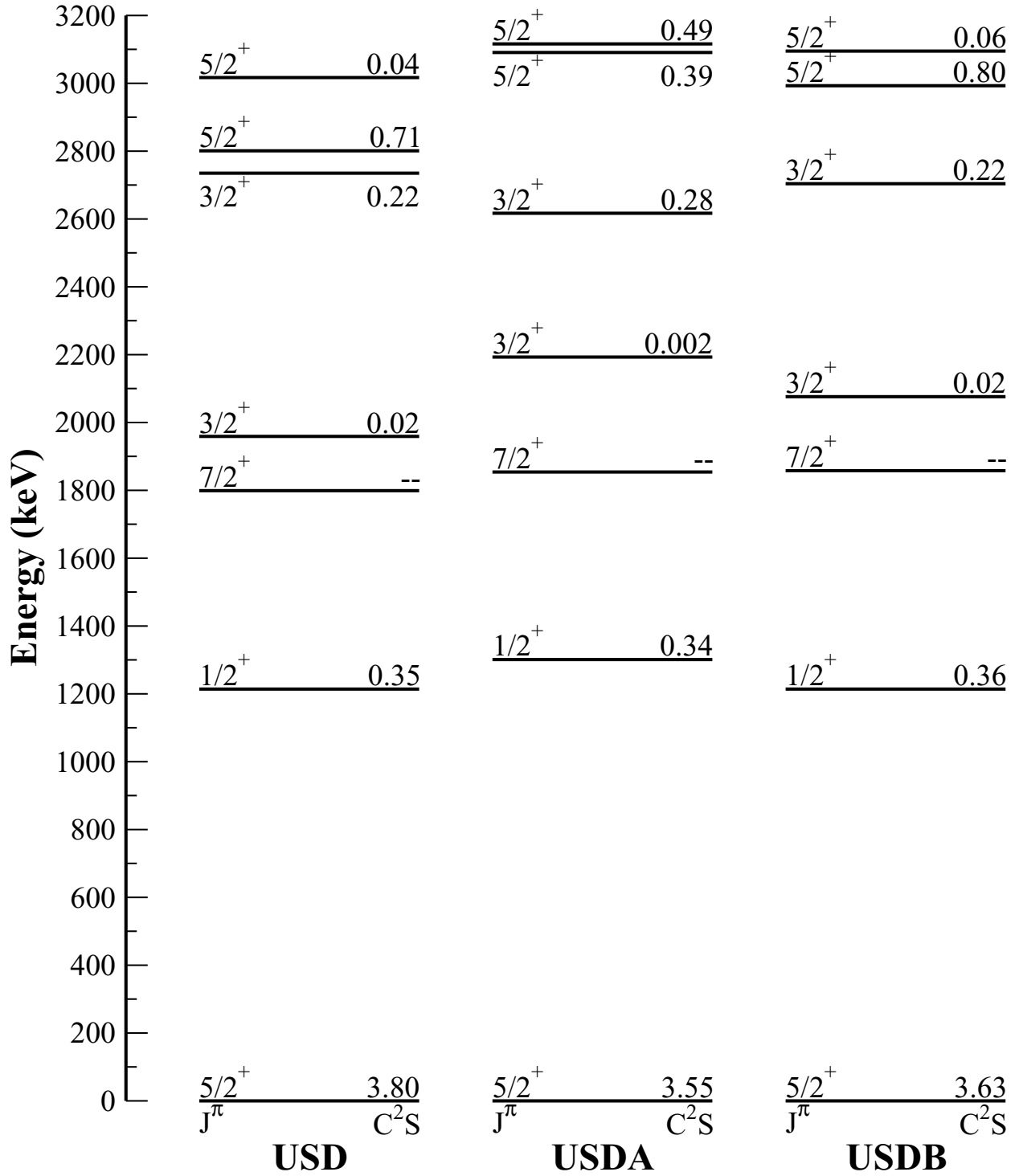


Figure 2.7: An energy level diagram of the *USD*, *USDA*, and *USDB* shell model calculations for  $^{29}\text{S}$ . Each state is labeled by its total angular momentum and parity  $J^\pi$ , and its spectroscopic strength in  $^{30}\text{S}$ .

### 2.1.3 Electromagnetic Transitions

The electromagnetic transitions between bound nuclear states have provided invaluable insight into the structure of the atomic nucleus. The definitive tome of the nuclear electromagnetic interaction is collected in Ref. [22], but it is hard for any volume on nuclear physics to not contain some discourse on the topic. Electromagnetic transitions result in the emission of a photon from the nucleus, this photon is most commonly referred to as a  $\gamma$ -ray or  $\gamma$ -radiation. The interaction preserves the isospin projection ( $T_z$ ) and nucleon number of the nucleus, but allows for transitions between states of the nucleus through electromagnetic multipole radiation that allows for both energy and angular momentum conservation. The electromagnetic transitions can be separated into two types, either electric or magnetic, however that is not to say that a single transition cannot contain components of each, but it does allow for certain limitations and rules to be established. The transition rate propagated by a  $2^\lambda$ -pole radiation with angular momentum  $\lambda$  between an initial state of angular momentum  $j_i$  and energy  $\epsilon_i$ , and a final state of  $j_f$  and  $\epsilon_f$  is given by

$$T(j_i \rightarrow j_f) = \sum_{\lambda, \pi} \frac{8\pi(\lambda + 1)}{[(2\lambda + 1)!!]^2 \lambda \hbar} \left( \frac{\epsilon_i - \epsilon_f}{\hbar c} \right)^{2\lambda+1} B(\pi\lambda, j_i \rightarrow j_f), \quad (2.7)$$

where  $\pi$  is either  $E$  or  $M$  for electric or magnetic type radiations and  $B(\pi\lambda)$  is the *reduced transition probability* which is dependent on a  $2^\lambda$ -multipole operator that is unique for both  $\pi$  values. Through the  $B(\pi\lambda)$  term, the electromagnetic decay obeys the standard rules as described in Refs. [23, 22, 12, 13] for coupling the three angular momentum states of  $j_f$ ,  $j_i$ , and  $\lambda$ .

The parity of a nuclear state is dependent on its orbital angular momentum value, where even  $\ell$  values ( $s, d, g, \dots$ , orbitals) have even parity and odd  $\ell$  values ( $p, f, \dots$ , orbitals) have odd parity. Electromagnetic transitions can affect the parity of the final state, dependent on the  $(\pi, \lambda)$  values in Eq. 2.7. Parity is conserved between the initial and final states if  $(\pi = E, \lambda = \text{even})$  or  $(\pi = M, \lambda = \text{odd})$ , and parity is changed between the initial and final states if  $(\pi = E, \lambda = \text{odd})$  or  $(\pi = M, \lambda = \text{even})$ .

In the shell model approach, the photon emissions are considered to be the result of a single nucleon's motion. For the few lowest excited states, this is typically an accurate assumption. Also, all of the  $sd$ -shell orbitals have even parity, which means that all transitions between the states in the  $sd$ -shell space must maintain this even parity, which

limits the possible electromagnetic decays to either  $E2$  or  $M1$  type transitions. The  $M1$  and  $E2$  transition rates for  $^{25}\text{Si}$  and  $^{29}\text{S}$  are shown in Table 2.3 for the USDA Hamiltonian and Table 2.4 for the USDB Hamiltonian. In the ideal independent particle motion picture, a proton will have both electric and magnetic transition components and a neutron will only have allowable magnetic transitions, however in reality there are collective nucleon effects which cause all nucleons to have allowable electric and magnetic transition components. A characteristic of a strong neutron transition is a dominant magnetic component in the decay, while proton transitions typically have a strong electric transition along with a sometimes appreciable magnetic component.

Table 2.3: *USDA* electromagnetic transition rates. The values were calculated with the proton effective charge of  $1.5e$  and the neutron effective charge of  $0.5e$ . These effective charges are necessary to account for collective nucleon effects.

$^{25}\text{Si}$				
$J^\pi$	Init. State Energy (keV)	Fin. State Energy (keV)	$M1$ -Transition Rate (Hz)	$E2$ -Transition Rate (Hz)
$5/2^+$	0	-	-	-
$3/2^+$	181	0	$3.05 \times 10^9$	$2.48 \times 10^7$
$1/2^+$	1028	181	$7.38 \times 10^9$	$1.34 \times 10^{10}$
		0	-	$9.36 \times 10^{10}$
$3/2^+$	2015	1028	$2.93 \times 10^{12}$	$4.80 \times 10^{10}$
		181	$5.74 \times 10^{12}$	$1.35 \times 10^{12}$
		0	$2.51 \times 10^{13}$	$3.58 \times 10^{11}$

$^{29}\text{S}$				
$J^\pi$	Init. State Energy (keV)	Fin. State Energy (keV)	$M1$ -Transition Rate (Hz)	$E2$ -Transition Rate (Hz)
$5/2^+$	0	-	-	-
$1/2^+$	1301	0	-	$1.55 \times 10^{11}$
$7/2^+$	1854	1301	-	-
		0	$2.48 \times 10^{13}$	$2.36 \times 10^{12}$
$3/2^+$	2193	1854	-	$5.61 \times 10^7$
		1301	$9.02 \times 10^9$	$3.30 \times 10^{10}$
		0	$1.01 \times 10^{13}$	$1.03 \times 10^{12}$
$3/2^+$	2617	2193	$2.90 \times 10^{10}$	$4.29 \times 10^3$
		1854	-	$2.31 \times 10^9$
		1301	$9.60 \times 10^{11}$	$6.40 \times 10^9$
		0	$5.36 \times 10^{12}$	$2.79 \times 10^{12}$
$5/2^+$	3091	2617	$6.38 \times 10^9$	$8.66 \times 10^7$
		2193	$2.36 \times 10^{11}$	$5.62 \times 10^7$
		1854	$8.30 \times 10^{12}$	$6.91 \times 10^{10}$
		1301	-	$2.15 \times 10^{11}$
		0	$5.76 \times 10^{12}$	$3.44 \times 10^{12}$
$5/2^+$	3116	3091	$8.65 \times 10^6$	$1.78 \times 10^2$
		2617	$7.47 \times 10^{11}$	$9.05 \times 10^7$
		2193	$2.70 \times 10^{12}$	$1.29 \times 10^{10}$
		1854	$3.00 \times 10^{12}$	$1.73 \times 10^{10}$
		1301	-	$1.01 \times 10^{12}$
		0	$1.55 \times 10^{12}$	$3.94 \times 10^{12}$

Table 2.4: *USDB* electromagnetic transition rates. The values were calculated with a proton effective charge of  $1.5e$  and a neutron effective charge of  $0.5e$ . These effective charges are necessary to account for collective nucleon effects.

$^{25}\text{Si}$				
$J^\pi$	Init. State Energy (keV)	Fin. State Energy (keV)	$M1$ -Transition Rate (Hz)	$E2$ -Transition Rate (Hz)
$5/2^+$	0	-	-	-
$3/2^+$	114	0	$7.81 \times 10^8$	$2.35 \times 10^6$
$1/2^+$	966	114	$2.03 \times 10^{10}$	$1.71 \times 10^{10}$
		0	-	$6.52 \times 10^{10}$
$3/2^+$	1981	966	$4.09 \times 10^{12}$	$5.25 \times 10^{10}$
		114	$3.88 \times 10^{12}$	$1.45 \times 10^{12}$
		0	$1.97 \times 10^{13}$	$5.02 \times 10^{11}$

$^{29}\text{S}$				
$J^\pi$	Init. State Energy (keV)	Fin. State Energy (keV)	$M1$ -Transition Rate (Hz)	$E2$ -Transition Rate (Hz)
$5/2^+$	0	-	-	-
$1/2^+$	1214	0	-	$1.06 \times 10^{11}$
$7/2^+$	1858	1214	-	-
		0	$2.15 \times 10^{13}$	$2.25 \times 10^{12}$
$3/2^+$	2076	1858	-	$8.94 \times 10^6$
		1214	$4.51 \times 10^{10}$	$2.54 \times 10^{10}$
		0	$8.53 \times 10^{12}$	$9.49 \times 10^{11}$
$3/2^+$	2704	2076	$1.43 \times 10^{11}$	$9.59 \times 10^6$
		1858	-	$2.20 \times 10^9$
		1214	$9.36 \times 10^{11}$	$4.91 \times 10^{10}$
		0	$6.74 \times 10^{12}$	$2.30 \times 10^{12}$
$5/2^+$	2993	2704	$9.67 \times 10^{10}$	$8.83 \times 10^6$
		2076	$2.24 \times 10^{12}$	$1.16 \times 10^{10}$
		1858	$5.47 \times 10^{12}$	$1.75 \times 10^7$
		1214	-	$5.15 \times 10^{11}$
		0	$3.16 \times 10^{12}$	$5.13 \times 10^{12}$
$5/2^+$	3095	2993	$1.11 \times 10^8$	$1.70 \times 10^5$
		2704	$9.67 \times 10^9$	$1.08 \times 10^7$
		2076	$1.83 \times 10^{12}$	$4.41 \times 10^9$
		1858	$5.48 \times 10^{12}$	$8.95 \times 10^{10}$
		1214	-	$7.75 \times 10^{11}$
		0	$2.83 \times 10^{12}$	$1.10 \times 10^{12}$

## 2.2 Reaction Mechanism

As discussed in Sec. 2.1.2, the ability to probe the single particle spectroscopic information is a crucial test of the nuclear wave-function. The earmark of a good spectroscopic probe is the ability to cleanly distinguish the effects of the reaction mechanism. It is because of this that nucleon knockout reactions are particularly favorable, as they assume a direct reaction with negligible residual interaction between the  $(A - 1)$  spectator core and the particle that instigated the nucleon removal. The effectiveness of knockout reactions for obtaining spectroscopic information is discussed in detail in Refs. [21, 4, 6].

The theoretical cross section for the removal of a particle from a single particle orbit with quantum numbers  $(n\ell j)$  from a nucleus of  $A$  nucleons to the residual core of  $(A - 1)$  nucleons in with total angular momentum and parity  $J^\pi$  is given by

$$\sigma_{th}(J^\pi, E_x) = \left(\frac{A}{A-1}\right)^N C^2 S_{SM}(n\ell j) \sigma_{sp}(n\ell j, S_n + E_x [J^\pi]), \quad (2.8)$$

in which  $S_n$  is the nucleon separation energy of the projectile,  $E_x$  is the excitation energy of the residual core state, and  $C^2 S_{SM}$  is the spectroscopic factor calculated from the shell model as discussed in Sec. 2.1.2. The  $A/(A - 1)$  term is raised to the main harmonic oscillator number  $N$ , which is two for the  $sd$ -shell as shown in Fig. 2.1. This term is a center of mass correction for the shell model spectroscopic factors as detailed in Ref. [19]. The  $\sigma_{sp}$  term is known as the single particle reaction cross section. Eq. 2.8 effectively factors the reaction into two components, one that contains all the single nucleon structure information in the spectroscopic factor, and another,  $\sigma_{sp}$  which contains the full reaction dependence of the total cross section. Eq. 2.8 also exemplifies the extreme dependence of having a reliable reaction theory in order to extract accurate spectroscopic information.

### 2.2.1 Single Nucleon Knockout Reactions

The eminent work on the single nucleon knockout reaction using inverse kinematics is in Ref. [4]. The effectiveness of this approach to extracting spectroscopic information from stable to very exotic nuclei has been discussed in detail in Refs. [4, 6, 21, 24, 20]. Single nucleon knockout reactions using inverse kinematics are particularly appealing for single particle reaction cross sections because the model is not as burdened by sensitive model parameterizations as other reaction models such as the Distorted Wave Born Approximation

(*DWBA*) as discussed in Ref. [6]. The foundation of the reaction theory is based on using an intermediate energy ( $> 50$  MeV/nucleon kinetic energy), heavy ion projectile on a highly absorptive target (typically  ${}^9\text{Be}$ ). Under these conditions, it is possible to use Glauber theory from Ref. [25], which makes two critical assumptions: first that the reaction is direct and sudden; and second, that the projectile and residual projectile-like ( $A - 1$ ) core obeys a straight-line (eikonal) trajectory. Using the highly absorptive target allows for the experimental selection of only glancing collisions in which the projectile core remains virtually unperturbed from its pre-collision state. Utilizing inverse kinematics, it is possible to monitor the relativistic residual ( $A - 1$ ) core after a nucleon removal.

The fundamental theory for the reaction cross sections is presented in Refs. [26, 4]. The single particle cross sections are the sum of two separate processes

$$\sigma_{sp} = \sigma_{str}^{th} + \sigma_{dif}^{th}, \quad (2.9)$$

where the first term is due to inelastic breakup (stripping) and the second is attributed to elastic breakup (diffractive dissociation). There is also a third reaction process of elastic break-up due to Coulomb interactions, however, as discussed in Ref. [4], with the choice of a low- $Z$  target, these effects are negligible. Both processes are calculated from the target-core and target-nucleon scattering matrices as described in Refs. [26, 4]. In each case the residual spectator core is left unperturbed by the target nucleus. Stripping is the case in which the removed nucleon is absorbed by the target, exciting the target from its ground state. In the case of diffractive dissociation, the nucleon is removed from the projectile, however the nucleon is not absorbed by the target nucleus. In the diffractive case, the nucleon proceeds forward with the same velocity as the projectile and the target nucleus is left in its ground state. A diagram of the reaction mechanism is presented in Fig. 2.8. The reaction models are calculated according the procedures laid out in Refs. [20, 6, 4], which parameterizes the reaction by a Woods-Saxon interaction potential that reproduces the effective binding energy ( $S_n + E_x$ ) and the nuclear matter densities of the projectile and target. The target is assumed to have a Gaussian nucleon density, while the residue and projectile densities are calculated using the Skyrme SkX calculations of Ref. [27]. The reaction model parameter sensitivity is discussed in Ref. [20]. The theoretical single particle cross sections for the  ${}^9\text{Be}({}^{26}\text{Si}, {}^{25}\text{Si})$  and the  ${}^9\text{Be}({}^{30}\text{S}, {}^{29}\text{S})$  reactions are given respectively in Table 2.5 and Table 2.6.

Table 2.5: Theoretical reaction cross sections for the  ${}^9\text{Be}({}^{26}\text{Si}, {}^{25}\text{Si})$  reaction. The individual stripping and diffractive break-up components, as well as their summed single particle reaction cross section. The spectroscopic factors are taken from the USDB shell model calculations from Table 2.1.

${}^9\text{Be}({}^{26}\text{Si}, {}^{25}\text{Si})$					
$E_{\text{level}}$ (keV)	$\sigma_{str}^{th}$ (mb)	$\sigma_{diff}^{th}$ (mb)	$\sigma_{sp}$ (mb)	$C^2S_{SM}$	$\sigma_{th}$ (mb)
1909	10.09	2.01	12.10	0.18	2.36
821	10.95	2.49	13.45	0.25	3.64
40	10.52	2.15	12.68	0.12	1.65
0 ( <i>G.S.</i> )	11.20	2.33	13.54	2.73	40.0

Table 2.6: Theoretical reaction cross sections for the  ${}^9\text{Be}({}^{30}\text{S}, {}^{29}\text{S})$  reaction. The individual stripping and diffractive break-up components, as well as their summed single particle reaction cross section. The spectroscopic factors are taken from the USDB shell model calculations from Table 2.2.

${}^9\text{Be}({}^{30}\text{S}, {}^{29}\text{S})$					
$E_{\text{level}}$ (keV)	$\sigma_{str}^{th}$ (mb)	$\sigma_{diff}^{th}$ (mb)	$\sigma_{sp}$ (mb)	$C^2S_{SM}$	$\sigma_{th}$ (mb)
2887	8.96	1.93	10.89	0.80	9.32
1222	10.14	2.54	12.68	0.36	4.89
0 ( <i>G.S.</i> )	9.64	2.17	11.80	3.63	45.9

### 2.2.1.1 Longitudinal Momentum Distribution

The parallel momentum content of the residual core, as described in Refs. [4, 28], is sensitive to the orbital angular momentum ( $\ell$ ) of the removed nucleon from the projectile. The momentum content of the transferred nucleon  $\vec{k}_n$  is given from the momentum conservation equation

$$\vec{k}_n = \frac{A-1}{A}\vec{k}_A - \vec{k}_{A-1}, \quad (2.10)$$

where the first term is the center of mass corrected momentum of the projectile and the second term is the momentum of the residual core. The momentum distributions are calculated using a black disk model for the residue-target and nucleon-target systems as described in Refs. [28, 29]. The calculations for the longitudinal momentum distributions were performed as described in Refs. [30].

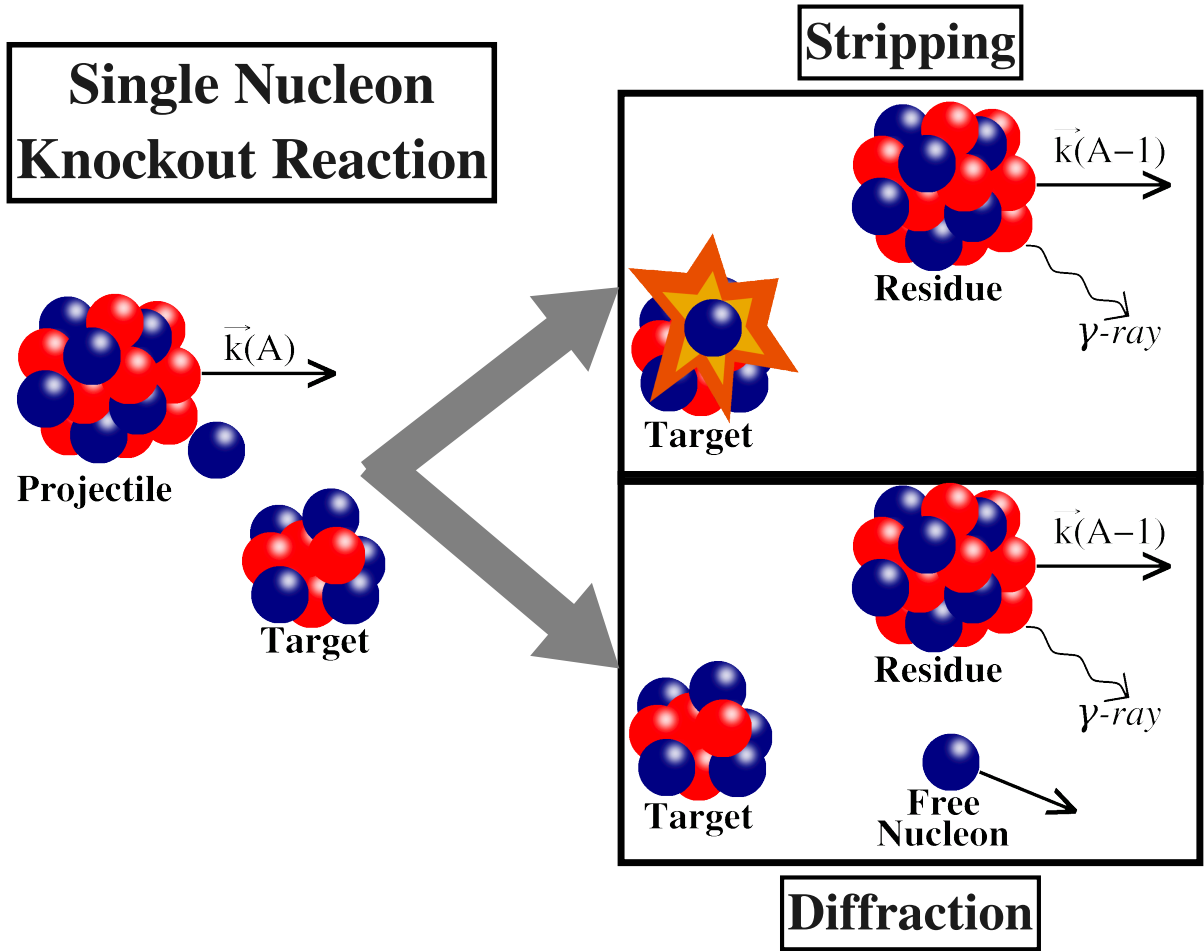


Figure 2.8: A diagram of the processes involved in the single nucleon knockout reaction. The initial projectile with momentum  $\vec{k}(A)$  and target system is shown on the left. In the stripping reaction process (top right), the removed nucleon is absorbed by the target and the residual core proceeds in a straight line trajectory with momentum  $\vec{k}(A - 1)$  and possibly will emit a  $\gamma$ -ray if the core is not in its ground state. In the diffraction reaction process (bottom right), the removed nucleon proceeds in with relatively the same velocity as the residual core, leaving the target in its ground state.

# CHAPTER 3

## EXPERIMENTAL DETAILS

The following sections will provide information on the equipment and measurement techniques used in the experiments. The equipment and techniques used to produce the exotic beams of  $^{26}\text{Si}$  and  $^{30}\text{S}$  will be discussed first in Sec. 3.1. Next, the methods and devices used to identify and make relevant measurements of the reaction products will be discussed. The particle detection system will be described in Sec. 3.2 and then the  $\gamma$ -ray analysis system in Sec. 3.3, followed by a brief discussion in Sec. 3.4 of the data acquisition trigger and timing system implemented for particle- $\gamma$  coincidence measurements.

### 3.1 Rare Isotope Beam Production

The following sections will cover the facilities, equipment, and techniques used to produce the beams of  $^{26}\text{Si}$  and  $^{30}\text{S}$ . The NSCL has a history of being one of the worlds leading rare isotope beam facilities. The NSCL was also the birthplace of the world's first superconducting cyclotron. The experiments made use of the Coupled Cyclotron Facility and the A1900 fragment separator to produce the relativistic radioactive beams of  $^{26}\text{Si}$  and  $^{30}\text{S}$ .

#### 3.1.1 Coupled Cyclotron Facility

The Coupled Cyclotron Facility at the NSCL was used to produce the primary beam for the experiment. Cyclotrons use an alternating electric field to accelerate particles while also using strong magnetic fields to force the particles into outward spiraling orbits. A diagram of the first cyclotron is shown in Fig. 3.1. The particles are injected close to the center of the cyclotron and gain energy by crossing the electric field. Once the particles have crossed the electric field, they enter a magnetic field which causes them to undergo a circular motion. The magnetic fields steer the particles back across the electric field, which

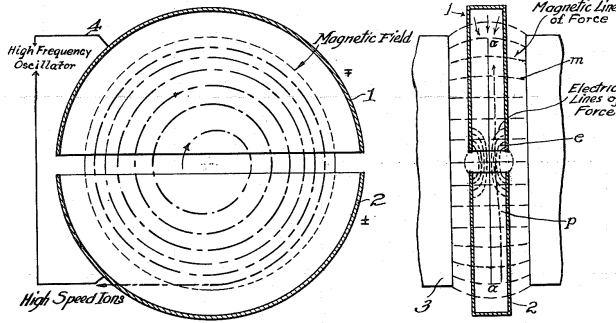


Figure 3.1: Schematic of a cyclotron from the original cyclotron patent filing of Ernest Lawrence in 1932. The design of the K500 and K1200 is modified to account for relativistic effects, however the basic concept is still the same.

has by this time switched directions to be  $180^\circ$  from the previous pass. The particles now undergo another acceleration through the electric field and once again enter the magnetic field, however because of the increase in kinetic energy, the particles make a wider arc in the magnetic field. This process is continued until eventually the particles reach the outer edges of the cyclotron and are allowed to exit the accelerator into the beam line.

The Coupled Cyclotron Facility uses two cyclotrons to accelerate ions as shown in Fig. 3.2. The initial beam particles are fed into the smaller K500 cyclotron, and then injected from the K500 into the K1200 cyclotron for further acceleration. The beam leaving the K1200 is often referred to as the primary beam. Both experiments used a primary beam of 150 MeV/nucleon  $^{36}\text{Ar}$  particles to create the secondary beams.

### 3.1.2 A1900 Fragment Separator

The primary beam impinges on a thick  $^9\text{Be}$  production target.  $^9\text{Be}$  is chosen because of its charge and target density. Nuclear collisions between the primary beam and the production target create a large number of secondary nuclear species. A primary function of an exotic beam facility is to effectively create beams of rare and short lived nuclei progressively further from the valley of  $\beta$ -stability. One obstacle to overcome is picking out the relatively small number of particles of interest from the total number of particles after the production target, which is a mixture of energy dispersed primary beam particles and all the secondary nuclear species. The A1900 separator [31] filters the secondary beam to allow only a few selected

nuclear species to advance. The A1900 is composed of four superconducting dipole magnets, and an energy degrading wedge to filter the beam, 24 superconducting quadrupoles for focusing and monitors to check the beam between the filters as seen in Fig. 3.2. The Lorentz

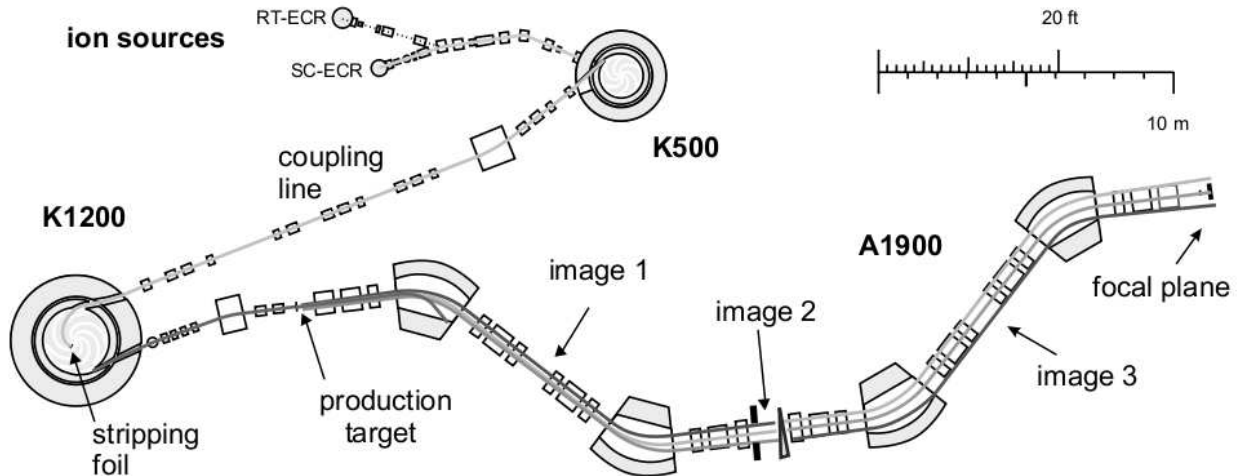


Figure 3.2: A schematic diagram of the ion source, K500 and K1200 cyclotrons, and the A1900 fragment separator. The  ${}^9\text{Be}$  production target is located before the first A1900 dipole. The energy degrading wedge is located in the second image position between the second and third A1900 dipoles. The focal plane of the A1900 is referred to as the extended focal plane when discussing it in use with the S800 Spectrometer. Figure from Ref. [31].

force equations of motion of a relativistic charged particle with electric charge  $q$ , velocity as a ratio to the speed of light  $\vec{\beta} = \vec{v}/c$ , momentum  $\vec{p}$ , and energy  $\epsilon$  passing through external electric ( $\vec{E}$ ) and magnetic ( $\vec{B}$ ) fields and is given by the following equations:

$$\frac{d\vec{p}}{dt} = q \left( \vec{E} + \vec{\beta} \times \vec{B} \right), \quad (3.1)$$

$$\frac{d\epsilon}{dt} = q \vec{v} \cdot \vec{E}. \quad (3.2)$$

For the case of a charged particle passing through a magnetic dipole with the magnetic field always perpendicular to the particles momentum vector, the right hand side of Eq. 3.2 becomes zero stating that energy is conserved, and Eq. 3.1 becomes

$$\frac{dp_{\perp}}{dt} = q\beta B. \quad (3.3)$$

Following Ref. [32], Eq. 3.3 can be evaluated in terms of

$$p_{\perp} = qB\rho, \quad (3.4)$$

where  $\rho$  is the particles bending radius. Using the relationships

$$\gamma = \frac{1}{\sqrt{1 - \beta^2}}, \text{ and} \quad (3.5)$$

$$\vec{\mathbf{p}} = \gamma m \vec{\beta} c, \quad (3.6)$$

Eq. 3.4 can be written as

$$B\rho = \frac{\gamma m \beta c}{q}. \quad (3.7)$$

$B\rho$  is also known as an isotopic beams rigidity. Eq. 3.7, shows that for a dipole with a set magnetic field strength, the bending radius of a charged particle is proportional to its momentum to charge ratio.

The A1900's dipoles use the Lorentz force to separate secondary beam particles based on rigidity. The first pair of dipoles are used to disperse the initial reaction products and narrow the secondary beam down to a single selected momentum to charge ratio value. The beam particles that are too different in rigidity are attenuated out of the beam. The isotopic filtering is improved with an energy degrading wedge placed between the second and third dipole. The energy loss of an isotope traveling through the wedge is given by

$$-\frac{d\epsilon}{dx} = q^2 \lambda(\beta), \quad (3.8)$$

where  $\lambda(\beta)$  is a function of the particles velocity and  $q$  is the particles charge. The value of  $\lambda(\beta)$  is often taken from empirical data when available or the relativistic Bethe-Bloch formula (Ref. [13, 33]) in which

$$\lambda(\beta) \propto \frac{1}{\beta^2} \left[ \ln \left( \frac{2m_e \beta^2 c^2}{I(1 - \beta^2)} \right) - \beta^2 \right], \quad (3.9)$$

where  $I$  is the average excitation of the wedge target particles and  $m_e$  is the electron mass. This energy loss will cause isotopes with the same momentum to charge ratio but different masses to undergo different momentum shifts. This additional momentum shift changes the rigidity of the remaining species enough that a second pair of dispersive dipoles will create acceptable isotopic separation. After leaving the fourth dipole, the secondary beam is monitored by a fast timing scintillator in the A1900's focal plane. The A1900's focal plane is referred to as the extended focal plane when used with the S800, in which case the extended focal plane scintillator is used for time-of-flight measurements as well as beam flux monitoring.

## 3.2 The S800 Spectrograph

The S800 is a large-acceptance, high resolution spectrograph for use in nuclear experiments at the NSCL. The S800 is composed of two main sections: the analysis line and the spectrograph as depicted in Fig. 3.3. The two sections are divided so that the analysis line measures

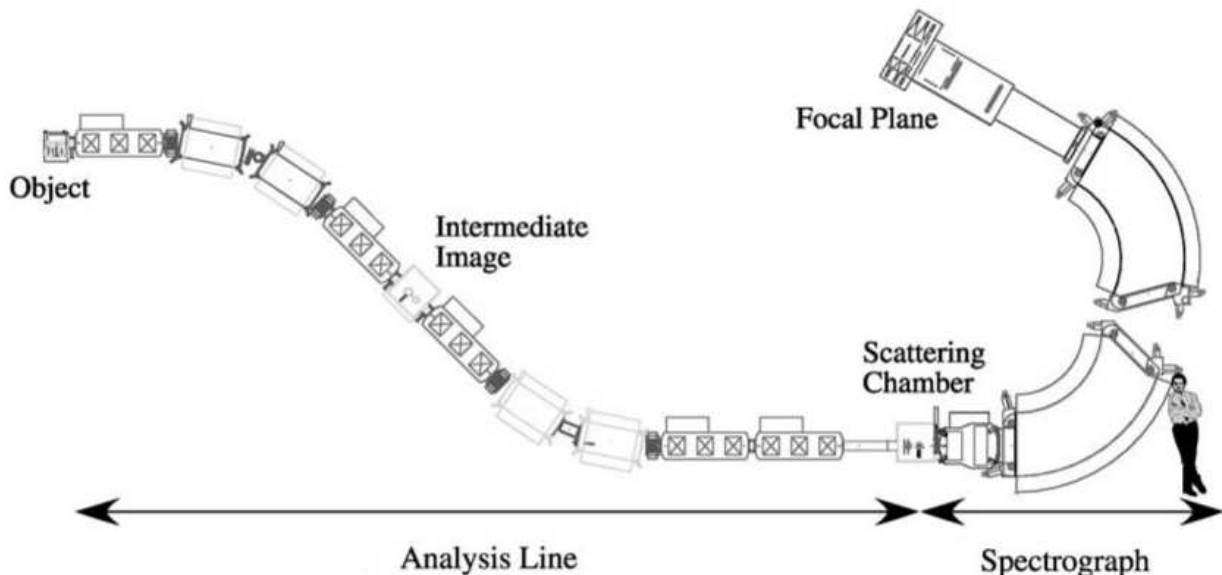


Figure 3.3: A diagram of the S800 large acceptance spectrometer. The secondary target was located at the S800 pivot point marked as the Scattering Chamber area above. The experiments used a fast timing scintillator in the Object position, the SeGA around the Scattering Chamber section, and the compliment of detectors in the Focal Plane. Figure from Ref. [34].

the pre-secondary target beam and the spectrograph measures the post-secondary target components. The S800 has a solid angle acceptance of 20 msr ( $7^\circ$  dispersive and  $10^\circ$  non-dispersive) and has a momentum acceptance of 5% with a maximum rigidity of 4.9 Tm in the analysis line and 4 Tm in the spectrograph[34]. The mode of operation employed is referred to by Ref. [34] as dispersion matched mode. In this mode the secondary beam is momentum dispersed across the target due to analysis line steering magnets. The dispersion across the target face is approximately 10 cm/% of the momentum dispersion ratio, and the momentum acceptance in the analysis line is limited to 0.5%. The dispersion matched mode also allows for the highest energy resolution of around 1 part in 5000 for a 1 mm beam spot,

although energy resolutions of 1 part in 2000 are more common in practice. The following sections will cover the detectors that make up the analysis line and the spectrograph, with attention given to the S800's focal plane detectors. This will be followed by a discussion of the measurement techniques used for particle identification, reaction rate, and momentum distribution measurements used in the experiments.

### 3.2.1 Analysis Line

The S800's analysis line is used for measuring and monitoring the incoming cocktail beam from the A1900. There is a 30 meter separation between the extended focal plane of the A1900 in Fig. 3.2 and the object position of the S800. There is a fast timing scintillator located at the object position before the first bend of the S800's analysis line. This scintillator is referred to as the object scintillator and is used for monitoring beam intensity and transmission efficiency, and taking time-of-flight measurements. There is also a pair of parallel plate avalanche counters (PPACs) in series located in the intermediate image location. The PPAC detectors can be used for profiling the incident cocktail beam position and trajectory, but the efficiency of these detectors is a limiting factor and the beam's dispersion profile on the target was small enough that the information from the PPACs was superfluous (which is common when running in the dispersion matched mode), so while they were present during the experiment, they were not needed or used for any of the current experimental analysis.

### 3.2.2 Spectrograph and Focal Plane Detectors

The spectrograph section of the S800 is two main parts: the actual magnetic spectrometer and the focal plane detectors. The projectile-like post-secondary target reaction residues enter the spectrometer into two superconducting quadrupoles followed by two  $75^\circ$  superconducting dipoles as depicted in Fig. 3.3. The magnetic field direction of the dipoles is in the horizontal plane, so as to cause the residues to be bent in an upward arc in the vertical direction. The residues are separated in the spectrometer by the Lorentz force as described in Sec. 3.1.2, however at this point it is useful to restate Eq. 3.7 in terms of the number of protons in the nuclei  $Z$  and the residue's momentum component parallel to the beam

direction  $p_{\parallel}$ ,

$$B\rho = \frac{p_{\parallel}}{Ze}. \quad (3.10)$$

The spectrometer's magnetic fields are tuned to maximize the residue of interest in the S800's focal plane.

The focal plane of the S800 consist of a series of particle detectors as depicted in Fig. 3.4. The S800's focal plane detection system as described in Ref. [35] consist of three main

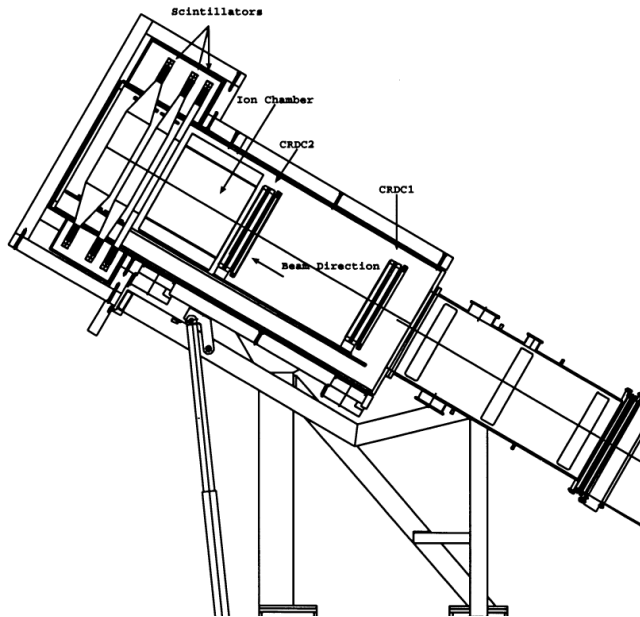


Figure 3.4: A diagram of the S800's focal plane detector system. The S800 focal plane is the last section of the experimental beam line and is located after the spectrometer. The experiments used CRDC1, CRDC2, the Ion Chamber, and the first scintillator. The two additional scintillators at the end of the beam line were not needed for the experiments. Figure from Ref. [35].

components: a pair of position sensitive cathode readout drift counters (CRDCs), followed by an ionization chamber, and then a set of four fast timing scintillators. All three components will be discussed in the following sections.

### 3.2.2.1 Cathode Readout Drift Counters

The CRDCs are a crucial component of the particle identification and the momentum distribution measurements. A CRDC allows for the simultaneous measurement of a particle's

x and y position within the detectors' interaction region. The basic construction is described in Ref. [36]. A CRDC combines aspects of several ionization detectors such as drift chambers, multiwire proportional chambers, and time projection chambers. Each CRDC has an active area of 59 cm in the dispersive plane (x), 30 cm in the non-dispersive (y), and a depth of 1.5 cm. The CRDC has 224 cathode pads aligned in series along the edges in the dispersive direction. The induced signal on each pad is read out individually. The ionization gas is 140 Torr of 80% CF<sub>4</sub> and 20% C<sub>4</sub>H<sub>10</sub>, which was chosen for its high drift velocity and low electron avalanche spread [35].

As the reaction residues pass through the active region of the CRDC, they ionize the molecules in the fill gas. The electrons from these ionizations are collected by the cathode pads along the dispersive edge of the detector. The spread of the ionization trail parallel to the dispersive edge is approximated as a Gaussian distribution with the largest amount of ionization occurring in line with the residue's x-position when it passed through the detector. This ionization spread is seen as a distribution of collected charge across the pads, with the pad corresponding to the particles x-position receiving the largest amount of charge, and the neighbors directly above and below it receiving slightly less than the centroid pad, and so forth propagated outward from the centroid pad. A center of gravity method, often used in multiwire proportional chambers [37], was used to determine the residue's x-position. The value of x was determined as

$$x = \frac{\sum_i b_i Q_i x_i}{\sum_j b_j Q_j}, \quad (3.11)$$

where the summation is carried out over all valid working pads,  $x_i$  is the center of the  $i^{\text{th}}$  pads position from the center of the detector,  $Q_i$  is the charge collected in that pad, and  $b_i$  is a scaling factor used to correct for measured discrepancies between the readouts from the different pads. The correction factors  $b_i$  for each pad were determined by looking at data runs and scaling each pad so that the average pulse height for the cocktail beam a reasonable distribution. A scaler offset was applied to each pad before any data was collected by pulsing the electric field and setting an appropriate rough offset to each pad. Fig. 3.5 shows the pad charge collections before and after the calibrations. It can also be seen in Fig. 3.5 that there are several pads in which the readouts were unreliable, these pads were marked as being bad pads and omitted from being used in any calculation. The large contiguous section of dead pads close to the center of CRDC2 is of some consequence for both efficiency corrections

and longitudinal momentum distribution measurements. The y-position of the residue in

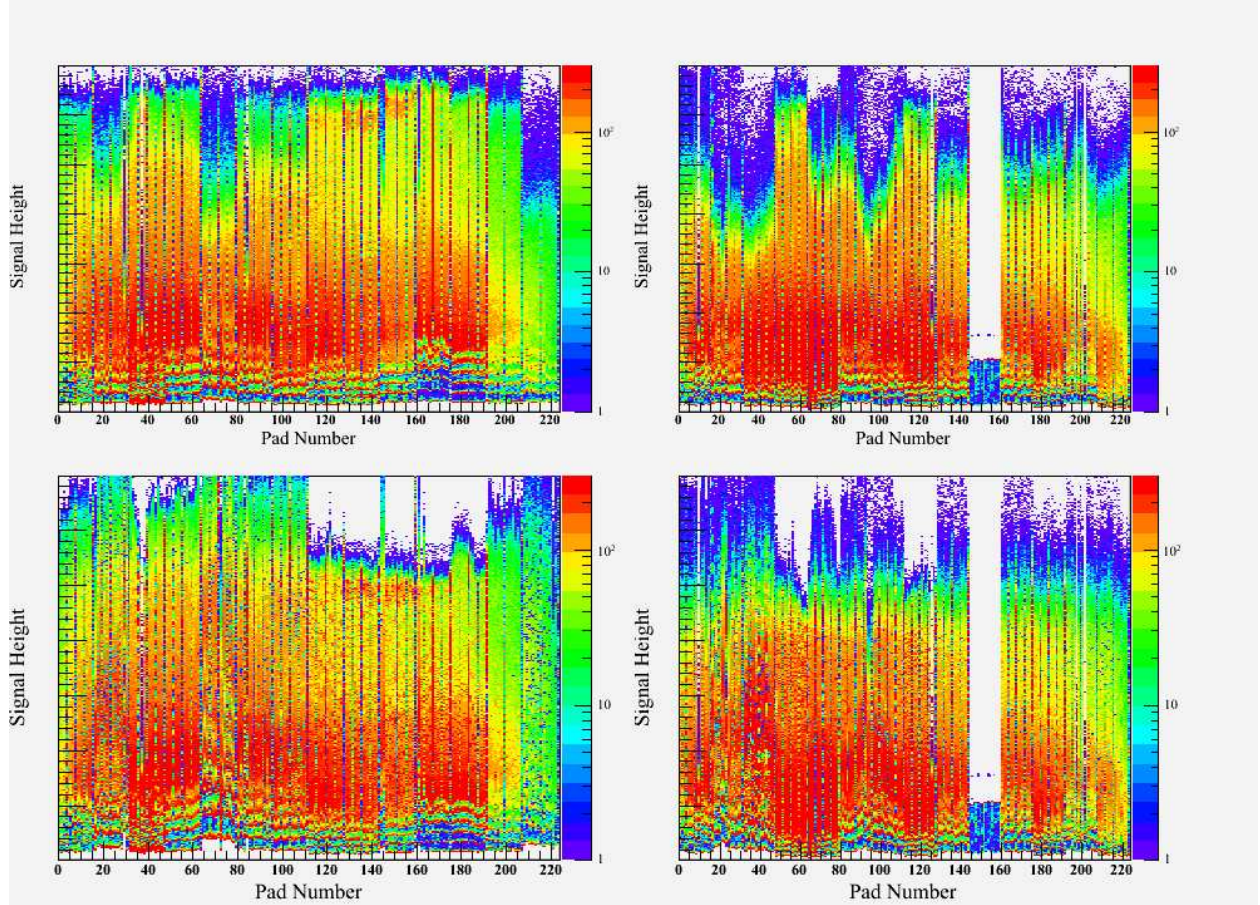


Figure 3.5: A comparison of the CRDC pad charge collections. The histograms are set-up so the horizontal axis is the pad number and the vertical axis is the signal output. Progressing clockwise from top-left: uncalibrated CRDC1, uncalibrated CRDC2, calibrated CRDC2, and calibrated CRDC1. This data was taken for the ungated  $^{26}\text{Si}$  cocktail beam.

the CRDC is calculated from the drift time of the electrons in the CRDC. A timing signal from the scintillator at the end of the S800's focal plane is used to determine the drift time of the electrons. The time difference between the scintillator's signal and the CRDC's pad readout determines the amount of time it took the ionized electrons to move toward the cathodes, and since the drift velocity of electrons in the gas is mostly uniform, the drift time is proportional to the distance away from the pad, which is the position in the non-dispersive beam direction.

The x and y position measurements are then each calibrated by a scaler and an additive

correction factor for each direction. A removable beam mask shown in Fig. 3.6 is used to make the final x and y position calibrations. The mask is constructed out a thick plate

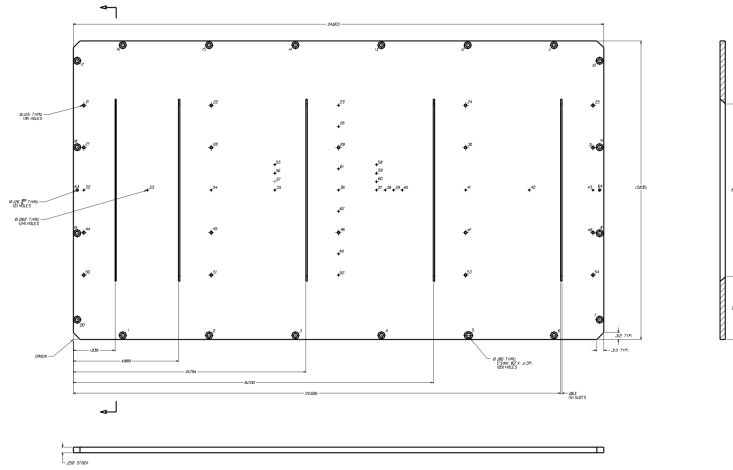


Figure 3.6: A diagram of the CRDC mask used to calibrate the position coordinates of the CRDC. There are two removable masks in the beamline, one directly in front of CRDC1 and the other in front of CRDC2. The precision drilled holes allow for a very small amount of beam to pass each hole.

that nearly completely attenuates any incident beam and is positioned directly in front of the CRDC to make calibration measurements. The mask has several small holes at precise locations that allow the beam to pass through to the CRDC as can be seen in Fig. 3.7. The  $(x,y)$  locations of the mask projections onto the CRDC are used to calibrate the CRDC x and y measurements so they align with the actual  $(x,y)$  positions of the holes on the mask. Each CRDC has a position resolution of roughly 0.5 mm in both the dispersive and non-dispersive planes. The section of dead pads in CRDC2 shown in Fig. 3.5 caused large blindspot in the CRDC2 x measurements, and also caused an artificial inflation of the x coordinates directly on the edges of this blind spot as seen in Fig. 3.8. In order to correct for the counting inflation around the dead region, an exclusion gate was applied to all particle events to ignore any events that were in coincidence with the events in the inflation areas around the dead region. The effect of this can be thought of as a decrease CRDC2's detection efficiency and is taken into account in the efficiency calculations.

The S800's focal plane uses two CRDC's located 1 meter apart along the beam line. The upstream CRDC is labeled as CRDC1 and the downstream is labeled as CRDC2. The

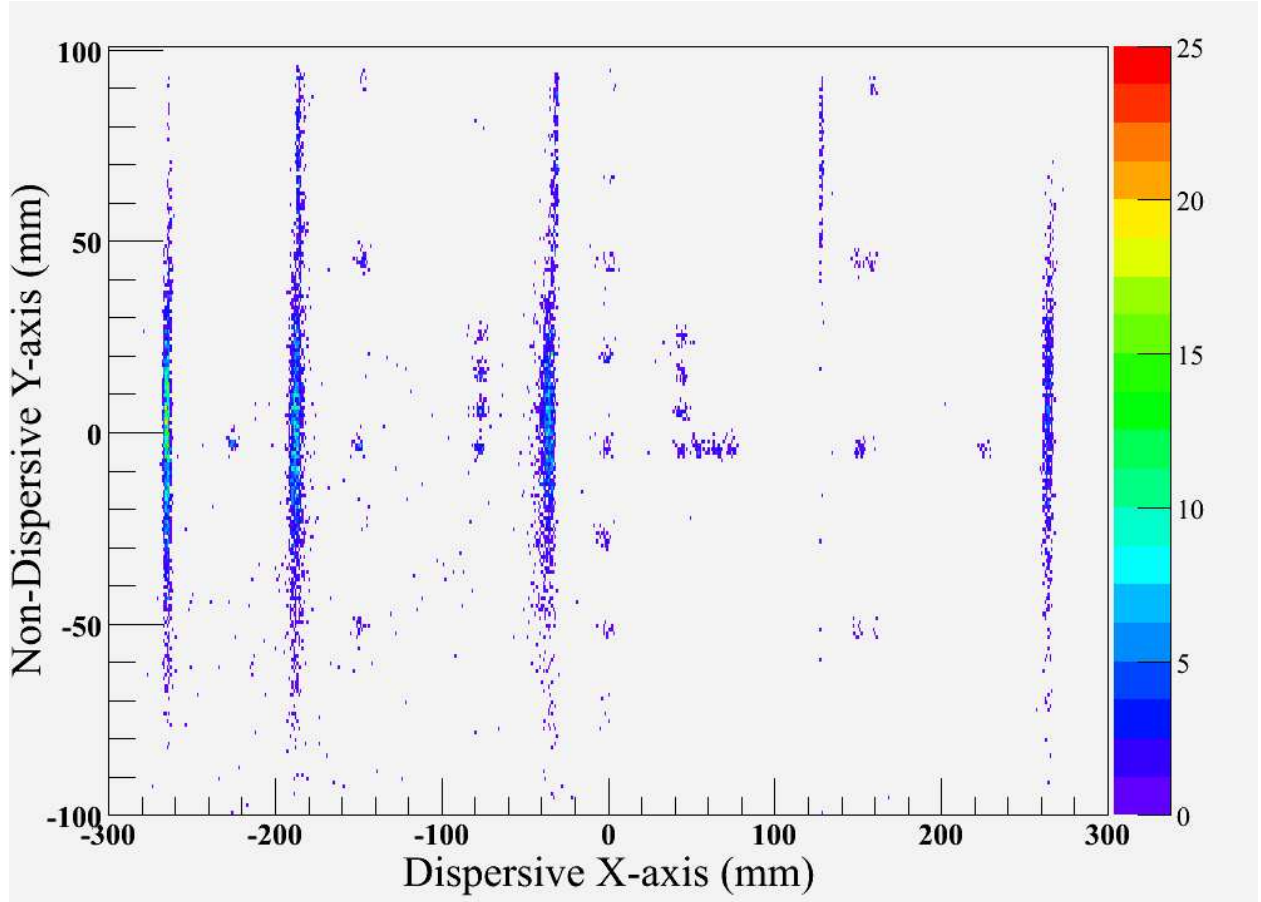


Figure 3.7: A CRDC mask calibration histogram. The horizontal axis is the CRDC x position (dispersive axis) and the vertical is the y position (non-dispersive axis). Notice how the pattern of detected particles matches that of Fig. 3.6. The x and y axis are both in millimeters.

trajectory of each incident residue can be determined using the calibrated x and y positions as it passed through both CRDCs. Using the physical spacing between the two CRDC detectors, for an event that is detected in both the CRDC1 and CRDC2, using simple trigonometry the detected particles dispersive and non-dispersive trajectory angles can be calculated. This dead region also affects the dispersive angle in the focal plane. While the angle is not as effected when allowing the inflated edge counts to be included, once they are removed, an apparent dip becomes present as shown in Fig. 3.9. The drawback of the CRDC detectors is that it typically takes up to  $20 \mu\text{s}$  per event to readout. This places a limitation on the maximum beam rate in the focal plane to around 5 kHz before the CRDC detection

efficiency becomes an issue.

### 3.2.2.2 Longitudinal Momentum Distributions

Using the two angles and two positions measured by the CRDCs, it is now possible to reconstruct the residue's trajectory all the way back to the secondary target. The program COSY Infinity [38] is used to create high-order maps of the beam optics and field dynamics of the S800's spectrograph section. The COSY mapping function is created from the magnetic field settings of the spectrometer and the residue's mass, velocity, and charge. This mapping function  $\mathcal{S}^{-1}$  takes the parameters measured from the CRDCs positions  $x_r$  and  $y_r$  from CRDC1 and the dispersive angle  $a_r$ , and the non-dispersive angle  $b_r$ , and maps them back to the residue's parameters of interest at the target given by [34, 39],

$$\begin{pmatrix} a_t \\ x_t \\ b_t \\ d_t \end{pmatrix} = \mathcal{S}^{-1} \begin{pmatrix} y_r \\ a_r \\ x_r \\ b_r \end{pmatrix}, \quad (3.12)$$

where  $x_t$  is the dispersive axis position coordinate at the target,  $a_t$  is the residues dispersive angle at the target, and  $d_t$  is the residues energy deviation from the spectrometer's central energy ( $d_t = \Delta E/E$ ), the value of  $y_t$  is of little interest and since it is mostly unaffected by the magnetic field, it is not considered a of much consequence in the mapping function. The CRDC detectors allow for a full beam trajectory reconstruction as well as gaining information on the residues energy dispersion from the mean. The longitudinal momentum distribution is the component of the residue's momentum parallel to the direction of motion and is determined from the parameter  $d_t$  in Eq. 3.12. The transformation between the parameter  $d_t$  and the lab frame longitudinal momentum  $p_{\parallel}$  is given by

$$p_{\parallel} = p_o \left( 1 + \frac{\gamma}{1 + \gamma} d_t \right), \quad (3.13)$$

where  $\gamma$  is from the normal relativistic correction term and  $p_o$  is the centrally focused momentum value. The velocity used for both  $\gamma$  and  $p_o$  is determined by taking the magnetic rigidity  $B\rho$  of the S800 spectrometer and solving Eq. 3.7 for the velocity of the residue of interest.  $p_o$  is then determined using Eq. 3.6, and corresponds to the residue momentum values that should ideally cross both CRDCs in the center with no angular dispersion.

The problems that arise from the dead region in CRDC2 result in a large dip in the momentum distributions. An effort was made to steer the residues away from the bad region

as much as possible, but due to the location it was impossible to avoid it having large effects on the momentum distributions.

### 3.2.2.3 Ionization Chamber

The ionization chamber is located directly after CRDC2. The main function of the ion chamber is to measure the energy loss of the residues as they pass through the fill gas, which is composed of P10 gas (90% Ar and 10% CH<sub>4</sub> Methane) at 140 Torr. The ion chamber's anodes are segmented into 16 1 in. pieces that lie perpendicular to the residues path. The anodes are also shielded by a Frisch grid from the main interaction region. The anode segmentation and the grid are both used to decrease the noise levels in the ion chambers charge collection readout. Looking back at Eq. 3.8, the amount of energy lost in the fill gas is strongly dependent on the charge of the residue, and since the residues are fully stripped of all electrons  $q = Ze$ , where  $Z$  is the number of protons in the isotope. Summing the charge collected on the ionization chambers anodes gives a direct measurement of the energy lost in the fill gas which is approximately proportional to  $Z^2$ . The ionization chamber readout effectively provides a measurement of the number of protons  $Z$  in the residue as can be seen in Fig. 3.10 and Fig. 3.11.

At the beam rates used in the present experiments, the ionization chambers detection efficiency is approximately 100%. Because of this, the ionization chamber was used as the standard for measuring the relative efficiency of the other particle detectors.

### 3.2.2.4 Fast Timing Scintillators for Time of Flight Measurements

The last group of detectors in the S800's focal plane are four plastic scintillators of thicknesses from upstream to downstream of 3 mm, 5 cm, 10 cm and 20 cm. The scintillators are used for timing measurements. As stated previously, only the front 3 mm scintillator was needed for the experiments. Also discussed previously, the signal from the scintillator was used to measure the CRDC electron drift time. The main function of the scintillator is in conjunction with the other scintillators located in the S800's analysis line object point and the extended focal plane scintillator at the end of the A1900. Time-of-flight measurements are made by comparing the time differences between the scintillator signals. The beam and residual particles are filtered by the magnetic dipoles such that only particles with similar momentum to charge ratios are allowed. Since the time-of-flight is dependent solely on the particle's

velocity, the time-of-flight measurements effectively act to distinguish the total mass  $A$  of the particles being measured.

### 3.2.3 Particle Identification

The particle identification of both the reaction residues and the incident secondary beam particles was done on an even-by-event basis. The incident secondary beam particles were identified from time-of-flight measurements made between the extended focal plane scintillator and the scintillator at the S800's object point. The time-of-flight measurements for  $^{26}\text{Si}$  and  $^{30}\text{S}$  are shown in Fig. 3.12 and Fig. 3.13. Since only the relative time-of-flight differences were needed to separate out the isotopic masses, there was no need to calculate the time-of-flight in real units, therefore arbitrary units are used for all time-of-flight measurements.

Because of the large number of nuclear species created in the reactions, the identification of the projectile-like residual reaction isotopes is a more complicated matter than the incident beam identification. The proton number of the residue is identified by the energy lost in the ionization chamber as described in Sec. 3.2.2.3. The time difference between the secondary beam particle entering the scintillator at the object point and the reaction residue entering the scintillator in the S800's focal plane is consistent for specific reaction channels and is also comparable to the time-of-flight of the residue from the target to the focal plane. However, the S800 exaggerates the vertical dispersion of like-residues proportional to the longitudinal momentum. This causes a larger flight path difference in residual particle groups of interest, which in turn causes the time-of-flight measurement of the residues to become too smeared between the different residue mass groups to be effective. To solve this problem, the dispersive angle in the focal plane as measured in the CRDCs is used to correct the time-of-flight spectrum for the path differences. Adding the path correction term to the time-of-flight takes the following form:

$$(TOF) = (OBJ)_t - (FP)_t + \alpha\theta_{FP}, \quad (3.14)$$

where  $\theta_{FP}$  is the angle in the focal plane,  $\alpha$  is the calibration constant, and  $(OBJ)_t$  and  $(FP)_t$  are respectively the object scintillator and focal plane scintillator timing signals. The method used to adjust the calibration constant is depicted in Fig. 3.14. The different vertical groupings in Fig. 3.14 correspond to residues with the same mass. The  $\alpha$  correction term

is adjusted until the mass groups are aligned vertically. The same correction term was used for all the experimental trials.

At this point it is possible to construct a two-dimensional particle identification (PID) spectrum by plotting the energy loss in the ionization chamber versus the corrected time-of-flight as shown in Fig. 3.15. Based on what has been established in this Section and Sec. 3.2.2.3, this particle identification spectrum is effectively plotting relative proton number ( $Z$ ) on the vertical and total atomic mass number ( $A$ ) on the horizontal where nuclei of the same  $A$  and  $Z$  cluster together in distinguishable groupings.

For fragmentation reaction data, the incident secondary beam is identified from the time-of-flight spectrum and the fragmentation reaction residue is identified from the particle identification spectrum. This allows for an unambiguous event-by-event identification of the  ${}^9\text{Be}({}^{26}\text{Si}, {}^{25}\text{Si})$  and  ${}^9\text{Be}({}^{30}\text{S}, {}^{29}\text{S})$  reactions. Focusing the unreacted secondary beam into the focal plane, it is also possible to use the PID spectrum to identify the particle composition of the beam.

### 3.2.4 Particle Detection Efficiency

One of the experimental goals is to determine the inclusive cross sections of the single neutron knockout reactions. In order to perform this calculation, it is imperative to have an accurate grasp of the absolute number of reaction residues of interest that were created and the total number of beam particles incident on the target. For the limited counting rate of the focal plane CRDC detectors, the focal plane scintillator's and ion chamber's counting rate efficiencies are considered to be approximately 100% for the incident particle energies and charge states in the present experiment. Using the ion chamber as the standard, the efficiencies of all the other particle detectors used in the experimental set-up can be calibrated by creating a coincidence logic gate around the region of interest in the ion chamber's energy loss spectrum, the detection efficiency of all other detectors can be determined as the ratio of the number of counts seen in coincidence with the ion chamber logic gate in that detector and the total number of events detected in the ion chamber's gated region. So the general formula for an S800 detector's efficiency is

$$\varepsilon_i = \frac{\textit{Gated Counts in Detector } i}{\textit{Counts in IC Gate}}. \quad (3.15)$$

The efficiency of the combined CRDC detectors required a additional consideration due

to the large section of dead pads close to the center of CRDC2. Because all of the events incident in this dead region were sacrificed, a significant amount of detection efficiency is lost. Since the calculations of significance are dependent on having both CRDC1 and CRDC2 tracking data, the efficiency was calculated as described except for the combined CRDC detectors. The particle efficiency loss due to the CRDC dead region is highly dependent on the trajectory profile of the residue of interest. In order to correct for the counts loss due to the dead region and the small number of counts lost from the limited acceptance angle of the S800, a smooth function is fit to the  $d_t$  energy dispersion spectrum calculated from the inverse map. The function was determined as a symmetrical set of Gaussian functions summed together and fit to the good regions of the  $d_t$  plots in coincidence with the residues of interest. The number of Gaussian functions was allowed to vary, but the overall shape of the fitted function was forced to be symmetric. Once a good fit was made, the ratio of the number of counts in the histogram to the integral of the fitted function was used as the correction factor ( $\eta_{crdc}$ ) for the number of particle events detected in the CRDCs. The corrected total CRDC efficiency is determined as

$$\varepsilon_{crdc} = \eta_{crdc} \times \varepsilon_{crdc1} \times \varepsilon_{crdc2}, \quad (3.16)$$

where  $\varepsilon_{crdc1}$  and  $\varepsilon_{crdc2}$  are the respective efficiencies of CRDC1 and CRDC2 from Eq. 3.15.

Typically the incident beam rate is monitored by the extended focal plane (XFP) and object plane (OBJ) scintillators. Since the secondary beam is a cocktail beam, the actual number of projectiles of interest is only a small fraction of the total number of beam particles that impinge on the secondary target. To determine the number of projectiles of interest per count in the XFP and OBJ scintillators, attenuated unreacted cocktail beams were focused for each reaction in the S800 and using the particle identification techniques as already described, the number of projectiles of interest to the total number of incident particles was determined along with the number of projectiles of interest on the target per event in the XFP and OBJ scintillators. Unfortunately it was discovered that the XFP scintillator's detection efficiency was degrading at a rate too rapid for it to be used as a consistent beam monitor for the course of an entire data run, so only the OBJ scintillator was used for monitoring the incident beam flux.

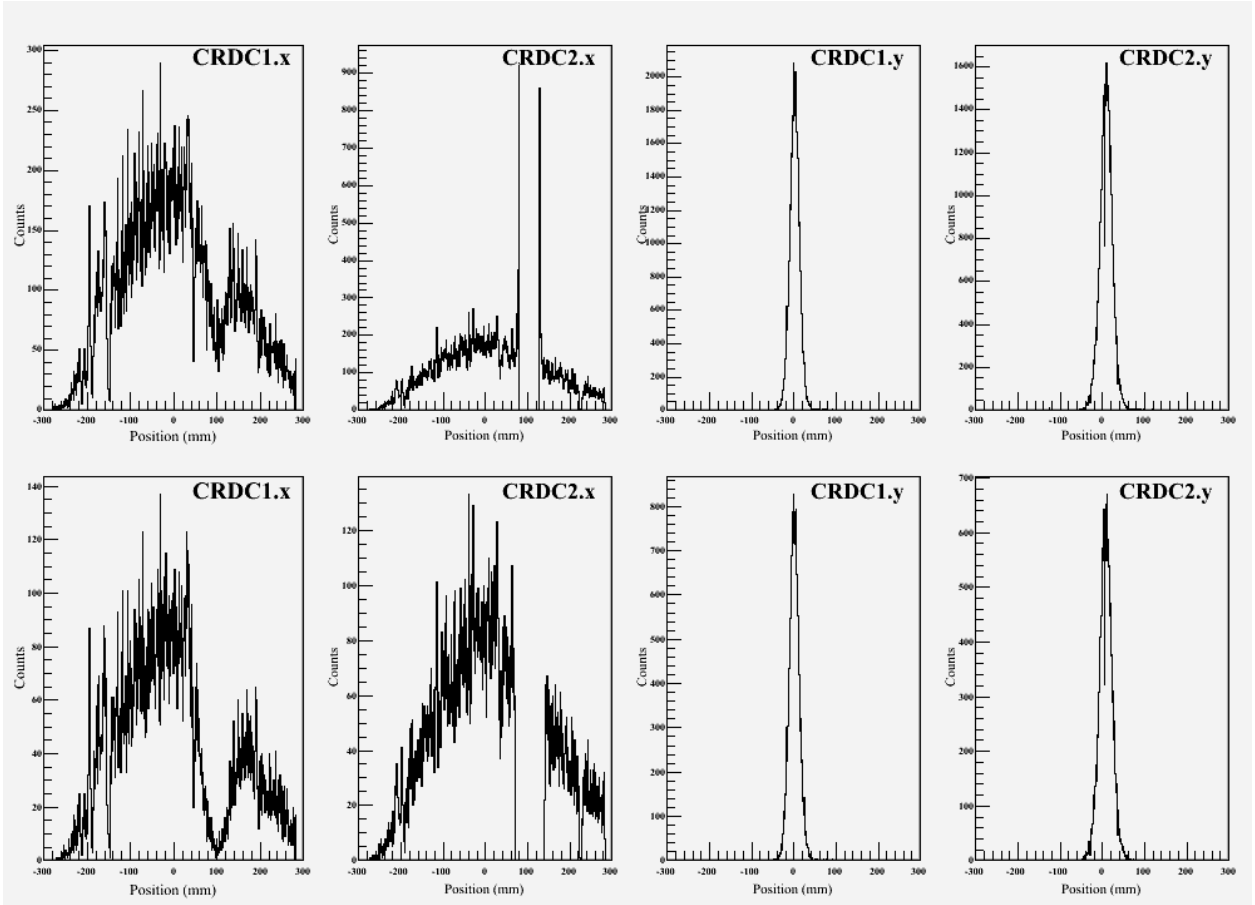


Figure 3.8: Histograms of the CRDC1 and CRDC2 x and y measurements from the  $^{25}\text{Si}$  residues. The top row is the values without the exclusion gate applied to the dead region of CRDC2 and also is not gated on the incident beam particle Time-of-Flight spectrum. The bottom row is the corresponding histogram to the top row for the same set of data except that the CRDC2 exclusion gate is applied and the events are also coincidence gated with the incident  $^{26}\text{Si}$  particles Time-of-Flight signatures. The inflation of events around the bad region of CRDC2.x can be seen in figures above. The difference in the scales of the histograms is due to the incident particle gating. The dip in the CRDC1.x histogram is due in part to the dead section of CRDC2 and possibly whatever event damaged the CRDC2 pad readout had a less severe but still noticeable effect on CRDC1's pad readout.

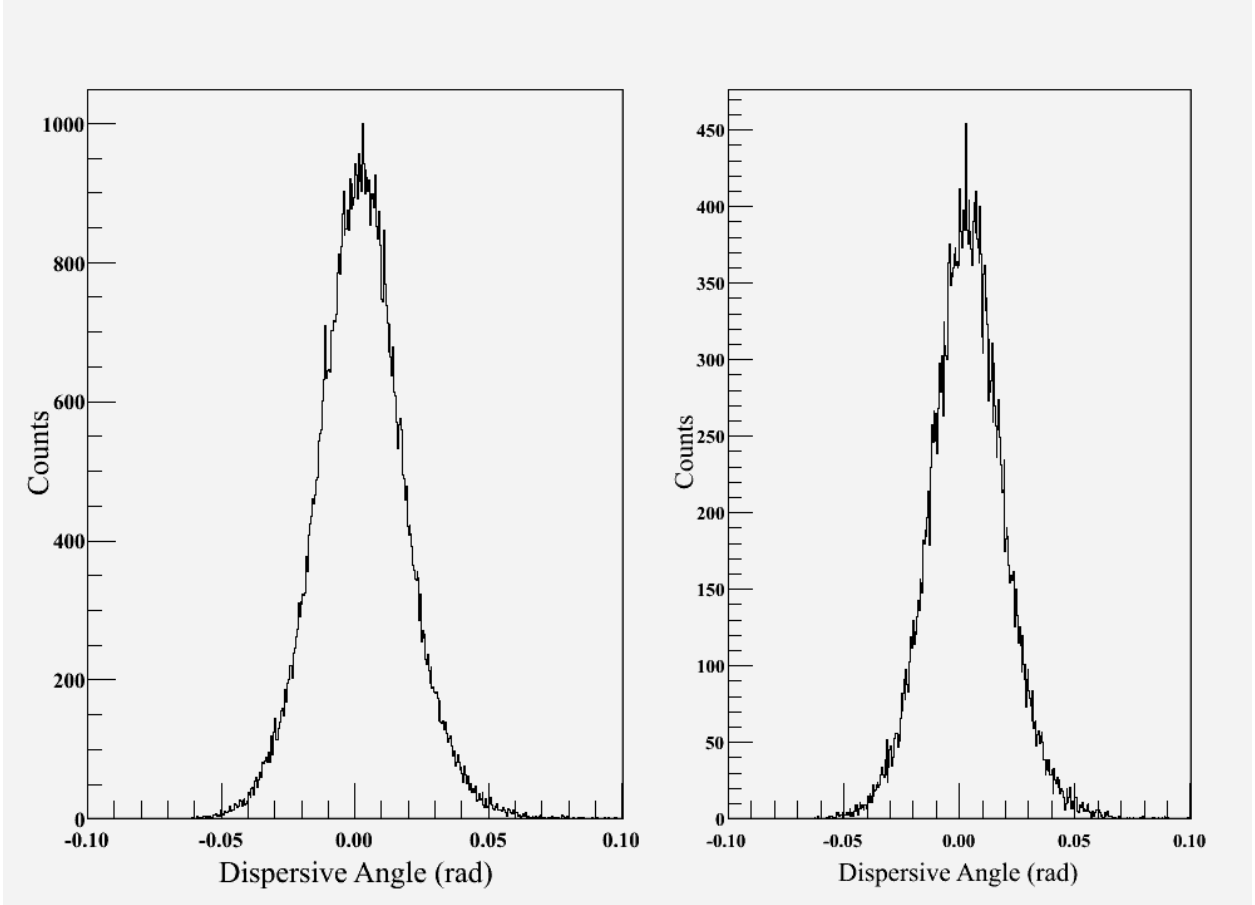


Figure 3.9: The above histograms are the dispersive angle trajectory measurements based on the same data sets used for Fig. 3.8. The histogram on the left corresponds to the top row in Fig. 3.8 and the one on the right corresponds to the bottom row in Fig. 3.8. It can be seen that the shape of the dispersion angle in the focal plane is not affected too adversely by the CRDC2.x exclusion gate.

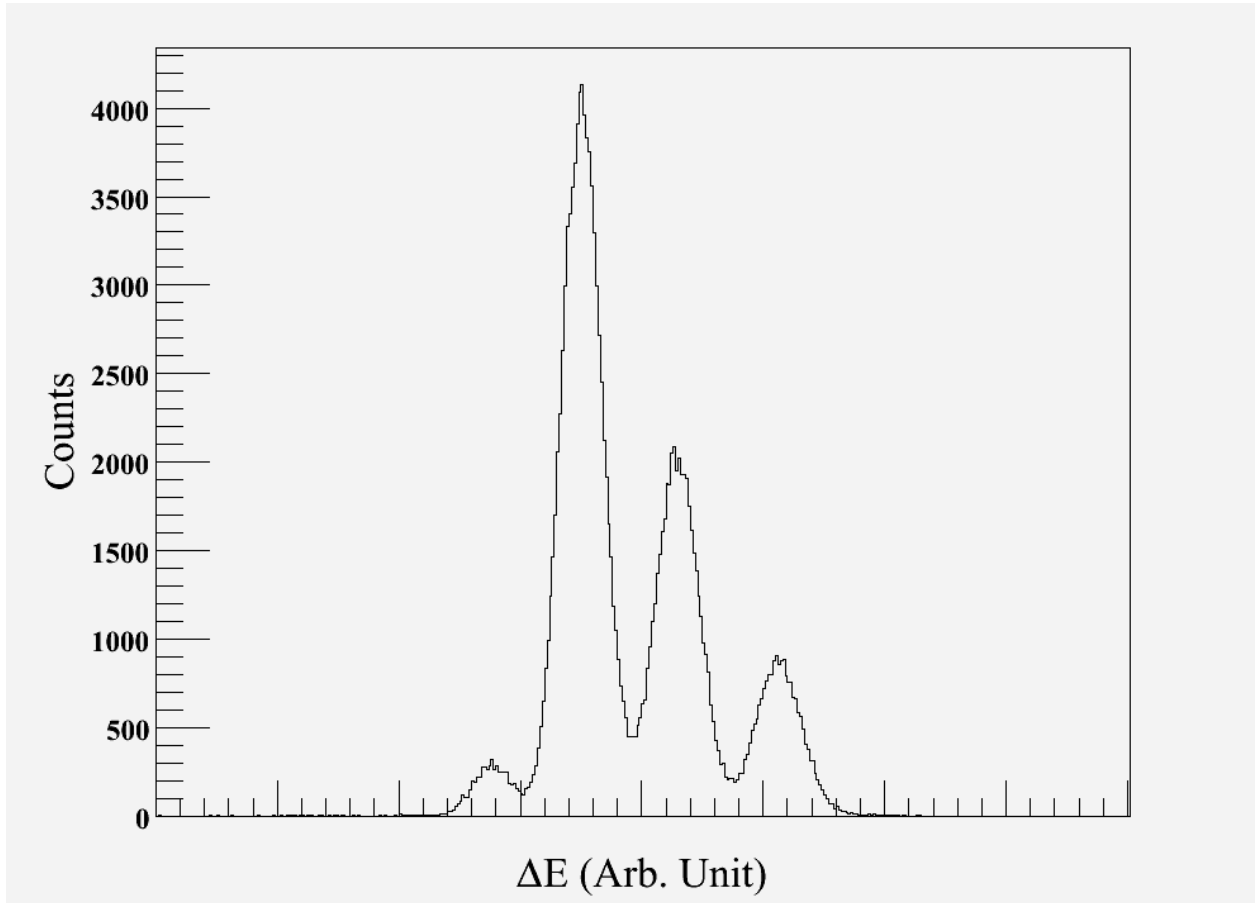


Figure 3.10: The spectrum of the Ion Chambers  $\Delta E$  for the  $^{26}\text{Si}$  secondary beam when the S800's spectrograph was set to focus the unreacted secondary beam into the focal plane. The S800 was tuned so the particles of interest had the highest charge state in the of all the isotopes that made it into the focal plane, so the Si isotopes are seen as the grouping of particles to the far right of the spectrum.

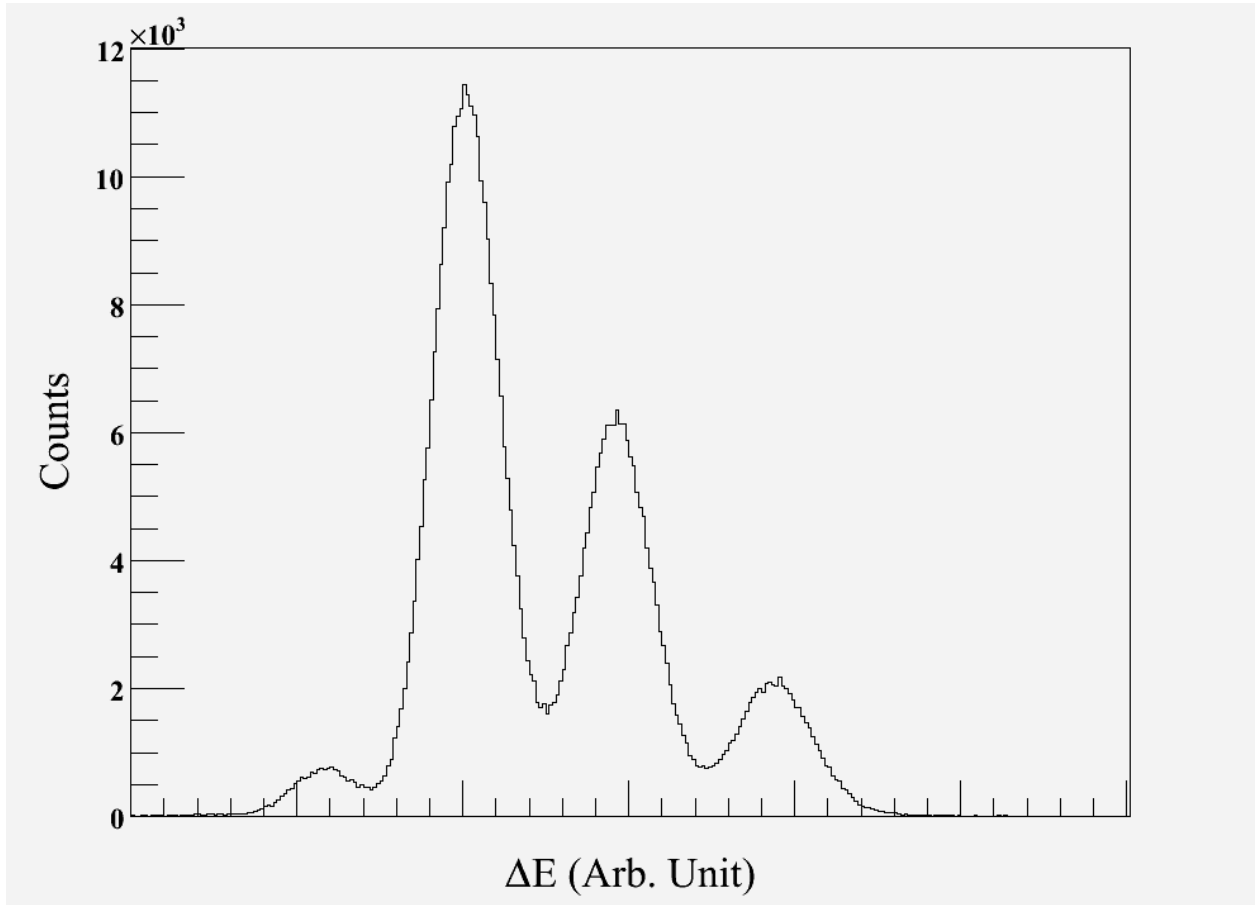


Figure 3.11: The spectrum of the Ion Chambers  $\Delta E$  for the  $^{30}\text{S}$  secondary beam when the S800's spectrograph was set to focus the unreacted secondary beam into the focal plane. The S800 was tuned so the particles of interest had the highest charge state in the of all the isotopes that made it into the focal plane, so the S isotopes are seen as the grouping of particles to the far right of the spectrum.

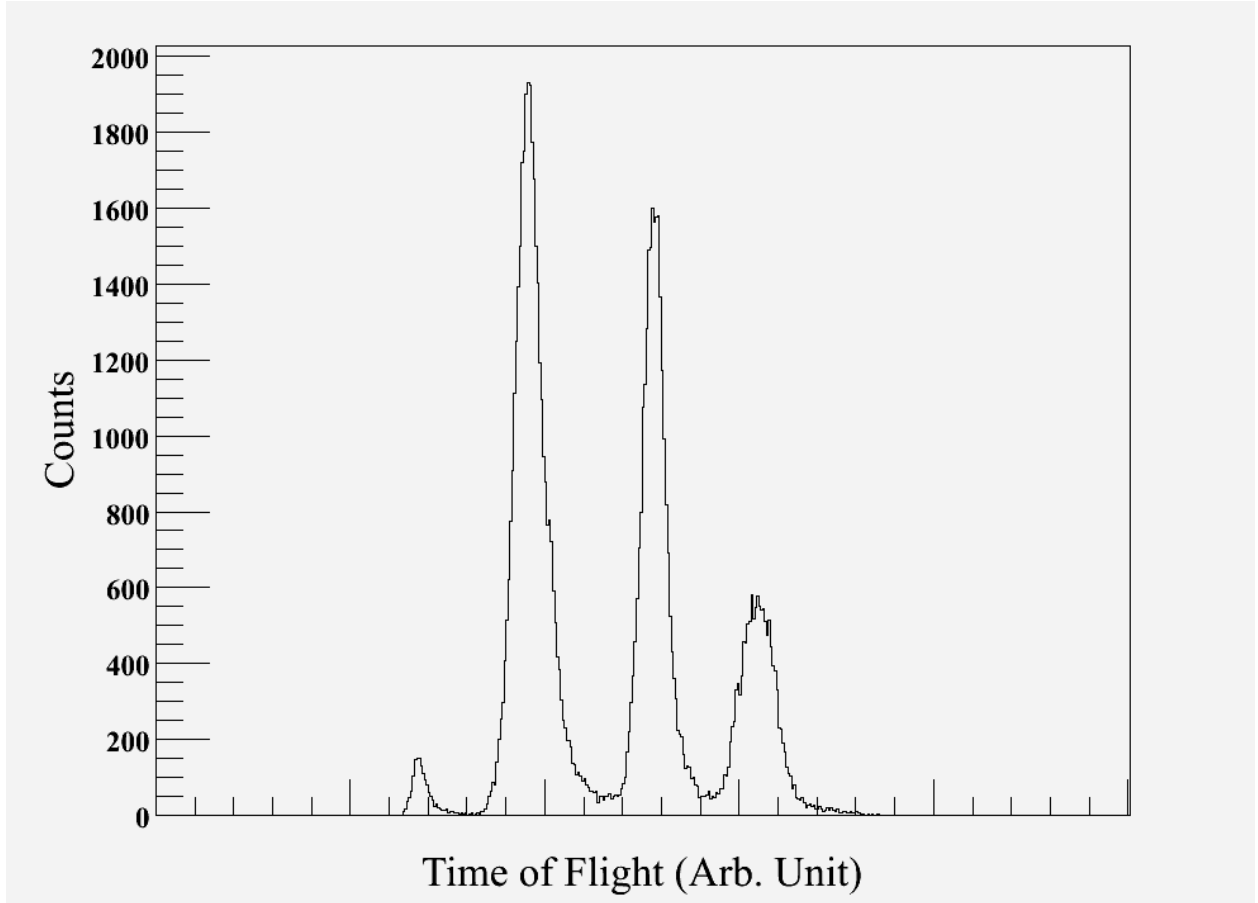


Figure 3.12: The time-of-flight between the extended focal plane (XFP) and the S800's object point (OBJ) scintillators for the  $^{26}\text{Si}$  secondary beam.  $^{26}\text{Si}$  is the grouping to the far right, while the other groupings are all heavier isotopes with longer times-of-flight.

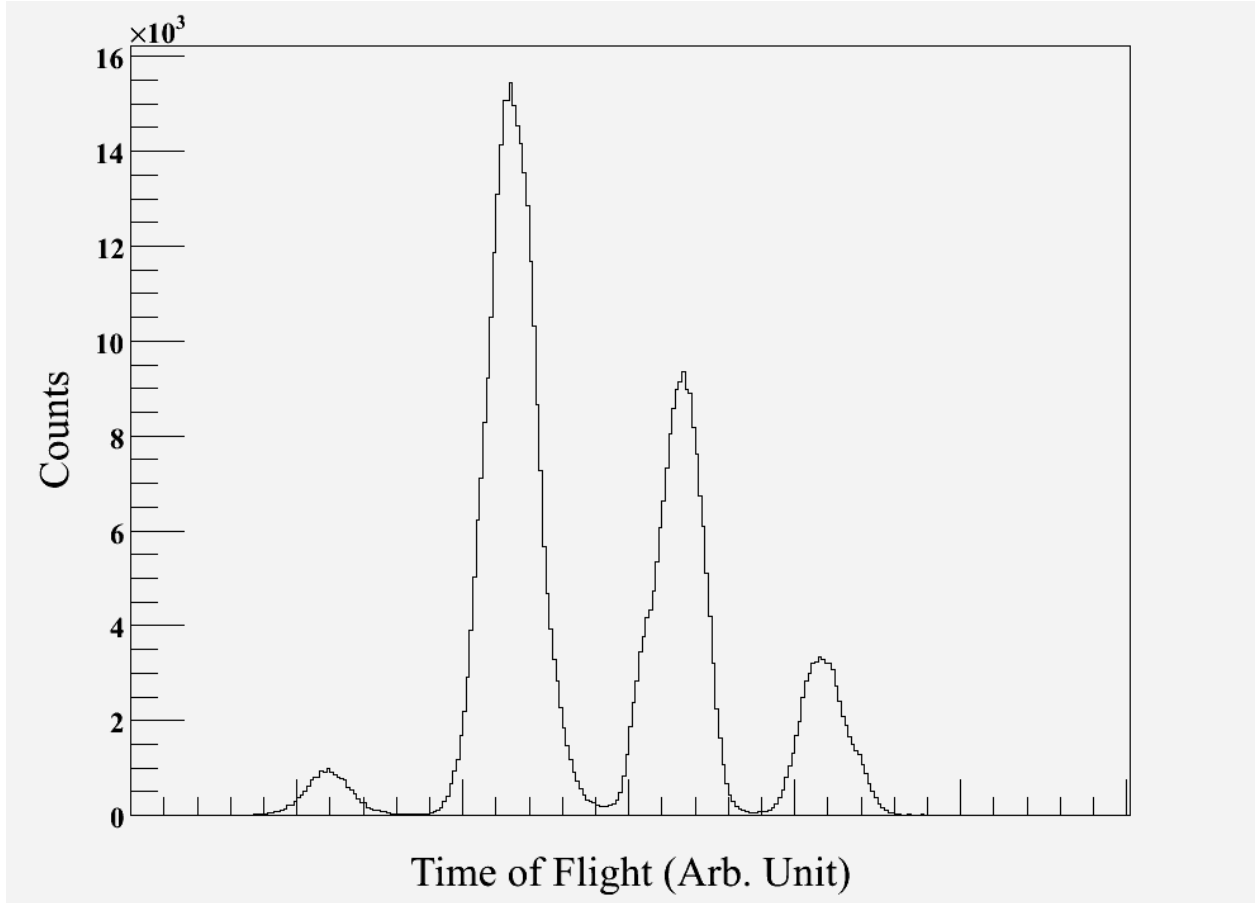


Figure 3.13: The time-of-flight between the extended focal plane (XFP) and the S800's object point (OBJ) scintillators for the  $^{30}\text{S}$  secondary beam.  $^{30}\text{S}$  is the grouping to the far right, while the other groupings are all heavier isotopes with longer times-of-flight.

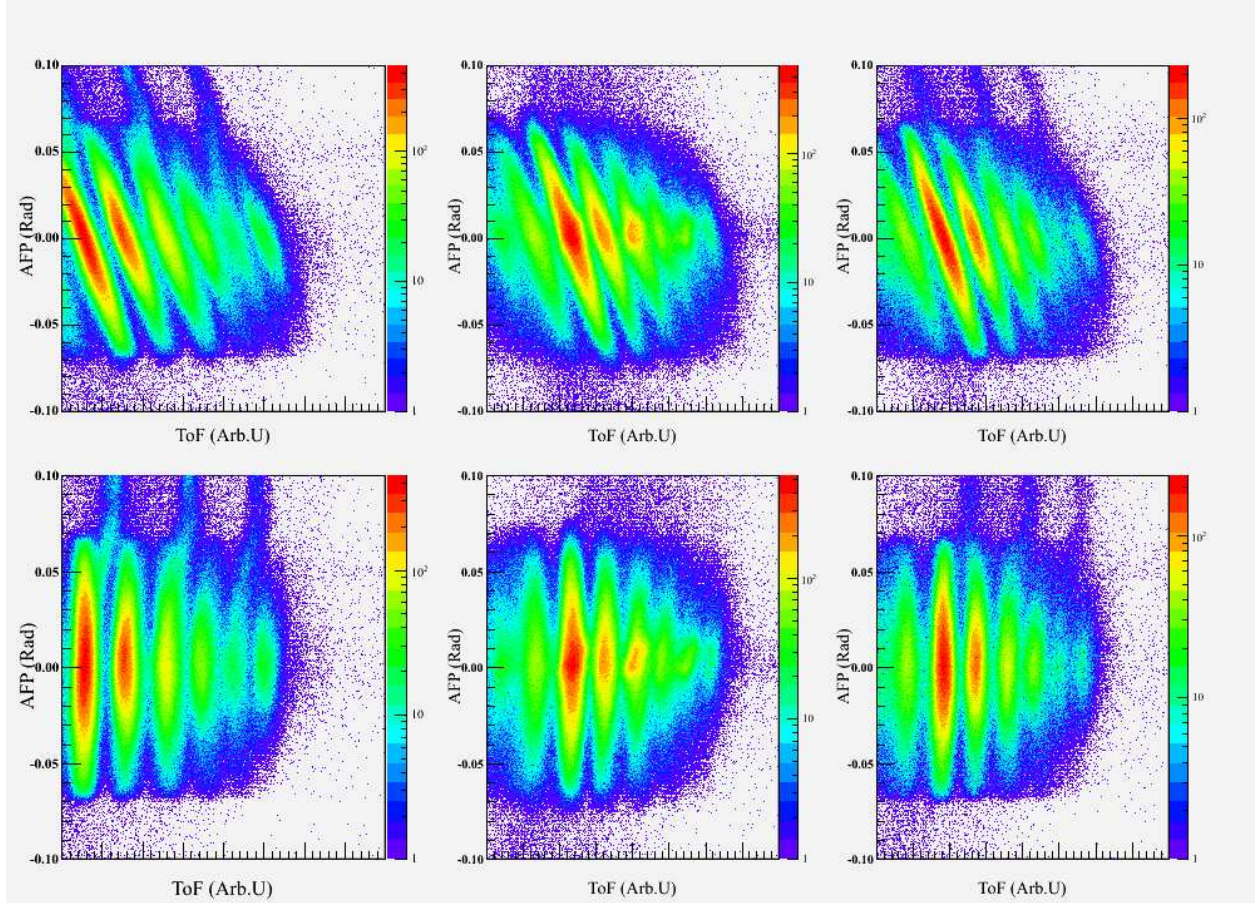


Figure 3.14: The effects of the angle in the focal plane corrections on the time-of-flight measurements are shown. For all six spectra the vertical axis is the measured angle in the focal plane (AFP), and the horizontal axis is the time-of-flight between the object scintillator and the focal plane scintillator. The top row are spectra without flight path correction terms for the residues from left to right:  $^{25}\text{Si}$ ,  $^{29}\text{S}$  first trial, and  $^{29}\text{S}$  second trial. The spectra on the bottom row are the same as the spectrum directly above it, except it includes a flight path correction term.

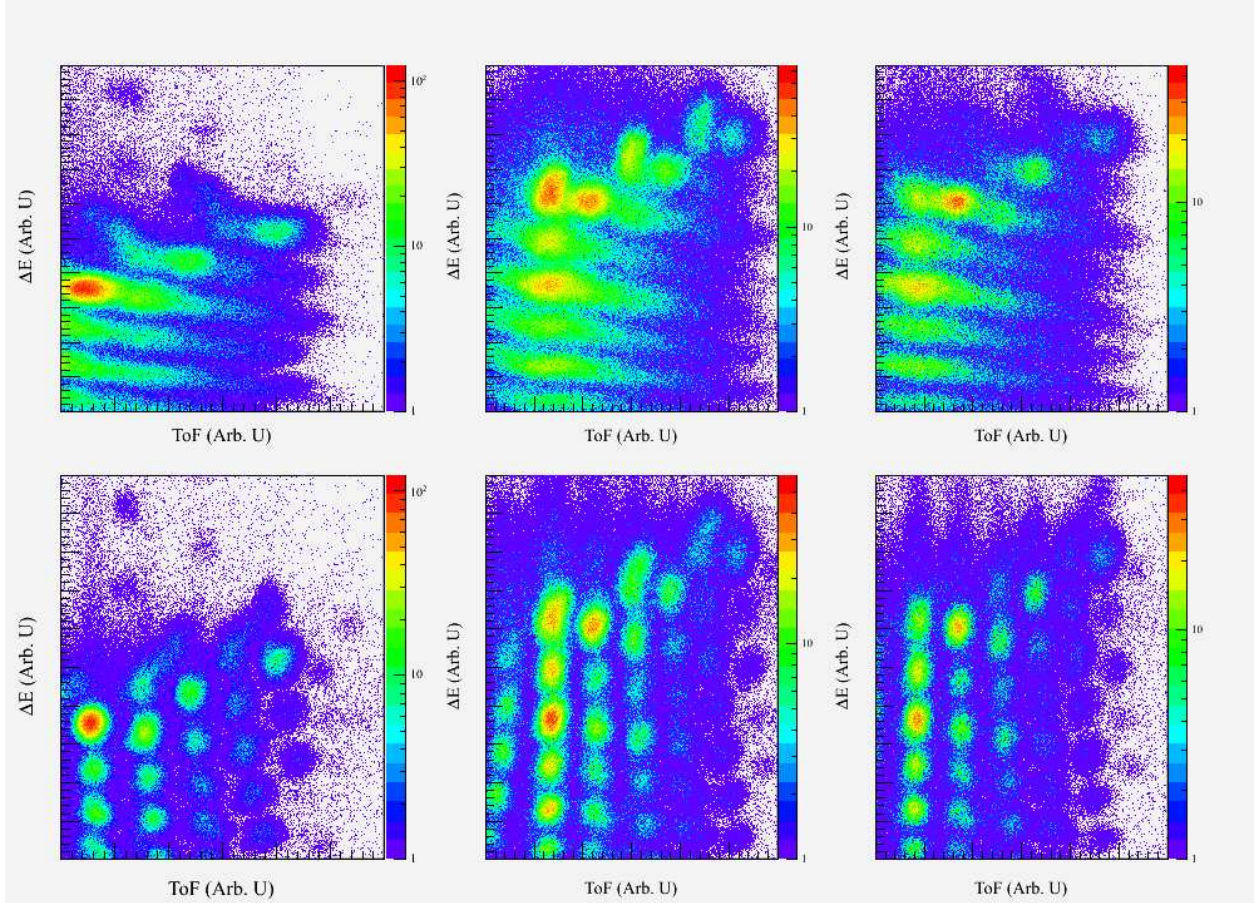


Figure 3.15: The effects of the angle in the focal plane corrections on the time-of-flight measurements for the residue particle identification spectra. For all six spectra the vertical axis is the energy loss in the ionization chamber, and the horizontal axis is the time-of-flight between the object scintillator and the focal plane scintillator. The top row are particle identification without flight path correction terms for the residues from left to right:  $^{25}\text{Si}$ ,  $^{29}\text{S}$  first trial, and  $^{29}\text{S}$  second trial. The spectra on the bottom row are the same as the spectrum directly above it, except it includes a flight path correction term.

### 3.3 The Segmented High Purity Germanium Detector Array (SeGA)

Currently there are two popular types of  $\gamma$ -ray detectors in wide use: scintillation detectors and High Purity Germanium (HPGe) detectors. NaI detectors have the benefit of being cheaper to produce, easier to maintain (no cryogenics needed), and can be formed into larger crystals for higher detection efficiency when compared to HPGe detectors, however the photopeak energy resolution of a NaI detector is often 10 times worse or more. For radiation energy detectors, the resolution is a measure of a detectors intrinsic ability to distinguish between two distinct energy peaks, which is a crucial feature for accurately determining nuclear structure from  $\gamma$ -ray spectroscopy. The typical shape of these photopeaks from a monoenergetic radiation source is close to that of a Gaussian distribution centered about the actual energy value. The resolution  $R$  for these cases is defined as the ratio of the full-width-at-half-maximum ( $FWHM$  or  $\Delta E$ ) of the Gaussian distribution divided by its centroid energy value  $E_c$  as

$$R = \frac{\Delta E}{E_c}. \quad (3.17)$$

The motivation for the Segmented HPGe Array (SeGA) was the need for a high resolution detection system to measure  $\gamma$ -rays emitted from relativistic sources.

A HPGe detector is a semiconductor detector consisting of a germanium crystal functioning effectively as a *pin* diode. A *pin* diode is a *pn* type semiconductor junction with a large insulating region between the *n* and *p* type semiconductor regions. The germanium crystal is lightly doped as either a *n* or *p* type semiconductor (depending on manufacturing) with a contact edge of the opposite charge carrier to create the junction. The sensitive/active volume of the detector is the large depletion region of the *pn*-junction as described in Ref. [37] and Ref. [40]. A reverse bias voltage is put across the *pn*-junction to create the depletion region, the larger the bias voltage the larger the depletion region and the faster the response time, however once the bias voltage becomes too high, some amount of leakage current begins to flow across the junction. The optimal voltage for each detector is determined by the manufacturer to maximize the detector's response and minimize the electrical noise from impurities and leakage current. The typical bias voltages for HPGe detectors are a few kilovolts and the functional  $\gamma$ -ray energy detection range is from a few keV to around 10 MeV. The high electron drift velocity inside the germanium crystal allows the electrons/holes

to be collected quickly and the signal output is a direct result of the moving charged particles in the detector's active region.

There are three different ways for an incident  $\gamma$ -ray to interact inside a detection medium: the photoelectric effect, Compton scattering, and pair production. In the photoelectric effect and Compton scattering, an electron is freed from an atom in the crystal lattice, creating an electron-hole pair in the depletion region. For the case of pair production, an electron-positron pair is created in the detector. One frustration of  $\gamma$ -ray detection is receiving only part of a  $\gamma$ -rays total energy. This occurs often from Compton scattering, in which the scattered photon is not recaptured in the detector, and in pair production when the positron is annihilated from interacting with another electron in the detector and the subsequent photons escape from the detector. The partial detection causes what is commonly referred to as a Compton edge effect in the  $\gamma$ -ray energy spectrum. This effect causes the energy peaks to deviate from the ideal Gaussian distribution shape into a Gaussian with a low energy trailing tail in which the shape of the tail is dependent on the  $\gamma$ -ray energy and the detector response function, the tail usually runs from the Compton edge all the way to the detector's low energy cutoff. In germanium detectors, the photoelectric effect is largely dominant at energies below a few hundred keV, however its strength becomes diminished with increasing photon energy. The Compton scattering plays a fairly consistent role in the bulk of the detector's functional energy range, its contributions also diminish with increasing photon energy, however they do not diminish as quickly as the photoelectric contributions, so the Compton scattering is the dominant interaction for a small energy region as the photoelectric contributions are diminishing and before pair production has picked up. Pair production plays no role in photon interaction until it reaches energies in excess of 1.022 MeV (twice the electron rest mass), at which point its contribution rises quickly and plays a dominant role for energies close to 10 MeV and above.

### 3.3.1 Doppler Effects

In the case of  $\gamma$ -rays being emitted from a source moving at with a relativistic velocity, the resolution is further complicated by the Doppler energy shift. For the purposes of nuclear structure studies, the  $\gamma$ -ray energy must be reconstructed into the emitting particles rest frame. For a  $\gamma$ -ray detected in the lab frame with energy  $E_{\text{lab}}$ , emitted from a particle moving with velocity  $\beta c$ , and detected at an angle  $\theta$  from the direction of the particles

velocity from the point of emission, the emitted  $\gamma$ -ray energy in the particles rest frame is given by

$$E_\gamma = E_{\text{lab}}\gamma(1 - \beta \cos \theta). \quad (3.18)$$

Following Ref. [41], the emission frame Doppler corrected energy resolution for the  $\gamma$ -ray ( $R_\gamma$ ) is given by

$$R_\gamma^2 = \left( \frac{\beta \sin \theta}{1 - \beta \cos \theta} \right)^2 \Delta_\theta^2 + \left( \frac{\beta - \cos \theta}{(1 - \beta^2)(1 - \beta \cos \theta)} \right)^2 \Delta_\beta^2 + R_{\text{lab}}^2, \quad (3.19)$$

where  $\Delta_\theta$  is the uncertainty in  $\theta$ ,  $\Delta_\beta$  is the uncertainty in  $\beta$ , and  $R_{\text{lab}}$  is the intrinsic resolution of the detected photon in the lab frame from Eq. 3.17 measured from a stationary source. It can be seen in Eq. 3.19, that there are more factors than just the intrinsic detector resolution that must be taken into account, which is where the design of SeGA comes into play.

SeGA consist of 18 individual high purity germanium (HPGe) detectors. The unique feature of each detector is the electronic segmentation of the main crystal element into 32 segments that can be read out individually along with a total crystal central contact signal, as seen in Fig. 3.16. Each detector uses a cylindrically-symmetric  $n$ -type germanium crystal with a coaxial central contact that runs the almost the length of the crystal, with an external diameter of 70 mm and a length of 80 mm as seen in Fig. 3.16 and Ref. [41]. The detector crystal is electronically divided lengthwise into eight 10 mm disks, and each disk is quartered radially to create the 32 segments. This segmentation does cause a small dead layer between the segments, but it is a necessary sacrifice.

As shown in Eq. 3.19, the level of accuracy for determining  $\beta$  and  $\theta$  plays a large role in the array's energy resolution, and it becomes even more pronounced at higher velocities and for more forward detection angles (smaller  $\theta$ ). The SeGA detectors are positioned with their axis of symmetry perpendicular to the target to utilize the lateral segmentation to determine the emission angle of the photon in the lab frame. The detectors are arranged into two angle groups with respect to the beam direction, one ring of ten detectors centered about  $90^\circ$  where the Doppler shift is minimized and another ring of 7 detectors centered around  $37^\circ$  from the beam forward direction as shown in Figs. 3.17 and 3.18. The closest cylindrical edge of each detector is positioned roughly 20 cm from the center of the target.

The  $\gamma$ -ray emissions of interest are typically coming from the de-excitation of extremely short lived states in the newly formed reaction residues, so for these experiments it is accurate

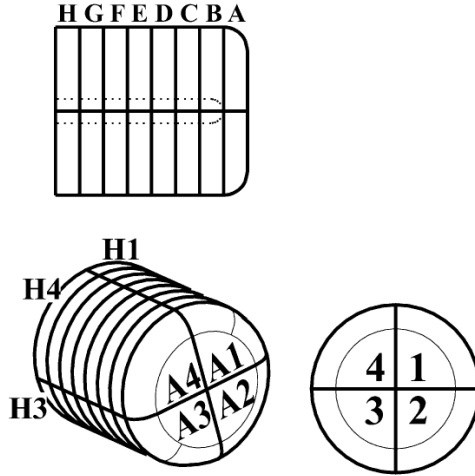


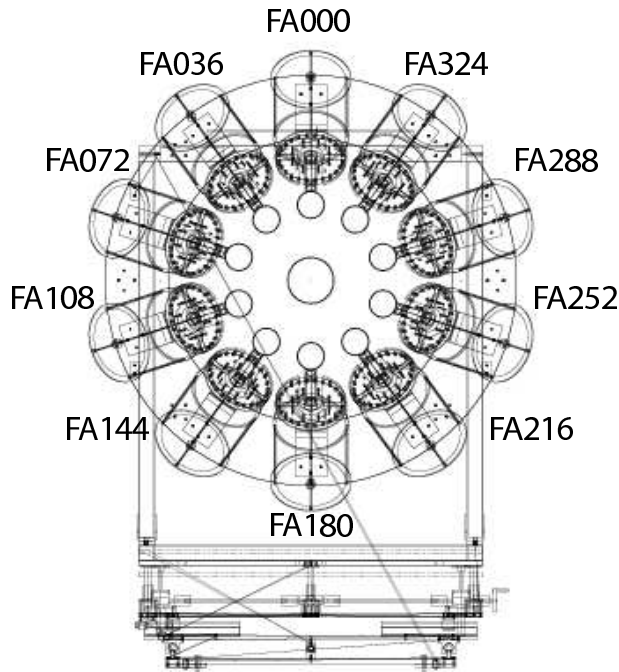
Figure 3.16: Schematics of a single HPGe crystal's segmentation from three different perspectives, clockwise from top: viewed perpendicular to the crystals lateral axis; view facing the detectors circular face; and a view from a slight angle just off face. The three diagrams display the labeling scheme of the detector segments. The crystal is divided into 8 disk segments along its lateral axis, and each disk segment is quartered radially to make a total of 32 segments. Each segment has an individual isolated signal output and the entire crystal can be read from the central contact that runs the almost the length of the crystal. The outline of the central contact is shown by the dotted line in the upper figure. Each of the 17 detectors used in SeGA contain a single 32-fold segmented germanium crystal. Figure from Ref. [41].

enough to assume that the observed  $\gamma$ -rays are emitted from the same point in the target where the reaction takes place. With the current SeGA-S800 set-up, it is not possible to determine the exact location of the reaction inside the target, but it is approximated as occurring in the center of the target. Using the orientation of each detector, a segment location map is created with the  $x, y$ , and  $z$ , Cartesian spatial coordinates of the center of each segment. Using this segment map, the angle  $\theta$  from the target's center can be determined as

$$\theta = \arccos \left( \frac{z}{(x^2 + y^2 + z^2)^{1/2}} \right). \quad (3.20)$$

Using the set-up as described, the uncertainty in  $\theta$  is  $\delta\theta \approx 2^\circ$ . A single photon interaction in one of the SeGA detectors can cause one or multiple segments to fire in the same detector. In the trivial case of one segment firing, the triggered segments location map coordinates are used to calculate the angle  $\theta$  used for the Doppler energy shift reconstruction for the in

90 degree detectors  
(toward the cyclotrons)



37 degree detectors  
(toward the S800)

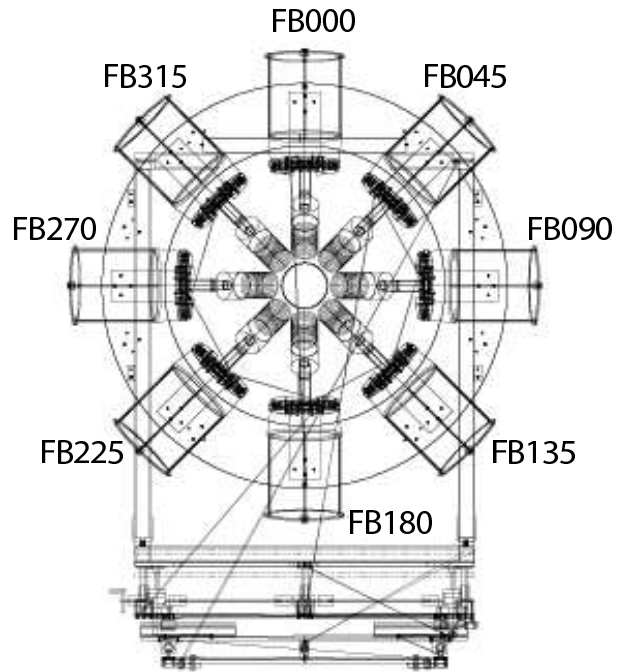


Figure 3.17: A schematic of SeGA's two rings of segmented HPGe detectors. The left hand figure is the 90° ring from a view facing up stream with respect to the beam from the S800's entrance. The right hand figure is the 37° ring viewed down stream from target towards the S800's entrance. The detector labels are also displayed. The detector labeled FB180 is absent from the actual configuration used due to interference with a valve on the S800.

Eq. 3.18, and the energy is taken from the detectors central contact. For the cases where more then one segment in the same detector are triggered for a single photon event, the segment with the most energy deposited in it is considered the point of first contact and its position is used to determine  $\theta$ .

The projectile nuclei and the projectile-like reaction residues are losing energy and slowing down while they pass through the 376 mg/cm<sup>2</sup> thick <sup>9</sup>Be target in the same manner as the wedge discussed in Sec. 3.1.2. This causes the velocity  $\beta$  in Eq. 3.18 to be dependent on how far into the target the reaction occurs. As previously stated, this reaction point can not be determined at present but the best assumption is that on average it is very close to the center

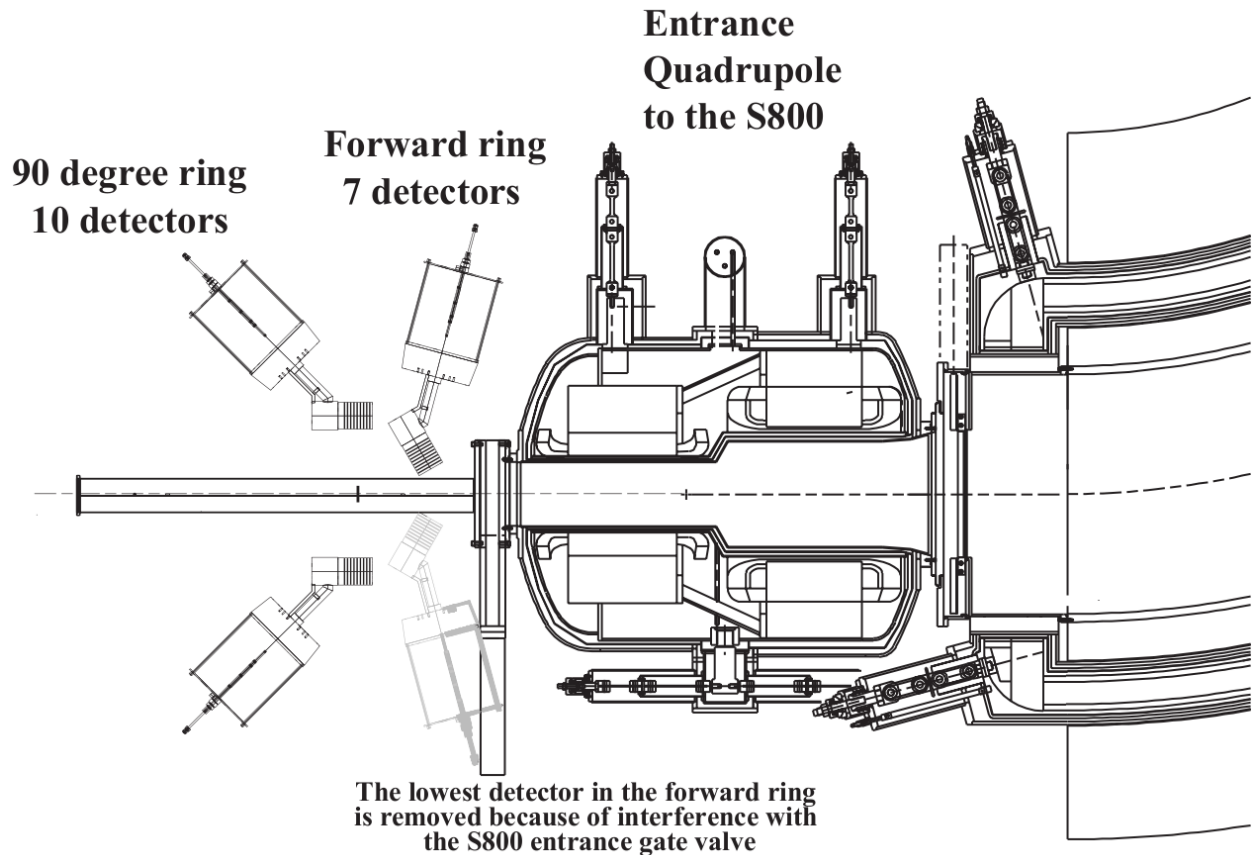


Figure 3.18: A schematic of SeGA as configured around the target position at the beam entrance to the S800. The beam direction is from the left to the right of the page.

of the target. As a first approximation, the *Physical Parameter Calculator* application of the software program *LISE++* [42, 43] was used to determine the mid-target velocity. The application uses the relativistic energy losses based on the calculations from the program *ATIMA* [44, 33]. As a first guess, the velocity is averaged between two calculations. One is for the energy loss of the projectile after traveling through the first half of the target with an initial velocity determined from Eq. 3.7 using the pre-target  $B\rho$  value. The other is for the reverse energy loss of the projectile-like reaction residue traveling through the second half of the target with the final velocity determined using the post-target  $B\rho$  value of the S800's spectrograph. After applying Eq. 3.18 to the  $\gamma$ -rays detected in coincidence with the reactions of interest, the  $\beta$  value can be adjusted by comparing the Doppler corrected photopeak energy spectra of the  $37^\circ$  detector ring to the  $90^\circ$  ring. Because of the different  $\theta$

values for the two detector rings, the energy correction in Eq. 3.18 for the two rings will only match-up for the correct value of  $\beta$  as can be seen in Fig. 3.19. This  $\beta$  value also corresponds to the optimal photopeak resolution of the total SeGA energy spectrum.

Several months after the completion of the experiment it was determined by a member of the NSCL staff that due to a measurement error of one of the beamline components the target position was shifted 2.6 cm upstream from its proper location at the center of SeGA, and a new segment location map file was created. This shifting of the target location affects the value of  $z$  in Eq. 3.20. In order to determine the correct value for the target position, a  $\gamma$ -ray with a known energy that was being emitted from a relativistic source was needed. To serve this purpose, the established 1795.9(2) keV  $\gamma$ -ray from the first excited state of  $^{26}\text{Si}$  from Ref. [45] was used as a relativistic  $\gamma$ -ray source for target position calibration. The life-time of this state is 430(40) fs, which is fast enough to assume it occurs at the same point in the target that the reaction occurs (approximated as the middle of the target). The population of this state is more than likely from relativistic Coulomb excitation of the primary beam, but the mechanism of creation is not of relevant. A particle identification coincidence gate was placed on the  $^{26}\text{Si}$  particle contaminates in the  $^{26}\text{Si}\rightarrow^{25}\text{Si}$  reaction data runs and  $\gamma$ -rays in coincidence with the  $^{26}\text{Si}$  reaction residues were observed. By adjusting the values of  $\beta$  and  $z$  used in Eqs. 3.18 and 3.20, the Doppler corrected energy photopeak for the  $37^\circ$  and  $90^\circ$  detector rings will both be at 1796 keV for the correct values of both  $z$  and  $\beta$  as shown in Fig. 3.19. After adjusting for the optimal total SeGA energy resolution of the 1796 keV  $^{26}\text{Si}$  photon, it was determined that the target position needed to further be adjusted back downstream by 1 cm. The targets position in the plane perpendicular to the beam axis was also checked by comparing the 1796 keV photopeak between individual detectors in the same ring. There was no noticeable shift in the photopeaks when compared between the detectors, implying that the target was centered in this plane.

### 3.3.2 Energy Calibration

The energy calibrations for each of the SeGA detectors play a crucial role in the accuracy of the  $\gamma$ -ray spectroscopy. The central contact output signal of each detector was adequately gain matched at the analog signal amplifier output before it was digitized, and then the energy spectrum is further calibrated in the analysis software. The central contact energy calibrations were performed for each individual detector using stationary  $^{152}\text{Eu}$  and  $^{56}\text{Co}$

sources with well known  $\gamma$ -ray decays as shown in Table 3.1. Calibration data runs with

Table 3.1: The photopeak energies and intensities used for the energy and efficiency calibrations. The  $^{152}\text{Eu}$  source (left two columns) has a known activity of  $1.131 \times 10^5 \pm 1.4\%$  decays per second measured on May 1, 1978, and a half-life of 13.537(6) years. The  $^{56}\text{Co}$  source (right two columns) has an unknown activity. The intensity is given as a percent chance of the emission of that  $\gamma$ -ray per decay. The activity of the  $^{152}\text{Eu}$  source is from the *National Bureau of Standards Certificate SRM 4218-C-25* that was associated with that particular source, all other data is from Ref. [46].

$^{152}\text{Eu}$		$^{56}\text{Co}$	
Energy (keV)	Intensity (%)	Energy (keV)	Intensity (%)
121.7817 (3)	28.67 (15)	846.771 (40)	99.94 (3)
244.6975 (8)	7.61 (4)	1037.84 (6)	14.17 (13)
344.2785 (12)	26.6 (5)	1238.282 (7)	66.9 (6)
411.1163 (11)	2.237 (25)	1360.215 (12)	4.29 (4)
443.965 (3)	3.16 (23)	1771.351 (16)	15.47 (14)
778.904 (18)	12.96 (14)	2015.181 (16)	3.04 (5)
867.373 (3)	4.26 (3)	2034.755 (13)	7.89 (13)
964.0727 (213)	14.785 (7)	2598.459 (13)	17.3 (3)
1112.069 (3)	13.69 (7)	3201.962 (16)	3.32 (7)
1212.948 (11)	1.426 (9)	3253.416 (15)	8.12 (17)
1299.14 (9)	1.625 (19)	3272.99 (15)	1.93 (4)
1408.006 (3)	21.07 (10)		

both sources were performed at the beginning of the experiment before reaction data was collected and again at the end of the experiment after the reaction data had been collected as listed in Table 3.2. The central contact energy spectra were fitted using the computer program *RadWare* [47], which contains a subprogram called *gf3*. The *gf3* program is specially designed to perform fitting routines on  $\gamma$ -ray energy photopeaks. The fit function is composed of four component functions, two to fit the actual photopeak and two to fit the background. The background is fit locally to a quadratic polynomial added to a smoothed step function to account for the Compton scattering. The photopeak function is fit to a Gaussian function plus a skewed Gaussian and then added to the background for the best fit. The main concern of the energy calibration was the photopeak centroid. For each detector, the raw central contact energy was adjusted by a quadratic polynomial to align and scale the raw central contact energies to the correct calibration energy. A comparison of the uncalibrated to calibrated energy spectra is shown in Fig. 3.20 and the total calibrated energy spectra for

Table 3.2: All of the runs were performed in 2004. The first four runs on 11/23 were taken before any reaction data was taken and the last two runs were taken at the end of the experiment after the reaction data was taken. There were only two physical radiation sources.

Date	Source	Run Time (s)
11/23	$^{152}\text{Eu}$	3305
11/23	$^{152}\text{Eu}$	3888
11/23	$^{56}\text{Co}$	3434
11/23	$^{56}\text{Co}$	3731
11/29	$^{152}\text{Eu}$	3687
11/29	$^{56}\text{Co}$	7345

both sources is shown in Fig. 3.21. The lab frame calibrated photopeak energy resolutions for the entire SeGA array are shown in Table 3.3.

The energy calibrations of the individual segments for each detector must also be made. As discussed in Sec. 3.3.1, the segments play an important role in determining the value of  $\theta$  used in Eq. 3.18. While the energy output of each segment is not as sensitive or critical as that of the detector's central contact, having a proper segment energy calibration improves the our Doppler corrected energy resolution by minimizing uncertainties in  $\theta$  as shown in Eq. 3.19. Once the central contact energy has been calibrated, the segment calibrations become somewhat trivial. By focusing on events where only one segment fired, that segments energy can be calibrated to the energy recorded by the central contact. This procedure was done for all of the source runs listed in Table 3.2, and using the full statistics available for each segments energy correlation to its central contact energy, each segment was calibrated to a quadratic polynomial. The calibrated central contact energy versus the summed calibrated segment energy per event for each detector is shown in Fig. 3.22, which shows a good one-to-one correspondence between the summed segment energies and the central contact energies for each detector.

### 3.3.3 Detection Efficiency

The  $\gamma$ -rays detected in coincidence with a particular reaction residue are used as a tag for determining the reaction cross section to a particular excited state of that residue. To perform this task effectively, it is important to determine the absolute  $\gamma$ -ray detection

Table 3.3: Measured energy resolutions of SeGA using *RadWare's* [47] fitting routines. The resolutions are taken from a weighted average over all the source runs listed in Table 3.2. The Resolution values are calculated as the ratio of the peaks *FWHM* determined from the Gaussian width to the energy of the photopeaks centroid.

<sup>152</sup> Eu		<sup>56</sup> Co	
Energy (keV)	Resolution	Energy (keV)	Resolution
121.8	0.0539	846.8	0.0082
244.7	0.0272	1037.8	0.0067
344.3	0.0193	1238.3	0.0060
411.1	0.0166	1360.2	0.0059
444.0	0.0156	1771.4	0.0045
778.9	0.0093	2015.2	0.0042
867.4	0.0083	2034.8	0.0040
964.1	0.0078	2598.5	0.0035
1112.1	0.0067	3202.0	0.0032
1212.9	0.0064	3253.4	0.0031
1299.1	0.0061	3273.0	0.0030
1408.0	0.0058		

efficiency of SeGA as a whole. The photon detection efficiency of a HPGe detector is dependent on the photon energy and the intrinsic properties of the detector. The problem with performing efficiency corrections on a Doppler corrected  $\gamma$ -ray emission is the fact that  $\gamma$ -rays that have the same energy in the emission frame, can have very different lab frame energies depending on the emission angle, which means that the efficiency corrections have to take this into account. This problem is overcome by using the detection simulation program GEANT3 [48]. GEANT uses the known information about the SeGA detector geometry and composition and the target position, combined with realistic  $\gamma$ -ray energy response functions, and deviations of the emitting particles velocity and position due to beam spread. Taking this information into account, GEANT uses a Monte-Carlo style approach to simulate the probability of a  $\gamma$ -ray being emitted and detected in SeGA. Any polarization effects that would cause the  $\gamma$ -rays to not be emitted uniformly in all directions from the reaction residues are neglected. Because the efficiency corrections for the particle- $\gamma$  coincidence events is based solely from the simulation results, it is important to verify the accuracy of the simulations to a measurable quantity. After configuring the simulations for the experimental conditions, efficiency simulations were run for a stationary source at

the target position emitting photons in all directions over a continuous and random energy spectrum from 0 keV to 4000 keV in 1 keV increments for  $5 \times 10^{11}$  events. The simulated emission spectrum is shown in Fig. 3.23 and the corresponding GEANT simulated total SeGA photon detection efficiency is shown in Fig. 3.24.

Of the two  $\gamma$ -ray calibration sources used, only the  $^{152}\text{Eu}$  source had a known and calibrated decay activity. However the  $^{152}\text{Eu}$  source's highest photon energy is below 1.5 MeV as shown in Fig. 3.21 and Table 3.1, which is not as high as some of the lab frame  $\gamma$ -ray energies that will be observed in the experiment. Rather than try to extrapolate the efficiencies from the  $^{152}\text{Eu}$  source, the  $^{56}\text{Co}$  source was used to determine the efficiency at higher energies, although the  $^{56}\text{Co}$  source does not have any calibrated decay activity data. The total detection efficiency for the SeGA array was determined by fitting the detected photopeaks for each source run in Table 3.2, using *RadWare* as described in the previous section, and using the number of background subtracted counts in the fitted photopeak as the total number of detected photo-events for each peak. The efficiency was then calculated for each energy peak by taking the ratio of the number of detected photo-events in the peak to the total number of  $\gamma$ -ray emissions that should have occurred based on the calibrated activity life-time adjusted for the amount of time elapsed since the calibration was made times the  $\gamma$ -ray branch intensity given in Table 3.1. The total SeGA efficiency results of all three  $^{152}\text{Eu}$  calibration runs are shown in Fig. 3.25.

Since the  $^{56}\text{Co}$  source does not have any standardized activity data, only the relative photopeak efficiencies could be determined on a first pass using the decay branching ratios from Table 3.1. The shape of the  $\gamma$ -ray efficiency curve can be approximated over a limited energy range to a polynomial function of the energy. Using the overlapping energy ranges at the upper end of  $^{152}\text{Eu}$  and the lower energy range of  $^{56}\text{Co}$  it was possible to normalize the relative efficiencies of  $^{56}\text{Co}$  to the total absolute efficiencies. The efficiency as a function of energy was fit to a 2nd degree polynomial over the energy range covering the six highest energy  $\gamma$ -rays of  $^{152}\text{Eu}$  in Table 3.1. After fixing the parameters of the fitted polynomial, the whole function is multiplied by a scale factor, and the scale factor is adjusted by a  $\chi^2$  minimization routine to give the best agreement of the fixed polynomial to the four lowest energies of the  $^{56}\text{Co}$  source in Table 3.1. This scale factor is then used to renormalize the measured  $^{56}\text{Co}$  relative efficiencies to the absolute efficiencies. This process provides absolute efficiency measurements of SeGA over the range of relevant  $\gamma$ -ray energies shown in Fig. 3.26.

In order to validate the  $\gamma$ -ray detection efficiencies of the GEANT simulation, it is necessary to compare the actual measured efficiencies in Fig. 3.26 to the simulated efficiencies in Fig. 3.24. Taking the ratio of the measured efficiency to the simulated efficiency at the same energy over the energy ranges relevant to this experiment is shown in Fig. 3.27. The ratio should ideally be unity, but the weighted average of the points is 1.063 with a weighted deviation of  $\pm 0.024$ . This scale factor of 1.063(24) is applied to all the GEANT simulated photopeaks used in the experiments and after applying the scale factor to the simulated efficiencies, Fig. 3.27 transforms into Fig. 3.28. The simulated to measured efficiencies were also compared for the  $37^\circ$  and  $90^\circ$  detector rings separately, and apart from the lower statistics there was no noticeable difference.

The GEANT simulations for a stationary source are in good agreement with what is observed, so the simulations can be used to reliably determine the total detection efficiencies for a  $\gamma$ -ray being emitted from a moving source. All of the Doppler reconstructed  $\gamma$ -ray simulations are done for the emission of  $10^7$  monoenergetic  $\gamma$ -ray events being emitted randomly in all directions in the emission frame from a source moving with the same velocity used for the Doppler energy reconstruction in Eq. 3.18.

### 3.3.4 Timing Signal

The central contact output signal was also used for a timing signal. Looking at the timing difference between the SeGA detectors timing signal and the event triggering signal as shown in Fig. 3.29. By placing a software coincidence logic gate around the main peaks seen in the each detectors timing spectrum in Fig. 3.29, a large amount of the low energy background noise is cut out of the Doppler reconstructed  $\gamma$ -ray spectra. It can be seen in Fig. 3.30 that the only consequence of applying these timing gates is a large reduction in the low energy background noise in the  $\gamma$ -ray energy spectra.

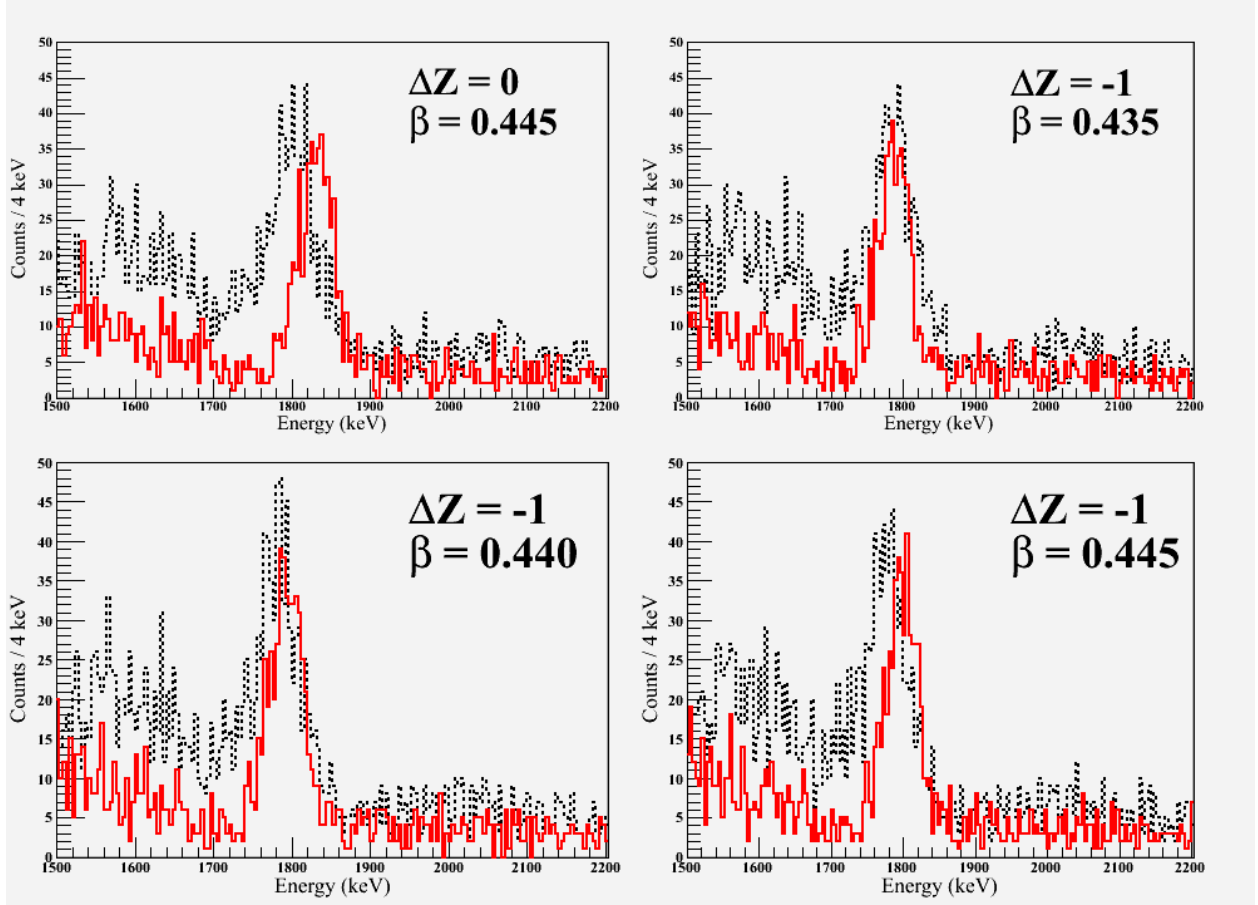


Figure 3.19: The Doppler corrected  $\gamma$ -ray energy spectra detected for the SeGA  $37^\circ$  ring (dashed black line) and the  $90^\circ$  ring (solid red line) in coincidence with  $^{26}\text{Si}$  in the S800's focal plane with different  $\beta$  velocity values and different target offset  $\Delta Z$  values. All four spectra are focused on the  $1795.9(2)$  keV  $\gamma$ -ray produced from the de-excitation of the first excited state of  $^{26}\text{Si}$ . The segment angle file used for these calculations already accounted for a 2.6 cm upstream shift of the target which corresponds to the top left figure with  $\Delta Z = 0$ . A negative value of  $\Delta Z$  corresponds to shifting the target downstream in units of centimeters. It can be seen in the three spectra for  $\Delta Z = -1$ , that the  $90^\circ$  ring is less effected by changes to  $\beta$  then the  $37^\circ$  ring. It is obvious from looking at the  $90^\circ$  detector ring for  $\Delta Z = 0$  that the energy of the corrected peak will be above 1800 keV. The bottom left figure shows the best agreement of the  $37^\circ$  and  $90^\circ$  rings with the expected  $\gamma$ -ray energy, so the target position corresponding to  $\Delta Z = -1$  was used for all other measurements. The two figures to the right show the effects of changing the relativistic velocity  $\beta$  value with  $\Delta Z = -1$ . It should be noted that the effects of changing  $\beta$  are more pronounced in the forward  $37^\circ$  ring then in the  $90^\circ$  ring which is due to the  $\theta$  dependence of the Doppler energy correction in Eq. 3.18. The lower right figure is calculated with the same  $\beta$  value as the top left figure, but with a different  $\Delta Z$  to illustrate the effects of shifting the target location.

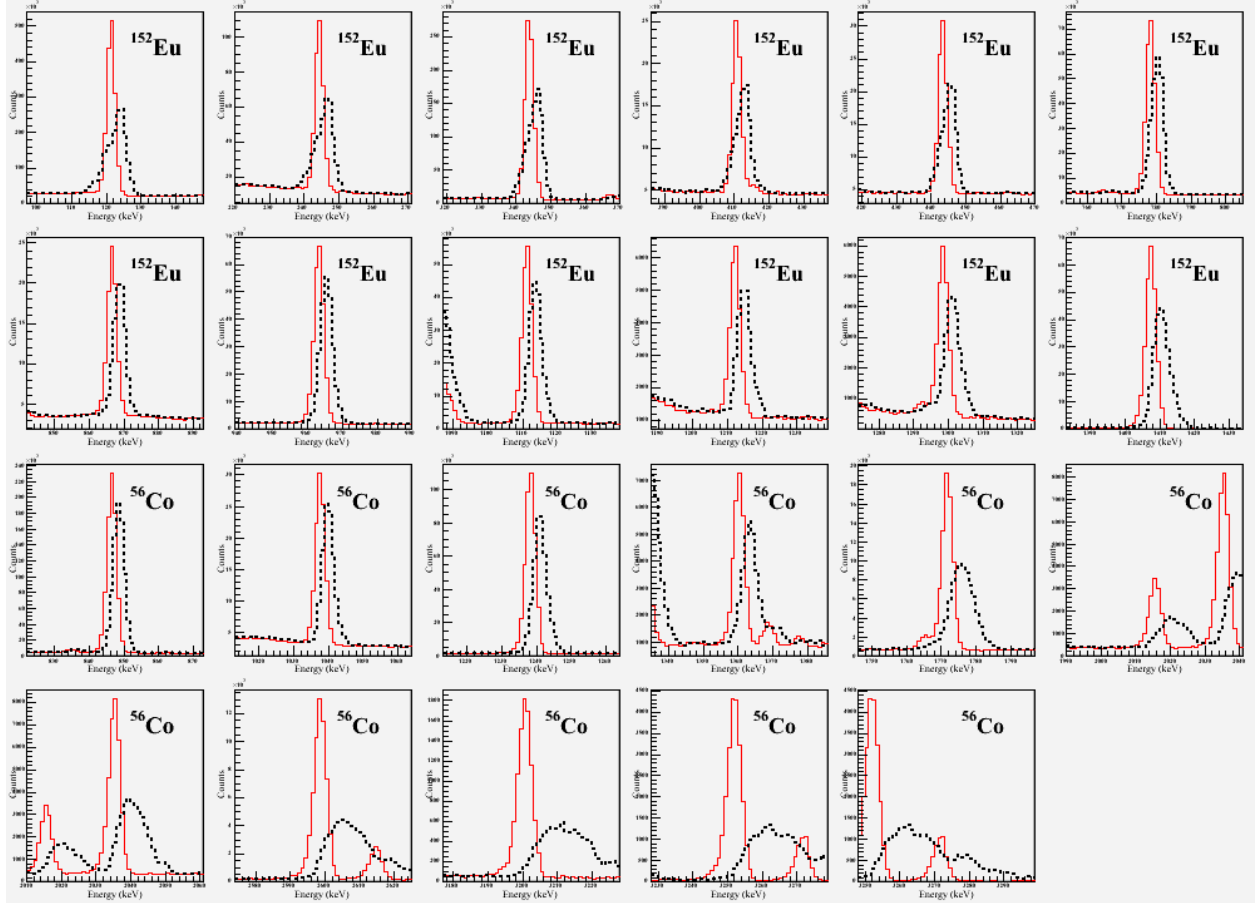


Figure 3.20: A comparison of the uncalibrated raw central contact energy spectra (dashed black line) to the calibrated energy spectra (red line). The top two rows are from a the same  $^{152}\text{Eu}$  data run where each figure is focused in on one of the 12 photopeak energies of interest from Table 3.1, starting with the lowest energy in the top left and increasing in energy from left to right. The bottom two rows are from the same  $^{56}\text{Co}$  data run with a similar peak focus for each figure. All of the spectra are taken by summing the energy spectra of all 17 SeGA detectors together.

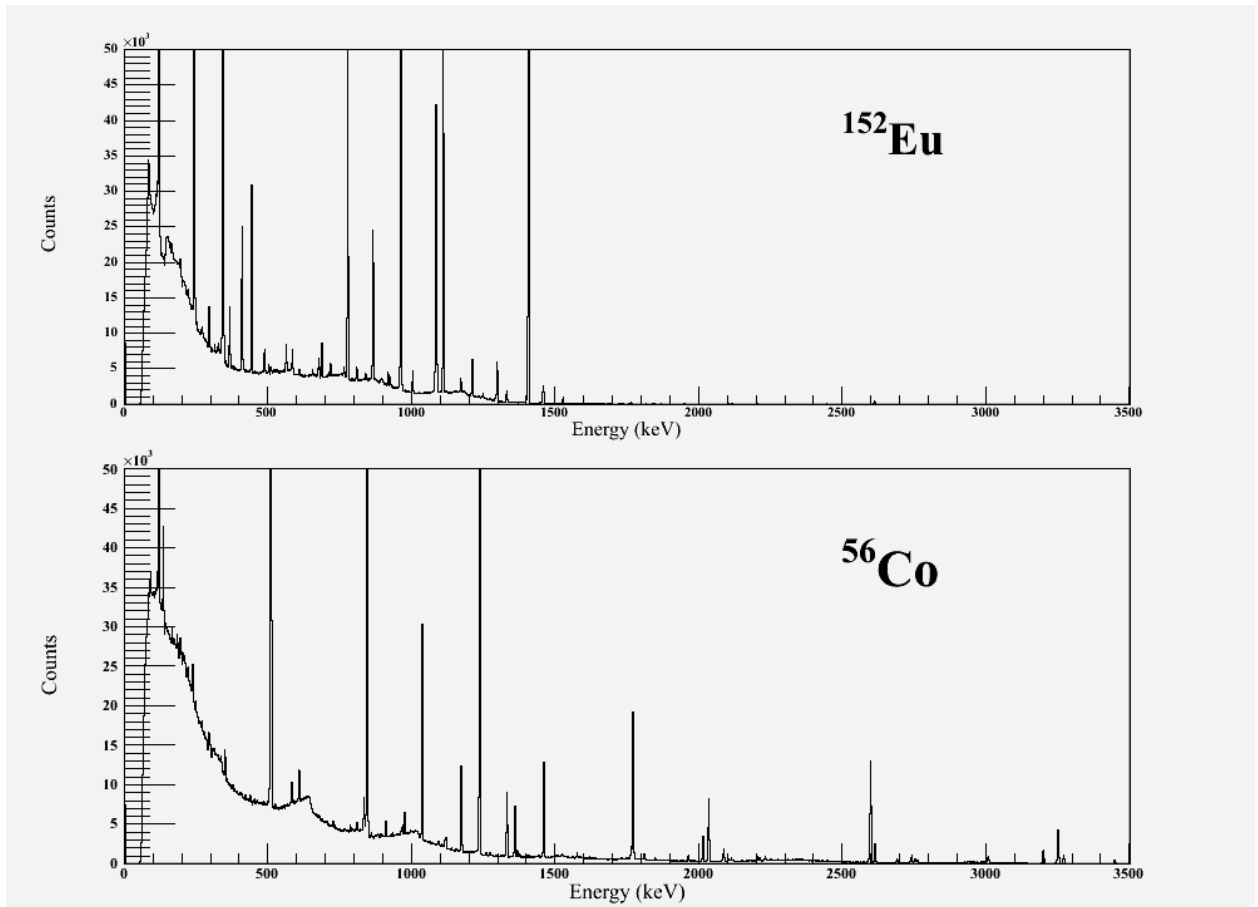


Figure 3.21: The calibrated energy spectra for  $^{152}\text{Eu}$  and  $^{56}\text{Co}$  sources from the calibrated central contact energies summed over all 17 SeGA detectors.

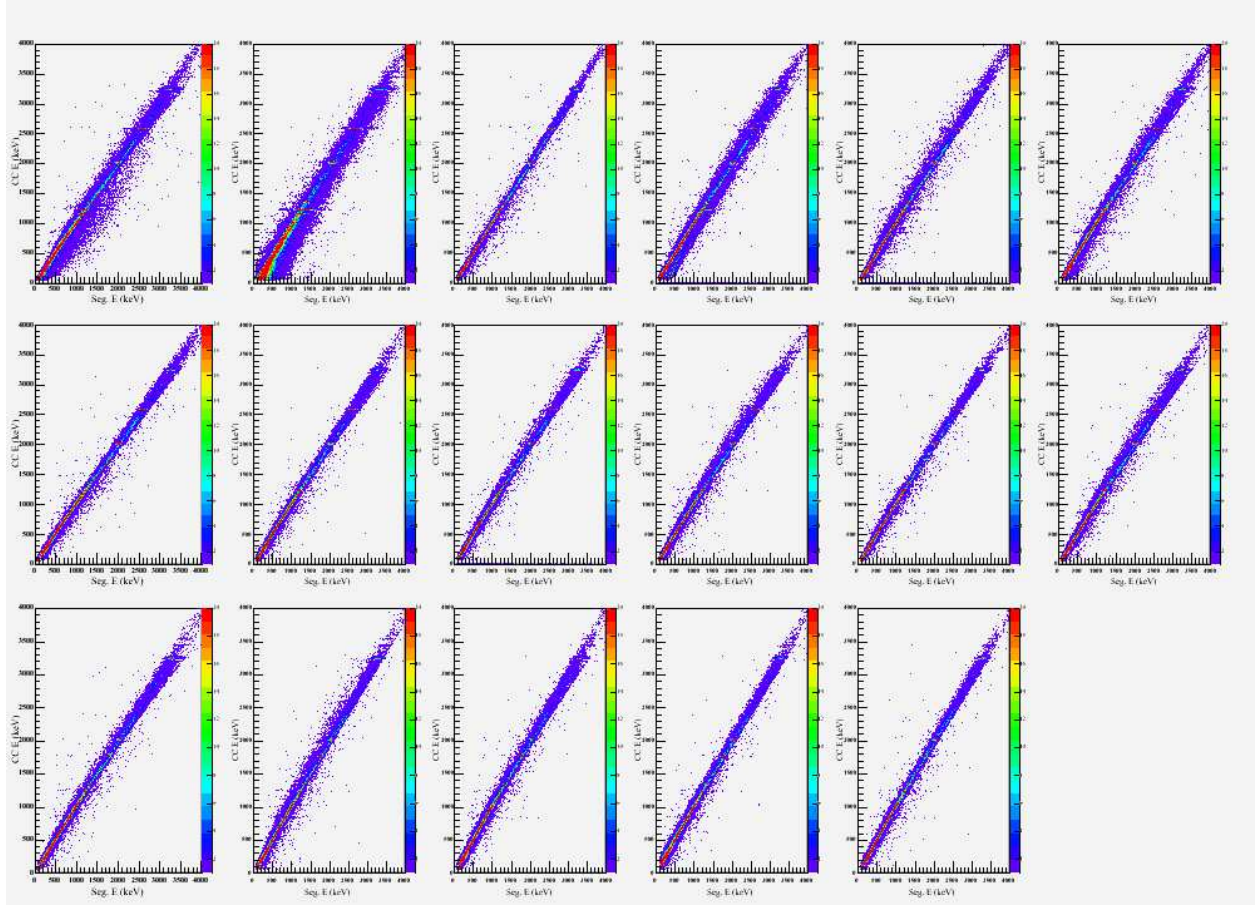


Figure 3.22: A comparison of the calibrated central contact energy (horizontal axis) to the summed calibrated segment energies (vertical axis) for each  $\gamma$ -ray event. Each of the 17 plots corresponds to the data from one of the 17 SeGA detectors in the array. This data was taken from a  $^{56}\text{Co}$  calibration source run. It can be seen that the majority of the events in each detector lie along a straight line with a slope of 1, which shows that the segment energy calibration parameters are in good agreement with each detectors central contact energy.

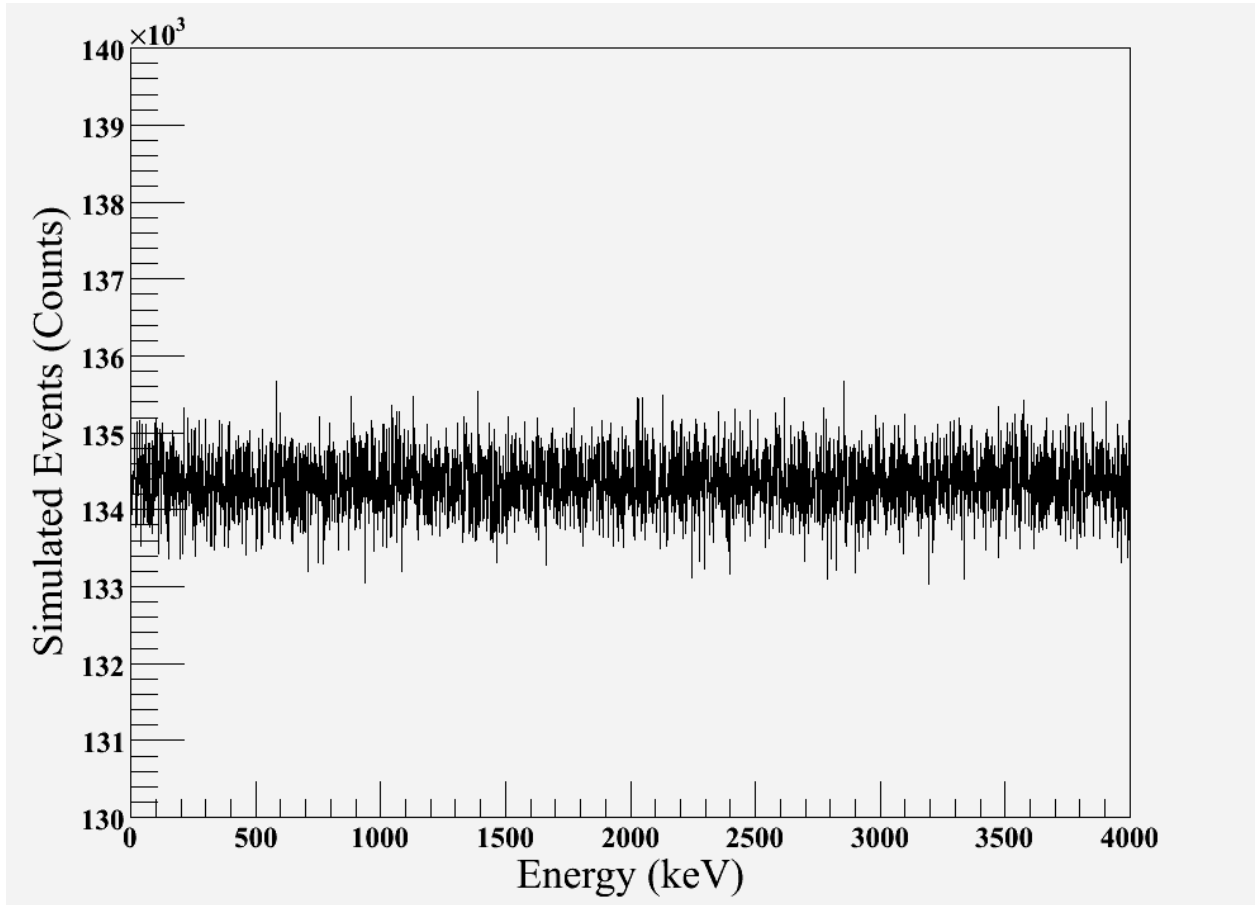


Figure 3.23: The GEANT simulated energy spectrum of the total emitted photons from a stationary source at the SeGA target position. The photons are emitted in all directions for energies of 0 keV to 4000 keV in 1 keV increments.

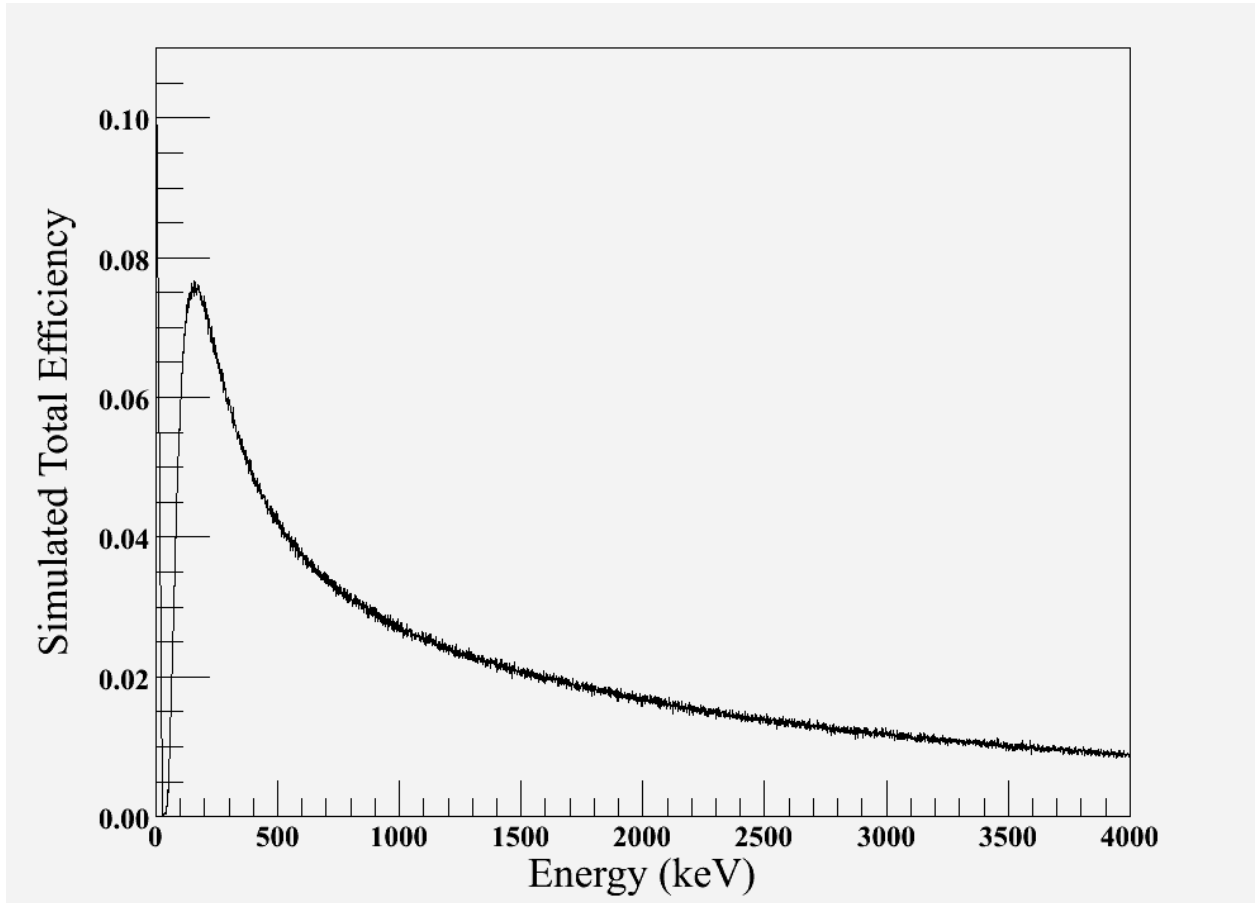


Figure 3.24: The GEANT simulated total detection efficiency of SeGA corresponding to the total emission spectrum in Fig. 3.23. The detection efficiency takes into account the effects of Compton scattering and does not count an event as being detected unless the amount of total energy deposited in the detectors active region is within the same acceptance region used for the real source efficiency calculations based on the energy resolutions in Table 3.3.

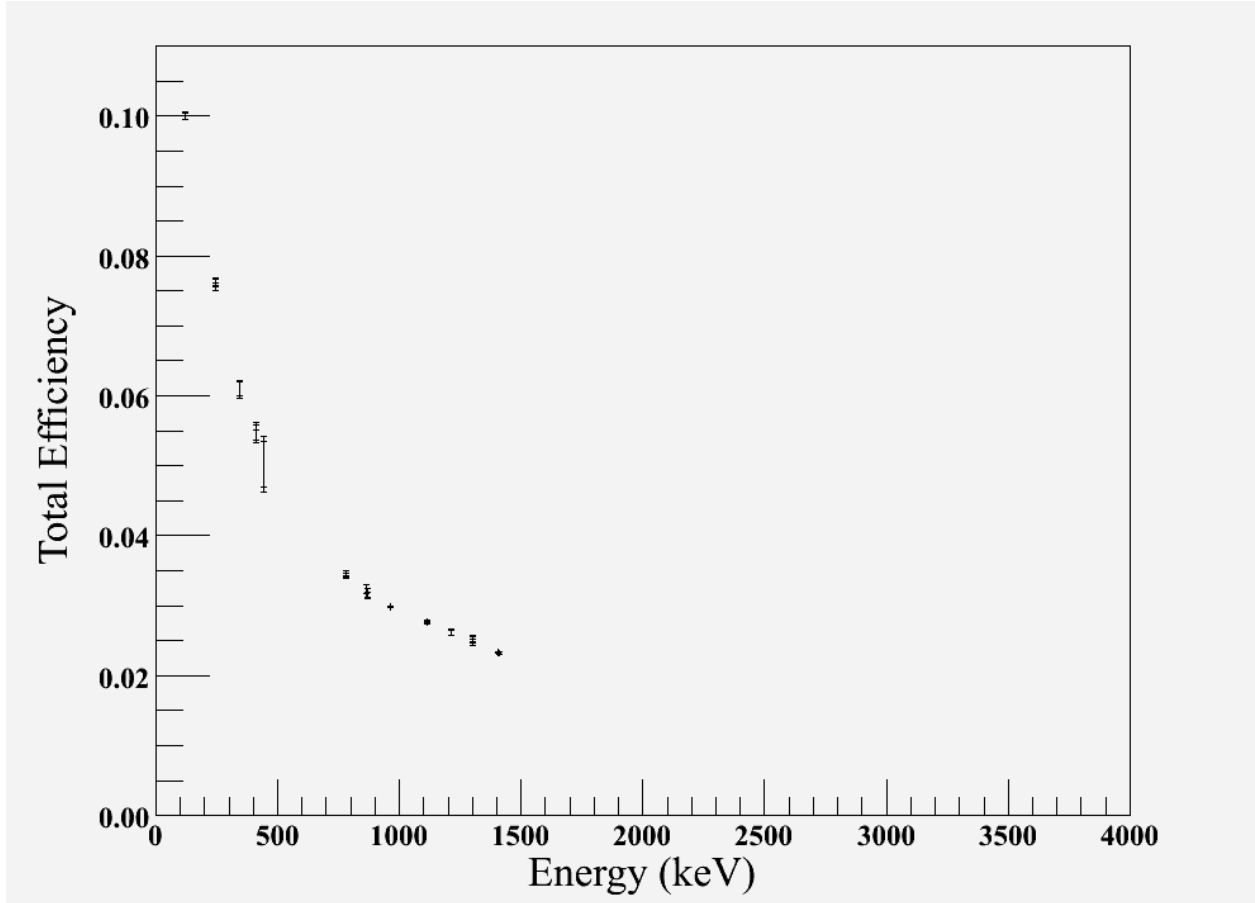


Figure 3.25: The measured SeGA total efficiency for  $^{152}\text{Eu}$  source runs. The data points are for the energies specified in Table 3.1 and all the applicable stationary source data runs in Table 3.2 in which the radiation source was located at the SeGA target position. .

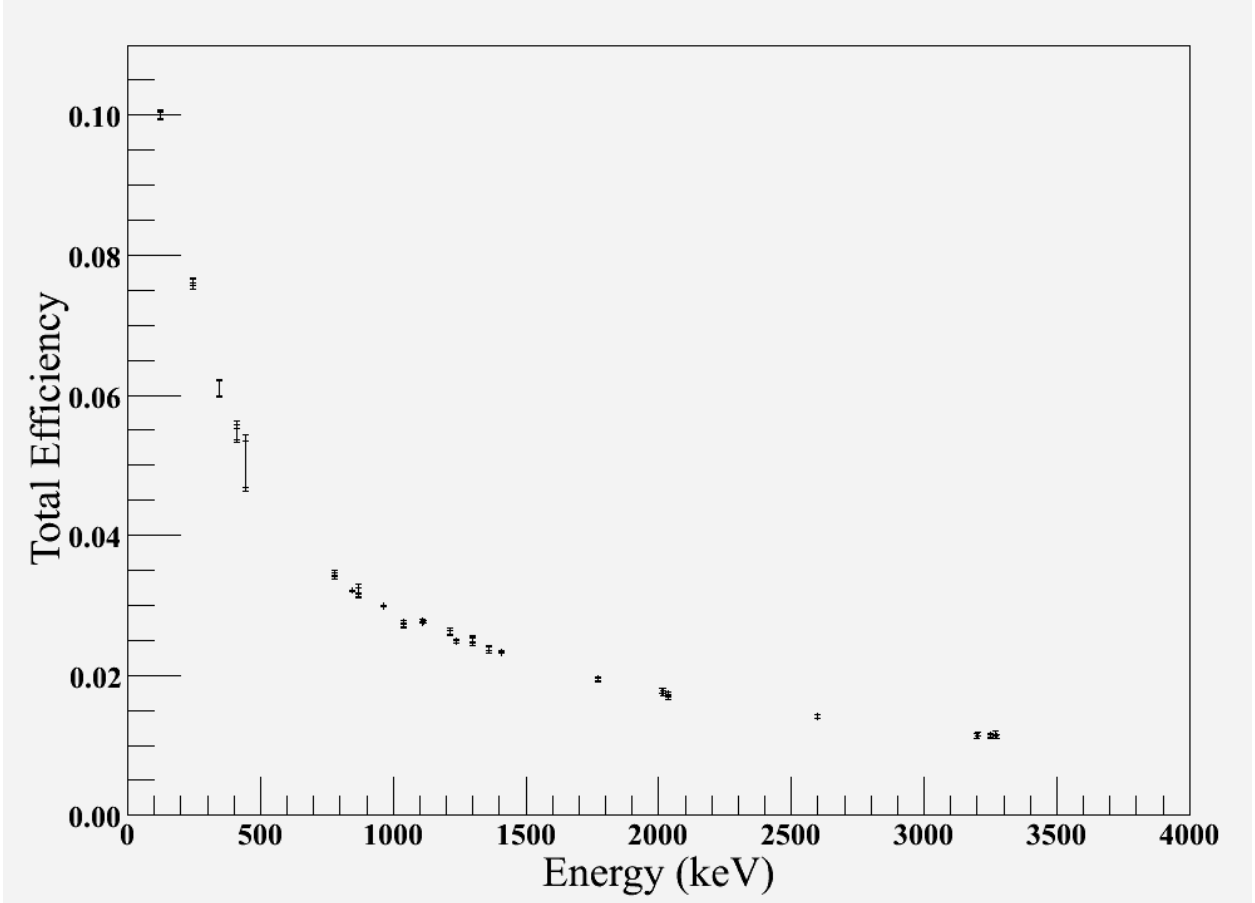


Figure 3.26: The measured SeGA total efficiency for all  $^{152}\text{Eu}$  and  $^{56}\text{Co}$  source runs listed in Table 3.2. The  $^{152}\text{Eu}$  data points are the same as Fig. 3.25, with the addition of the  $^{56}\text{Co}$  source efficiency data normalized to the absolute total efficiency.

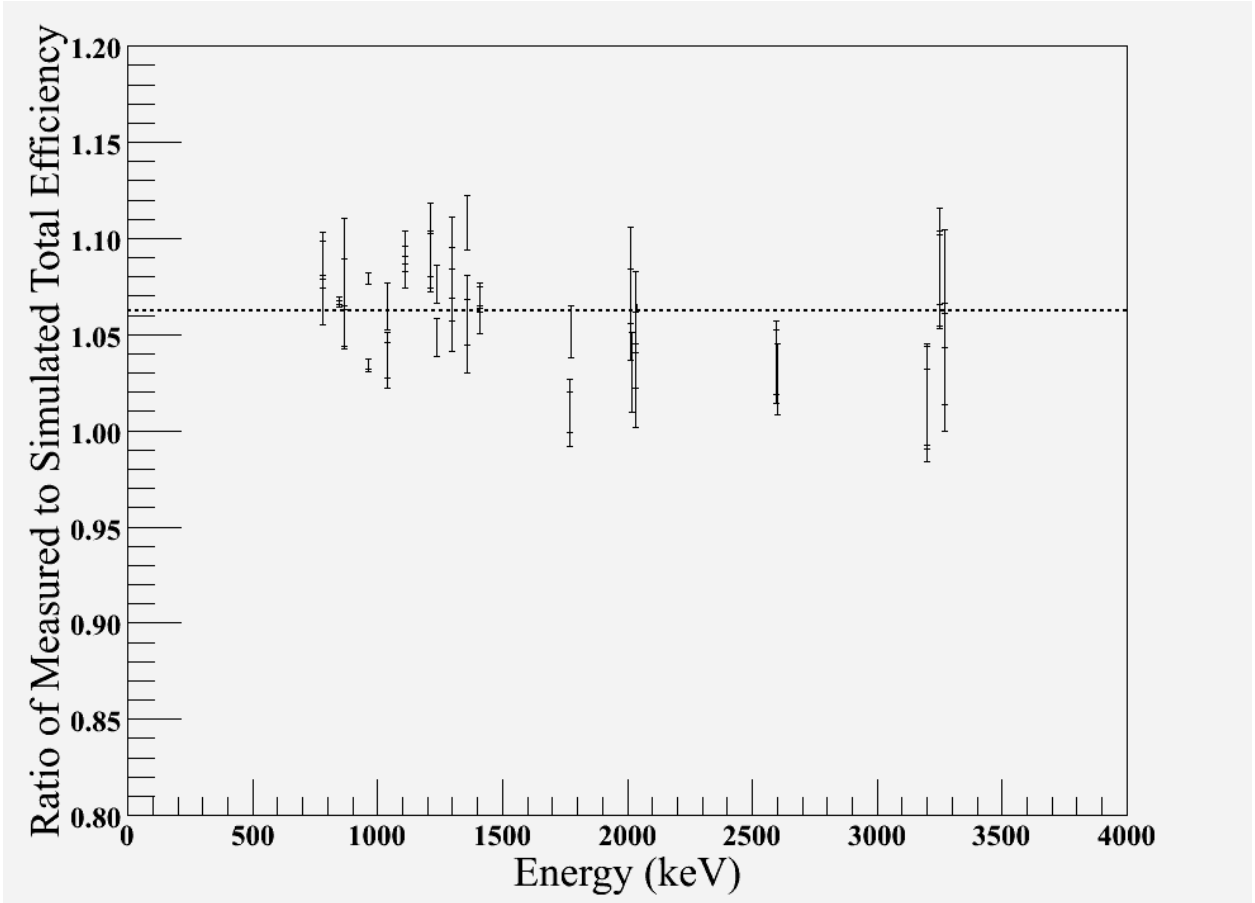


Figure 3.27: A plot of the ratio of measured efficiencies from Fig. 3.26 to the simulated efficiency over the relevant energy ranges. The horizontal line is the weighted average of the data points and is fixed at 1.063.

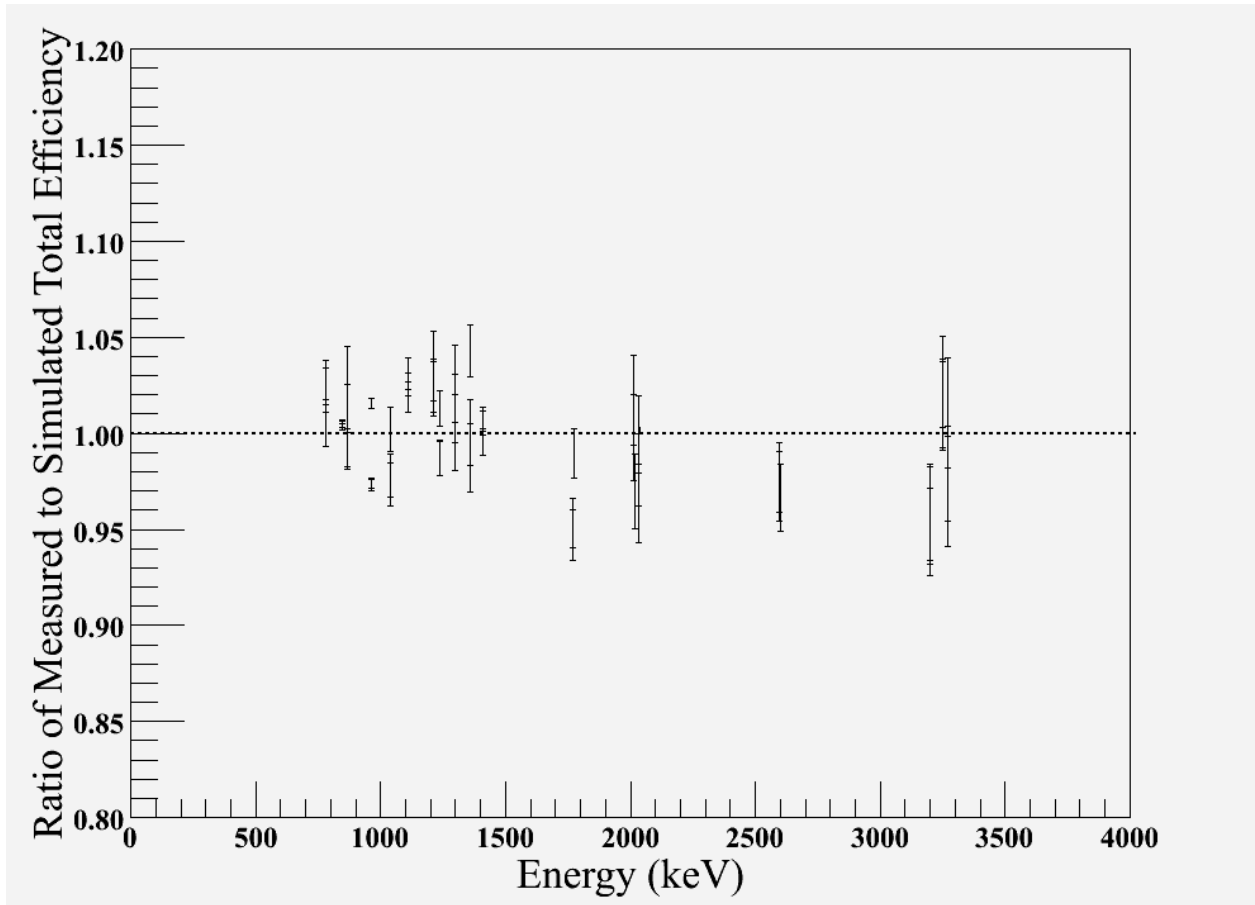


Figure 3.28: A plot of the ratio of measured efficiencies to the simulated efficiency including the correction term. This is the same as Fig. 3.27 with the simulation efficiencies adjusted by the scale factor of 1.063. The horizontal line is the weighted average of the data points which is 1.00. This shows a very good agreement between the simulated  $\gamma$ -ray detection efficiencies and the measured efficiencies.

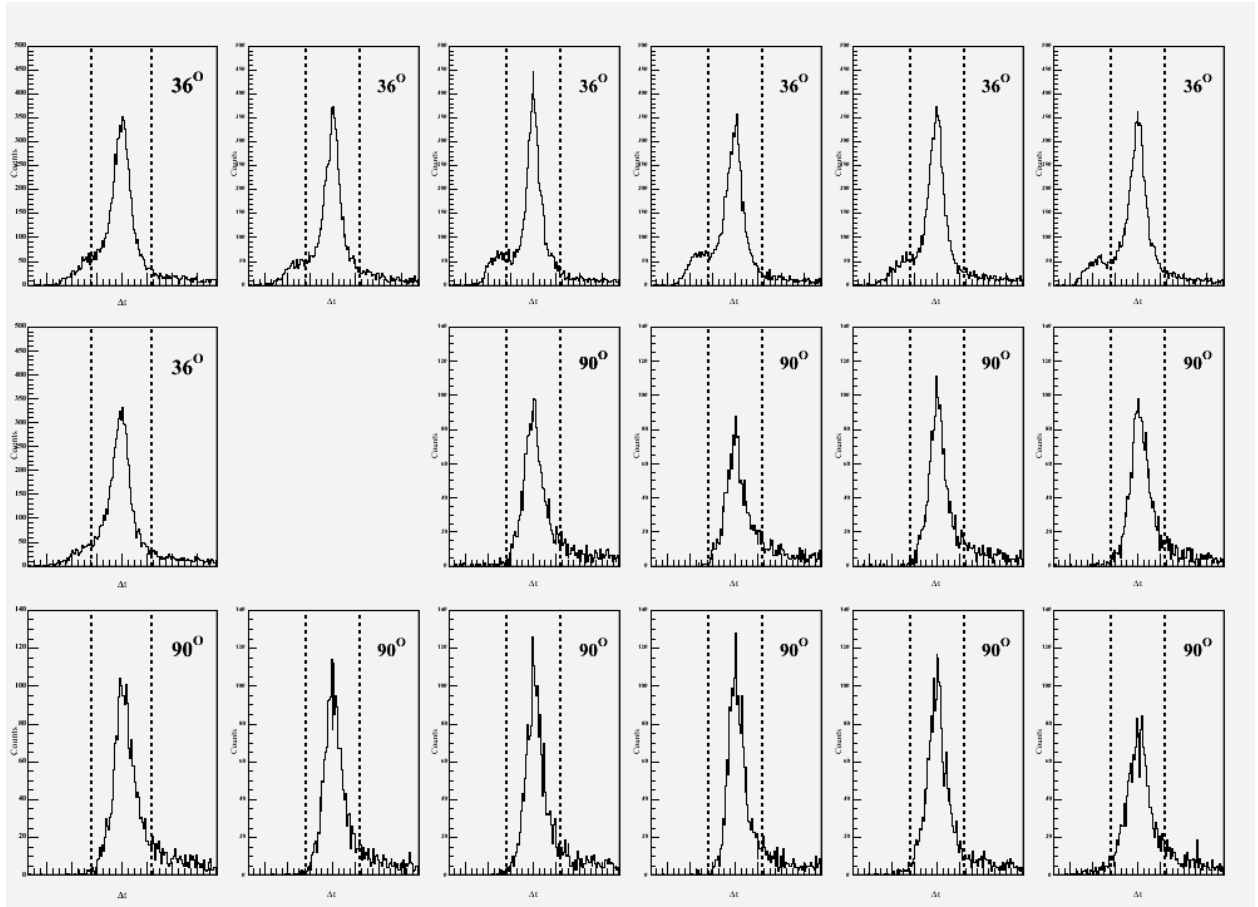


Figure 3.29: Each plot is for the timing difference between the detectors timing signal and the events trigger signal for each individual SeGA detector. Each detector is labeled by which detector ring angle it is in. The dashed line represents a coincidence logic *and*-gate that is applied to the detector. The events occurring outside the coincidence gates are from other reactions not associated with the main knockout reaction. This set of histograms is from the  $^{26}\text{Si} \rightarrow ^{25}\text{Si}$  reaction data, but the  $^{30}\text{S} \rightarrow ^{29}\text{S}$  looks very similar.

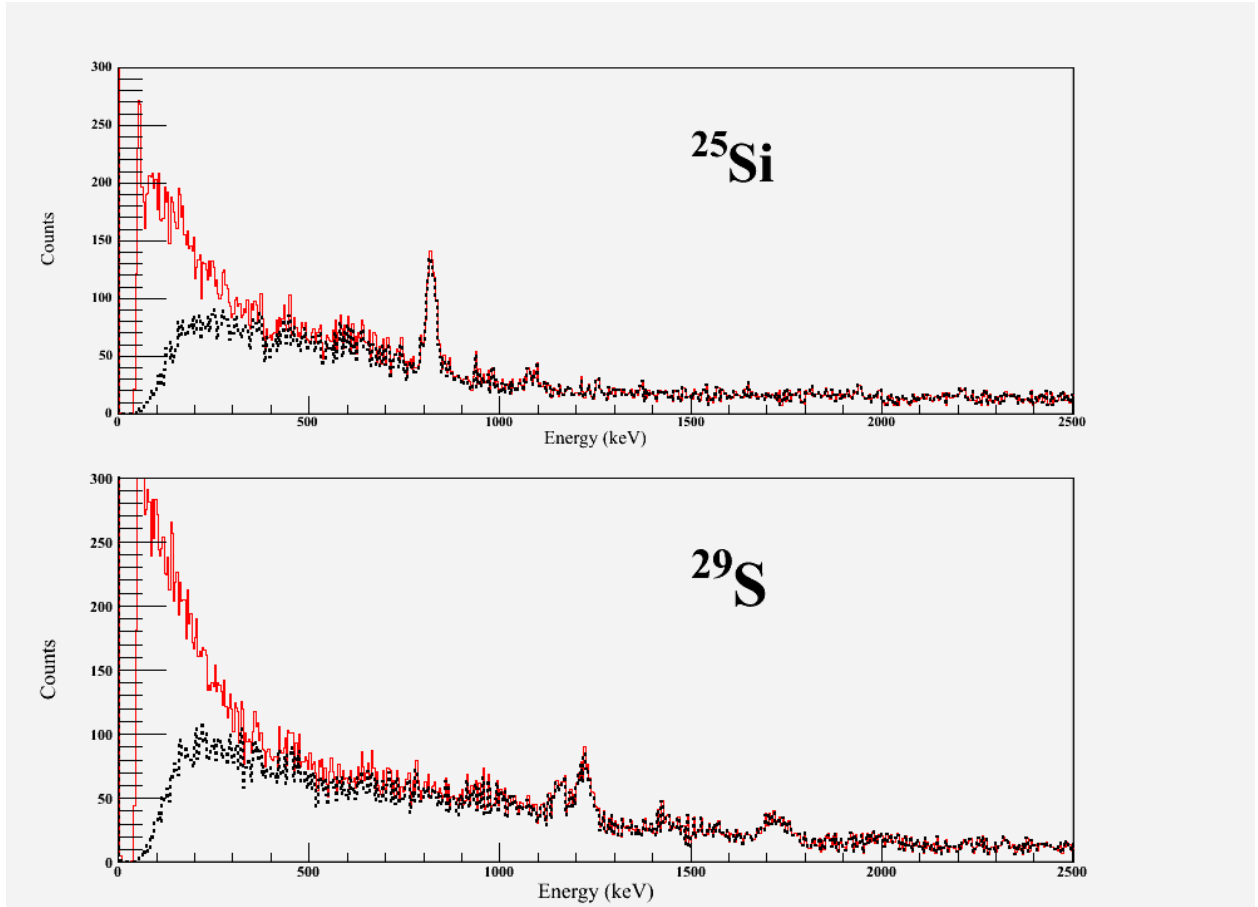


Figure 3.30: The particle- $\gamma$  coincidence gated Doppler reconstructed  $\gamma$ -ray energy spectra for  $^{25}\text{Si}$  and  $^{29}\text{S}$ . The data set without a central contact timing gate is shown as the solid red line, and the same data taken with the timing gate shown in Fig. 3.29 applied is represented by the dashed black line.

### 3.4 Data Acquisition Triggers and Signal Timing

The data acquisition system used in the experiment was a combination of the individual SeGA and S800 systems. Event data is recorded only if specified conditions are met. These conditions are referred to as triggers, and each recorded data event can be classified by its triggering condition. The experiment used three types of triggering conditions: particle-single (PS) events,  $\gamma$ -single (GS) events, and particle- $\gamma$  coincidence (COINC) events. PS triggers are initiated by a signal from the first scintillator in the S800 focal plane. The timing signal from each of the SeGA detectors are sent to an OR logic circuit that puts out a signal for the GS trigger if at least one SeGA detector fired. The COINC triggers are a combination of near simultaneous PS and GS trigger events. A short timing logic gate of around 400 ns is opened when a PS event occurs, the GS signal is processed through an appropriate timing delay, and if the time delayed signal occurs during the open logic gate the event is recorded as a COINC event. The data acquisition system is designed to allow any combination of PS, GS, or COINC events to be collected at the same time. Because of the time required to process the signals from the various detectors, the data acquisition allows for each of the three trigger conditions to be independently down scaled by integer factors in an effort to minimize the amount of dead time in the data acquisition system from pile-up effects in the signal collection and digital processing. The down scale factor value (DS) caused the associated triggering event to only be written to disk after the trigger had fired DS number of times. The data acquisition system records the scalar total for each trigger regardless of whether an event is recorded to disk or not. The GS events were used exclusively for SeGA calibration measurements in which the particle data was not necessary. Similarly, the PS events were used exclusively for the particle detector calibrations such as the CRDC mask calibrations discussed in Sec. 3.2.2.1, and the unreacted beam normalization runs as discussed in Sec. 3.2.4. During the residual reaction product particle- $\gamma$  data collection runs, both the PS and COINC data events were taken simultaneously with an appropriate downscale factor applied to the PS trigger and a downscale factor of unity applied to the COINC triggers.

The data acquisition live-time ratio is the amount of time that the data acquisition system was actually available to take data to the total amount of time that events were occurring. The live-time ratio is strongly related to the beam rate. As discussed in Sec. 3.2.2.1, the

CRDCs in the S800's focal plane have a limiting count rate at which point the data acquisition system begins to miss a large number of good events because of the processing time of collecting and recording the previous event's signal data. The beam rate was constantly monitored during the experiment to make an effort to keep the counting rate and live time ratio as high as possible. The raw trigger readouts could be measured as a scalar output separately from the events being digitized and written to disk. The beam rates used were low enough that the raw trigger readout can safely be considered to be the absolute number of triggered events that occurred regardless of whether or not the event was written to disk. The live-time ratio ( $\tau$ ) is then determined for each trigger condition separately as

$$\tau = \frac{n_{etrig}}{n_{raw}}, \quad (3.21)$$

where  $n_{etrig}$  is the number of the trigger events written to disk and  $n_{raw}$  is the downscaled raw number of times that specific trigger fired. The advantage of directly comparing the number of recorded events to the actual number of triggers is that it removes any direct beam rate dependency in calculating the live-time.

Timing signals are used in the particle time-of-flight measurements between the extended focal plane (XFP), the objective focal plane (OBJ), and the first S800 focal plane scintillator (E1). Additionally, the timing signals are used as discussed in the previous paragraph for the COINC trigger events as well as to synchronize the signal readouts of all detectors for every data event. PS and COINC events require that a particle be detected in the S800 focal plane detectors, because of this the E1 timing signal is used as a start signal for both of these events. The E1 detector is the last detector and is located at the end of the beamline, so logically, the real timing signals from all of the other upstream detector systems (apart from the S800's ion chamber and CRDC detectors) occurs before the event start signal is produced, so to remedy this, all of the timing signals are run through separate signal time delays. The amount of time for each delay is adjusted with the projectile cocktail beam on target to place all of the delayed timing signals to occur during a small time window (around 400 ns) after the event start signal from E1. The time-of-flight measurements are the only measurements that are value sensitive to the amount of delay introduced to each timing signal, however as described in Sec. 3.2.3, only a relative time-of-flight difference is required for particle identification, so the time-of-flight measurements are not true to life.

It was discovered several months after the end of the experiment that there was a

computer software bug in the data acquisition system. The bug was introduced because a portion of the stable working code was accidentally replaced with an untested modification that was being worked on for a future release. The untested modification was an effort to test the validity of COINC triggered events after the event was digitized but before it was recorded to a hard-drive disk in order to reduce the number of invalid COINC events written to disk and increase the data acquisition live-time. The portion of code made two boolean checks: one was for a specific condition to be met in the SeGA data packet and the other was for a specific condition in the S800 data packet. If both conditions were met, a logical AND condition on the two checks would allow the data packet to be written out, if it failed then the packet would be dropped and nothing would be written out to disk. The bug was the result of a failure of the S800 valid data condition to be updated for the current event buffer until after the SeGA-S800 AND conditional was checked. A diagram illustrating how the event buffer flow was intended to work and how it actually executed is shown in Fig. 3.31. The standard experimental procedure at the time was to not perform any validation checks on the digital data packets and write all events that satisfied the triggering conditions to disk. The initial problem was that during any experiment using the S800-SeGA set-up, there were random events in which the COINC trigger was fired, but the data packet that was written to disk was empty or missing the SeGA or S800 portion of the packet. Since these occurrences are random, the associated event packets can be ignored during the analysis and the only consequence is added acquisition dead time from writing the corrupted event packet to disk. After thoroughly inspecting the raw event data files and the affected acquisition code, it was determined that only COINC triggered events were affected by the bug. The COINC events were only written to disk if the SeGA validation check for the current COINC data packet was true and the S800 validation check for the previous COINC data packet was true. The result was a loss of good data packets and several data packets written to disk that were labeled as COINC events but were missing the S800 data. The solution was to only use COINC events for which there was a complete data packet written to disk. The only consequence of this bug was an increase in the data acquisition dead time for COINC events only.

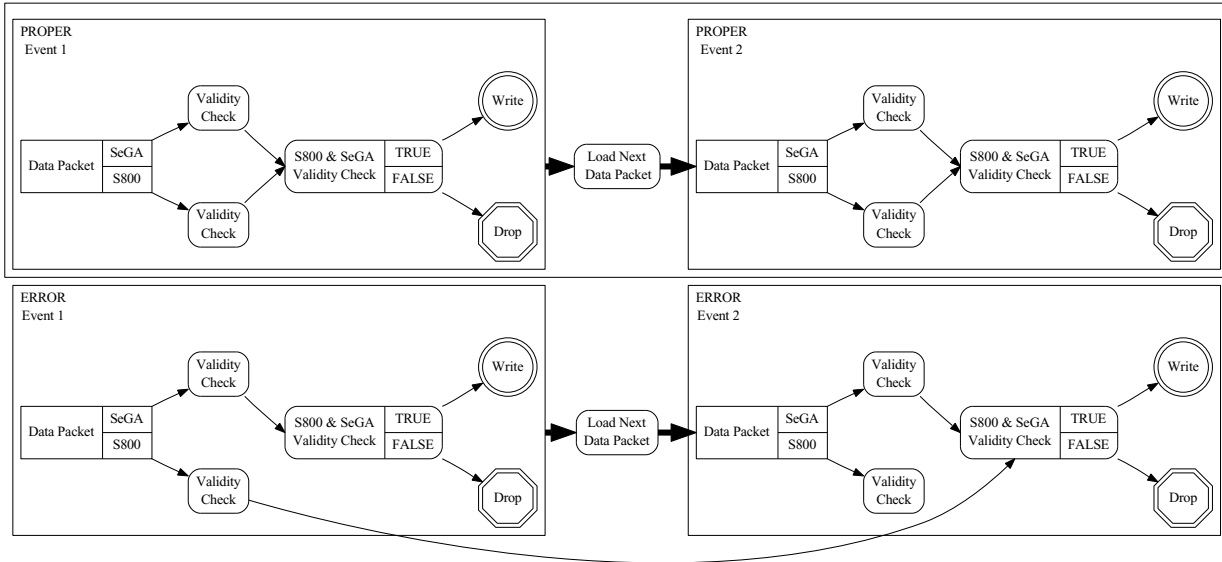


Figure 3.31: A flow chart of two sequential data event packets processing from left to right. This procedure was from a portion of code that was still a work in progress and was accidentally placed in the stable version of the data acquisition code. The top diagram was the intended data buffer processing flow and the bottom diagram is what was implemented. The data flow starts at the point in which the data packet has been created by digital conversion of all the detector systems after a COINC triggered event. A process is performed to check the validity of the digitized SeGA and S800 data packets, then these checks are processed through a logical AND process. If the AND comparison is true, then the data packet is written to disk, if it is false it is dropped and nothing is written to disk. The data collection system then is cleared to allow for the next triggered event to be processed. The error in this procedure is shown in the bottom row when the S800 Validity Check process is not processed for the current event packet, but is instead applied to the next data packet, this is a continuous process for all subsequent data packets (e.g., the S800 Validity Check for Event 2 is carried over to Event 3 and so forth).

# CHAPTER 4

## ANALYSIS AND CONCLUSIONS

The following chapter will present the analysis results of the  ${}^9\text{Be}({}^{26}\text{Si}, {}^{25}\text{Si}+\gamma)$  and  ${}^9\text{Be}({}^{30}\text{S}, {}^{29}\text{S}+\gamma)$  reactions. The first section will present an overview of the analysis procedure building on what was discussed in Ch. 3. The analysis results for the  ${}^{26}\text{Si}\rightarrow{}^{25}\text{Si}$  are presented in Sec. 4.2 and the results of  ${}^{30}\text{S}\rightarrow{}^{29}\text{S}$  are in Sec. 4.3.

### 4.1 Analysis Procedure

The two reactions being studied were performed as part of Experiment 03021 at the NSCL running over the dates of Nov. 20-30, in 2004. The proposal for Experiment 03021 was the first test of the two-neutron knockout reaction mechanism. The initial plan was to study the two neutron knockout from  ${}^{26}\text{Si}$ ,  ${}^{30}\text{S}$ , and  ${}^{32}\text{Ar}$ , and by a slight refocusing of the S800 spectrometer, it was determined that it would be feasible to look at the single neutron knockout from  ${}^{26}\text{Si}$  and  ${}^{30}\text{S}$ . The results of the two neutron knockout experiments have been published in Ref. [49] and Ref. [50]. The observable quantities of interest that can be determined from neutron knockout reactions using the SeGA-S800 set-up are the inclusive and partial state reaction cross sections, the longitudinal momentum distributions, and the  $\gamma$ -ray energies and relative intensities from the de-excitation of the states directly populated in the reaction.

#### 4.1.1 Cross Section Calculation

As discussed in Chap. 2, the cross section measurements from neutron knockout reactions can be used to extract spectroscopic information pertaining to the single particle occupational strengths. A cross section is a measurement of the probability of a reaction populating a specific bound state of the residual nucleus from a specific initial state of the projectile

nucleus. The inclusive cross section ( $\sigma_{inc}$ ) is the total probability for populating any bound state of the fragment residue from the projectile. Given the rate of beam particles  $N_b$  incident on  $\nu_t$  target particles per unit area that create  $N_f$  fragmentation residues of interest, the inclusive cross section is given by

$$\sigma_{inc} = \frac{N_f}{N_b \nu_t}. \quad (4.1)$$

The cross section for populating a specific bound state of the fragment residue is referred to as a partial cross section. The relationship between the partial state cross sections and the inclusive cross section is

$$\sigma_i^{\text{partial}} = b_i \sigma_{inc}, \quad (4.2)$$

where  $b_i$  is the reaction's branching ratio to that particular state denoted by the subscript  $i$ . The sum over all the partial state cross sections is equal to the inclusive cross section.

The number of target particles per unit area in Eq. 4.1 is determined by  $\nu_t = \nu x$ , where  $\nu$  is the target particle number density and  $x$  is the thickness of the target. The target used in this experiment was a uniform  ${}^9\text{Be}$  target with  $\nu_t = 2.52 \times 10^{-5} \text{ mb}^{-2}$  ( $x = 376 \text{ mg/cm}^2$ ), where the units are in millibarns and one barn is equal to  $10^{-28} \text{ m}^2$ . The largest source of error in  $\nu_t$  is from a 5% uncertainty in the target's thickness as quoted from the manufacturer.

The values of  $N_f$  and  $N_b$  can both be calculated from the generalized formula

$$N_i = \frac{N_i^{\text{obs}} \lambda_{DS}}{N_{norm} \tau_i \varepsilon_i}. \quad (4.3)$$

The two values in the numerator are the number of events recorded with the downscaled PS trigger condition  $N_i^{\text{obs}}$ , and the PS trigger DS factor  $\lambda_{DS}$ . The denominator consists of three terms: a normalization factor  $N_{norm}$ , a live-time correction term  $\tau_i$ , and a particle detection efficiency correction term  $\varepsilon_i$ .  $N_f$  and  $N_b$  have to be determined from separate data runs and are respectively referred to as fragmentation/reaction runs and unreacted beam normalization runs.  $N_{norm}$  serves to normalize the fragmentation reaction runs to the beam normalization runs and must be consistently proportional to the total beam flux steered through the target position. To accommodate this data normalization, the raw scalar output of the extended focal plane (XFP) and object plane (OBJ) scintillators are monitored during both types of runs. Because the XFP scintillator was degrading too rapidly over the full course of the fragmentation reaction runs, it could not be used reliably over the amount of time needed, and only the OBJ scintillator was used for beam flux monitoring. As a

result,  $N_{norm}$  is equal to the total raw scalar output of the OBJ scintillator over the course of the data collection. There are a few sources of systematic errors that must be accounted for in the cross section measurements along with the statistical errors. The systematic errors are from the uncertainty of the particle identification software gates ( $\sim 5\%$ ), uncertainties arising from fluctuations in the beam purity and stability ( $\sim 5\%$ ), and the corrections for the limited momentum/angle acceptance of the S800 ( $< 10\%$ ). These systematic uncertainties are added in quadrature to the statistical errors.

#### 4.1.1.1 Beam Normalization Rate

As previously stated in Ch. 3, the projectile beam incident on the secondary target is composed of a cocktail of nuclear species and the beam consistency has to be determined by focusing the unreacted projectile beam into the focal plane of the S800 and identifying the beam purity of the projectile of interest. The  ${}^9\text{Be}$  target is still in place during the beam normalization runs, so the unreacted beam focused in the S800 focal plane does undergo energy loss in the target and the scattering effects are small. Because the beam normalization runs cannot be performed at the same time as the reaction data runs and require adjusting the spectrograph settings, a normalization run is performed shortly before the first reaction data run and also shortly after the last reaction data run, and the results are averaged together to account for any small changes in beam consistency and detector degradation over the course of the reaction data runs. The beam normalization rate runs are used to determine the value of  $N_b$  in Eq. 4.1. The live-time  $\tau_b$  is determined from the PS trigger live-time as described in Sec. 3.4 and Eq. 3.21. The particles that are steered into the focal plane are the unreacted beam particles, so there is no need to identify the incident beam particles based on time-of-flight between the XFP and OBJ scintillators as described in Sec. 3.2.3, so the XFP scintillator can effectively be ignored in the beam normalization runs. The beam dispersion angles after the target are very small, so the beam's profile in the CRDC is small enough to avoid the bad section of the CRDC detectors discussed in Sec. 3.2.2.1 and there is no need to determine a CRDC lost count correction factor as described in Sec. 3.2.4. The total particle detection efficiency for the unreacted beam normalization rate is

$$\varepsilon_b = \varepsilon_{obj} \times \varepsilon_{crdc1} \times \varepsilon_{crdc2}, \quad (4.4)$$

where  $\varepsilon_{obj}$ ,  $\varepsilon_{crdc1}$ , and  $\varepsilon_{crdc2}$ , are the detection efficiencies of the OBJ scintillator, CRDC1, and CRDC2 determined using Eq. 3.15.

The value of  $N_b^{\text{obs}}$  is determined by creating a particle-identification logic gate around the particle of interest in the two dimensional particle identification spectrum described in Sec. 3.2.3 and extracting the total number of downscaled PS triggered events that were collected and are inside the logic gate.

#### 4.1.1.2 Fragmentation Rate

The fragmentation rate  $N_f$  from Eq. 4.1 is determined from collecting data in which the fragmentation residue of interest is steered into the S800's focal plane detectors. It is important that the secondary beam settings used in the beam normalization rate calculations are the same as those used for the fragmentation rates. The particle identification of the reaction products is described in Sec. 3.2.3. The fragmentation rate calculations require that the XFP scintillator and the OBJ scintillator be used for identification of the incident projectile. The fragmentation residues are more dispersed in the focal plane than the unreacted beam used for the beam normalization runs, so the CRDC counting correction as described in Sec. 3.2.4 must be taken into account. The live-time  $\tau_f$  is determined from the downscaled PS trigger live-time as described in Sec. 3.4 and Eq. 3.21. The total particle detection efficiency for the fragmentation rate calculations are

$$\varepsilon_f = (\eta_{crdc} \times \varepsilon_{crdc1} \times \varepsilon_{crdc2}) (\varepsilon_{xfp} \times \varepsilon_{obj}), \quad (4.5)$$

where  $\eta_{crdc} \times \varepsilon_{crdc1} \times \varepsilon_{crdc2}$  is the total CRDC correction from Eq. 3.16, and  $\varepsilon_{xfp}$  and  $\varepsilon_{obj}$  are the detection efficiencies of the XFP scintillator and the OBJ scintillator calculated using Eq. 3.15.

The number of observed fragment residues,  $N_f^{\text{obs}}$ , is determined by creating a particle-identification logic gate on the two dimensional particle identification spectrum and another logic gate on the incident beam particle in the one dimensional XFP-OBJ time-of-flight spectrum. The fragmentation rate must be corrected for the number of counts lost in the bad section of the CRDC, so  $N_f^{\text{obs}}$  is equal to the number of PS trigger events recorded that satisfy both of the logic gates multiplied by the CRDC correction factor  $\eta_{crdc}$ . It should be noted that was very little count loss due to the limited acceptance angle of the S800 spectrograph which would have shown up as clipping at the edges of the angle in the focal

plane (AFP) spectrum or the parallel momentum distribution spectrum ( $d_t$ ). It is because of this that both the CRDC efficiency and the number of observed events are both corrected by the same  $\eta_{crdc}$  factor. In Eq. 3.15, the  $\eta_{crdc}$  factor cancels itself out in the numerator and denominator, however it is kept in the calculations to properly account for the additional error introduced from the lost counts.

During the course of an experiment, the beam intensity and detection efficiencies are naturally subject to fluctuations, but it can be safely assumed that over the course of one to two hours these fluctuations can be considered negligible. Because of this, the total experimental run time for the fragmentation data was divided into a series of smaller runs in which each run covered an elapsed time of between one to two hours. The calculation of  $N_f$  was performed for each of the smaller runs individually, and then the error weighted average of all of the fragmentation runs is calculated and used for  $N_f$  to calculate the inclusive cross section.

## 4.1.2 $\gamma$ -Ray Analysis

The Doppler-reconstructed  $\gamma$ -ray energy spectrum provides a means to determine the energy levels and the probabilities of populating selective states in the reaction residue. It also allows for observation of any photo-decay branching cascades from the populated states. The photon detection efficiency is significantly lower than that of the particle detection efficiency, because of this the full set of fragmentation data runs is required to acquire a  $\gamma$ -ray energy spectrum of statistical significance.

### 4.1.2.1 Determination of Populated Excited States

The  $\gamma$ -rays observed in coincidence with a fragmentation residue only represent the electromagnetic transitions between bound states of the residue. When determining the actual energy separations of the observable bound states based on the  $\gamma$ -ray energy spectrum, it is very important to take into consideration the possible decay branching of excited states into other excited states as well as the ground state. The partial cross sections are determined from the observed photopeak counts, and because they are meant to represent the direct reaction feeding into a specific final state, it is important to take into account any feeding from one excited state into another that would cause an inflation in the photopeak's intensity that is not the result of a direct reaction population. It is a safe assumption that all of the

bound states observed in the current work are well within the  $sd$ -shell as described in Sec. 2.1, and as such all of the states are assumed to have a positive parity. As discussed in Sec. 2.1.3 the parity restriction limits the possible electromagnetic transitions of any consequence to  $E2$  and  $M1$  transitions.

There are a few techniques that can be used in conjunction with the observed spectrum to determine the appropriate energy level schemes. The first, and most obvious, is to perform particle- $\gamma$ - $\gamma$  coincident measurements. This is done by creating additional logic gates around the photopeaks in the  $\gamma$ -ray energy spectrum and creating additional spectra that represent additional  $\gamma$ -rays observed in coincidence with a reaction residue particle and a  $\gamma$ -ray in the photopeak's region. Separate particle- $\gamma$ - $\gamma$  coincidence gates must be created for each observed photopeak. As shown in Fig. 3.26, the single photon detection efficiency of SeGA in the region of interest can be lower than 2%, therefore the efficiency of detecting two photons simultaneously is much lower and requires better statistical data for particle- $\gamma$ - $\gamma$  measurements than what is necessary for particle- $\gamma$  measurements.

In the absence of reliable particle- $\gamma$ - $\gamma$  coincidence data, the relative photopeak intensities can provide some insight into the decay schemes. Logically, the photopeak intensity of an excited state being fed from a higher energy state must have an intensity equal to or greater than the feeding state's intensity. It is also possible to observe  $\gamma$ -ray decays from states not directly populated in the reaction. A strong indicator of this is the observation of multiple  $\gamma$ -rays with very similar photopeak intensities. This can be explained as cascading decays from a reaction populated state into another excited state that is not directly populated in the reaction.

Another helpful technique is to determine the orbital angular momentum value associated with each photopeak from the momentum distributions as described in Sec. 2.2.1 and Sec. 3.2.2.2. The residual particle's momentum distribution associated with a specific  $\gamma$ -ray allows the identification of the orbital angular momentum value  $\ell$  of the removed nucleon. The momentum distributions only provide a method to distinguish between  $\gamma$ -rays emitted from different nucleon knockout  $\ell$  values.

The experimental results are compared to other experimental results and theoretical calculations when applicable to affirm and clarify the accuracy of the determined level schemes and measurements. The total comprehension of the reaction residue's level scheme is enhanced by any previous experimental results that are available. The known structure

and transition strengths of the residue’s isospin mirror are also a good comparison tool. Isospin mirror symmetry provides a rough picture of the angular momentum values and energy separations to be expected of the bound states in the residue. The spectroscopic values of the single proton removal from the isospin mirrors also give some expectations of the relative spectroscopic strengths of the neutron removal reaction. Finally, *USDA* and *USDB* shell-model calculations as described in Sec. 2.1.1.1, provide theoretical estimates of the excitation energies, total angular momentum values, and the population probabilities of the reaction residue’s bound states. Shell-model calculations are also implemented to provide rough estimates of the electromagnetic transition strengths between the residue’s bound states.

#### 4.1.2.2 Partial State Cross Sections

The  $\gamma$ -ray emission rate ( $N_\gamma$ ) is determined in a similar way to that of the fragmentation reaction rate  $N_f$  in Eq. 4.3 and Sec. 4.1.1.2. Each detected  $\gamma$ -ray event corresponds to a COINC trigger event as described in Sec. 3.4. The COINC trigger was not downscaled, so the factor  $\lambda_{DS}$  is not included in any calculations. Because of the particle- $\gamma$  coincidence required for the COINC triggered events, the  $\gamma$ -ray emission rate is dependent on the particle detection efficiency ( $\varepsilon_f$ ) and the  $\gamma$ -ray detection efficiency ( $\varepsilon_\gamma$ ). The calculation of the  $\gamma$ -ray emission rate is

$$N_\gamma = \frac{N_\gamma^{\text{obs}}}{N_{\text{norm}}\tau_\gamma\varepsilon_f\varepsilon_\gamma}, \quad (4.6)$$

where  $\tau_\gamma$  is the COINC trigger live-time correction,  $N_\gamma^{\text{obs}}$  is the number of observed photopeak events, and  $N_{\text{norm}}$  is the normalization factor. The normalization factor  $N_{\text{norm}}$  is the total raw scalar output of the OBJ scintillator summed over all of the fragmentation runs.  $\tau_\gamma$  is calculated from Eq. 3.21 for the COINC trigger condition, and the particle detection efficiency is taken as the weighted average of  $\varepsilon_f$  from all of the fragmentation runs for a specific reaction as described in Sec. 4.1.1.2.

As discussed in Sec. 3.3.3, GEANT simulation software is used to recreate the  $\gamma$ -rays emitted from the relativistic fragment residue. A separate simulation is run for each photopeak in the energy spectrum. Each simulation is run for  $10^6$  single photon events emitted in all directions with the exact energy of the measured photopeak’s centroid and then Lorentz boosted into the lab frame. The simulation is adjusted to reasonably account for

the distribution of emission velocities within the target. The resulting simulated detected energy spectrum is then Doppler reconstructed into the emission frame according to the same procedure used for the actual energy spectrum as described in Sec. 3.3.1. The simulated photopeak is the expected actual photopeak for  $10^6$   $\gamma$ -ray emissions plus the 6% underestimation factor of the simulated photopeak detection efficiency as discussed in Sec. 3.3.3.

A portion of the observed  $\gamma$ -ray energy spectrum is fit by a function ( $f(E)$ ) that is a summation of the simulated photopeaks ( $\xi_i(E)$ ) each multiplied by its own scale factor ( $\alpha_i$ ) added to a pair of free parameter exponential functions to account for background noise in the spectrum. The fitted equation has the form of

$$f(E) = a_0 e^{a_1 E} + a_2 e^{a_3 E} + \sum_i \alpha_i \xi_i(E), \quad (4.7)$$

where  $a_{0-3}$ , and  $\alpha_i$  are free parameters and  $i$  is summed over all simulated photopeaks. The fitted value of  $\alpha_i$  is then scaled by the number of simulated events for that photopeak ( $10^6$ ) and the simulation correction factor of 6% to give the efficiency corrected total number of photon emissions for that photopeak. The photon efficiency corrected number of photon events ( $N_\gamma/\varepsilon_\gamma$ ) in Eq. 4.6 is determined directly from the simulation results.

Comparing the  $\gamma$ -ray emission rate  $N_\gamma$  to the fragmentation rate  $N_f$ , the  $\gamma$ -ray intensity ( $I_\gamma$ ) is the probability per fragmentation reaction of observing a specific  $\gamma$ -ray calculated as

$$I_\gamma = \frac{N_\gamma}{N_f}, \quad (4.8)$$

where the fragmentation reaction rate is the weighted average  $N_f$  from all of the fragmentation data runs. The reaction branching ratio  $b_i$  from Eq. 4.2 for each observed excited state is determined directly from the associated  $\gamma$ -ray intensities as

$$b_i = \sum_i I_{\gamma i} - \sum_j I_{\gamma j}^{\text{feed}}, \quad (4.9)$$

where  $I_{\gamma i}$  is summed over all observed decay branches from the state and  $I_{\gamma j}^{\text{feed}}$  is summed over all de-excitation branches feeding directly into the state. The direct excited state cross sections are calculated from Eq. 4.2. The ground state does not have any associated  $\gamma$ -ray emission tag like the excited states, so the partial cross section to populate the ground state of the fragmentation residue directly in the reaction is

$$\sigma_{\text{GS}} = \sigma_{\text{inc}} - \sum_i \sigma_i^{\text{partial}}, \quad (4.10)$$

where  $\sigma_i^{\text{partial}}$  is summed over all observed excited state cross sections and is subtracted from the total inclusive cross section  $\sigma_{inc}$ .

### 4.1.3 Longitudinal Momentum Distribution

The longitudinal momentum distributions are described in Sec. 2.2 and Sec. 3.2.2.2 and are used primarily to determine the orbital angular momentum value of the removed nucleon. They can also be used as an impromptu test for any noticeable deviations from the approximations used in the reaction theory. The experimental inclusive momentum distribution is determined as described in Sec. 3.2.2.2. The momentum distributions associated with specific excited states are a little more complicated to acquire. The observed Doppler-reconstructed photopeaks are used to tag the momentum distribution for a given excited state by creating a software coincidence logic gate around the photopeak.

The photopeak gated momentum distribution is still not a good representation of the excited state's momentum distribution, the photopeak gate can contain a large amount of background noise and the Compton tail from other photopeaks which causes the gated momentum distribution to be contaminated by other states. To correct for this background noise, a coincidence logic gate is on the pure background located at energies above any photopeaks. The momentum distribution obtained in coincidence with the background gate is taken as the momentum distribution associated with the background noise for all energies. The momentum distribution corrections for the excited states must be dealt with starting with the highest energy photopeak and making corrections sequentially in decreasing order of photopeak energy. Utilizing Eq. 4.7, the fitted function is decomposed into individual peak components for each GEANT simulated photopeak and a single background component. The integral of each component across the photopeak gate is used to normalize the associated momentum distributions to their respective component of the total photopeak gated momentum distribution. For the highest energy photopeak, the total gated momentum distribution only needs the background component subtracted to determine the pure excited state momentum distribution.

Once the pure momentum distribution of the first photopeak (highest energy) is acquired, the procedure is repeated for the next photopeak's total gated momentum distribution. The second photopeak's total gated momentum distribution contains contaminant components of the background noise and also of the first photopeak's pure momentum distribution.

Using the fitted component integrals of Eq. 4.7 over the second photopeak’s gate limits, the pure background momentum distribution and the first photopeak’s pure momentum distribution are respectively normalized and subtracted from the second photopeak’s total gated momentum distribution, resulting in the second photopeak’s pure momentum distribution. This procedure is repeated for all subsequent photopeaks, taking into consideration all contaminate photopeak counts in each  $\gamma$ -ray energy gate. The momentum distribution of the ground state can be determined by normalizing the pure excited state momentum distributions with their respective branching ratios and subtracting the normalized distributions from the inclusive momentum distribution, however this is not completely necessary if the inclusive cross section is dominated by the ground state cross section in which case the ground state momentum distribution can be approximated by the inclusive distribution.

Theoretical momentum distributions are created for each bound state as described in Sec. 2.2.1.1. The theoretical momentum distributions must be convoluted with the momentum distribution of the projectile beam nuclei to account for the beam’s inherent momentum dispersion. The convoluted momentum distributions are then compared to the experimentally determined momentum distributions where it is possible.

## 4.2 Analysis of ${}^9\text{Be}({}^{26}\text{Si}, {}^{25}\text{Si}+\gamma)$

The  ${}^{26}\text{Si}\rightarrow{}^{25}\text{Si}$  single neutron knockout reaction experiment marks the first time  $\gamma$ -ray spectroscopy has been performed on  ${}^{25}\text{Si}$  and the second time that excited state structural measurements have been made on the isotope. The reaction  ${}^{28}\text{Si}({}^3\text{He}, {}^6\text{He}){}^{25}\text{Si}$  was studied by Ref. [51] in 1971 and that study only focused on measuring the excited state energy levels of  ${}^{25}\text{Si}$ . There have also been several studies done of the isospin mirror  ${}^{25}\text{Na}$  collected in Ref. [52], that are used to help determine the present level scheme of  ${}^{25}\text{Si}$ . The energy levels and angular momentum of the first four lowest bound states from previous studies of  ${}^{25}\text{Si}$  and  ${}^{25}\text{Na}$  are shown in Table 4.1.

The theoretical shell-model calculations from the *USD*, *USDA*, and *USDB* models are in fair agreement with one another, as well as with the experimental  ${}^{25}\text{Si}$  values from previous work and also with the isospin mirror  ${}^{25}\text{Na}$ . A diagram comparing the three shell model calculations has already been presented in Sec. 2.1.1.1 as Fig. 2.6, and the theoretical energy level calculations are given in Table 4.1.

Table 4.1: The energies and angular momentum values of the lowest four observed bound states in  $^{25}\text{Si}$  and  $^{25}\text{Na}$  from previous studies and shell model calculations. The energy values for  $^{25}\text{Si}$  in the second column are taken from the  $^{28}\text{Si}(^3\text{He},^6\text{He})^{25}\text{Si}$  reaction studied in Ref. [51] and the spin assignments for the second column are assumed from the isospin mirror and shell model calculations. The values shown for  $^{25}\text{Na}$  are taken from Ref. [52] and represent the results of several different reaction studies. The shell model calculations are calculated using Ref. [53].

$J\pi$	Energy (keV)				
	$^{25}\text{Si}$	$^{25}\text{Na}$	<i>USD</i>	<i>USDA</i>	<i>USDB</i>
$5/2^+$	0.0	0.0	0.0	0.0	0.0
$3/2^+$	40(5)	89.53(10)	132	181	114
$1/2^+$	815(15)	1069.32(19)	1159	1028	966
$3/2^+$	1963(15)	2202.0(10)	2130	2015	1981

### 4.2.1 Inclusive Reaction Measurements

The  $^{26}\text{Si}$  radioactive isotope beam was created from a primary beam of 150 MeV/nucleon  $^{36}\text{Ar}$  as described in Sec. 3.1. The secondary cocktail beam had a  $^{26}\text{Si}$  beam purity in the focal plane of roughly 12.5%. The particle identification of the secondary cocktail beam is shown in Fig. 4.1.

Two beam normalization runs were performed around the  $^{25}\text{Si}$  fragmentation reaction runs. The calculated values of  $\tau_b$ ,  $\varepsilon_b$ , and  $N_b$  from Sec. 4.1.1.1 for each run are shown in Table 4.2. The weighted average unreacted beam normalization rate  $N_b$  is  $8.94(9) \times 10^{-2}$

Table 4.2: The beam normalization run data for the  $^{26}\text{Si}$  secondary cocktail beam. The live-time correction factor  $\tau_b$ , the total particle detection efficiency  $\varepsilon_b$ , and the beam normalization rate  $N_b$  calculations are described in Sec. 4.1.1.1.

Run #	Live Time $\tau_b$	Efficiency $\varepsilon_b$	Beam Rate $N_b$
182	0.64	0.997	$9.10(13) \times 10^{-2}$
220	0.64	0.996	$8.81(12) \times 10^{-2}$

$^{26}\text{Si}$  particles per raw count in the objective plane scintillator.

The  $^{25}\text{Si}$  fragmentation reaction runs were performed in one consecutive series with a total of 15.75 hours of beam time on target with a PS trigger downscale factor of 20. The

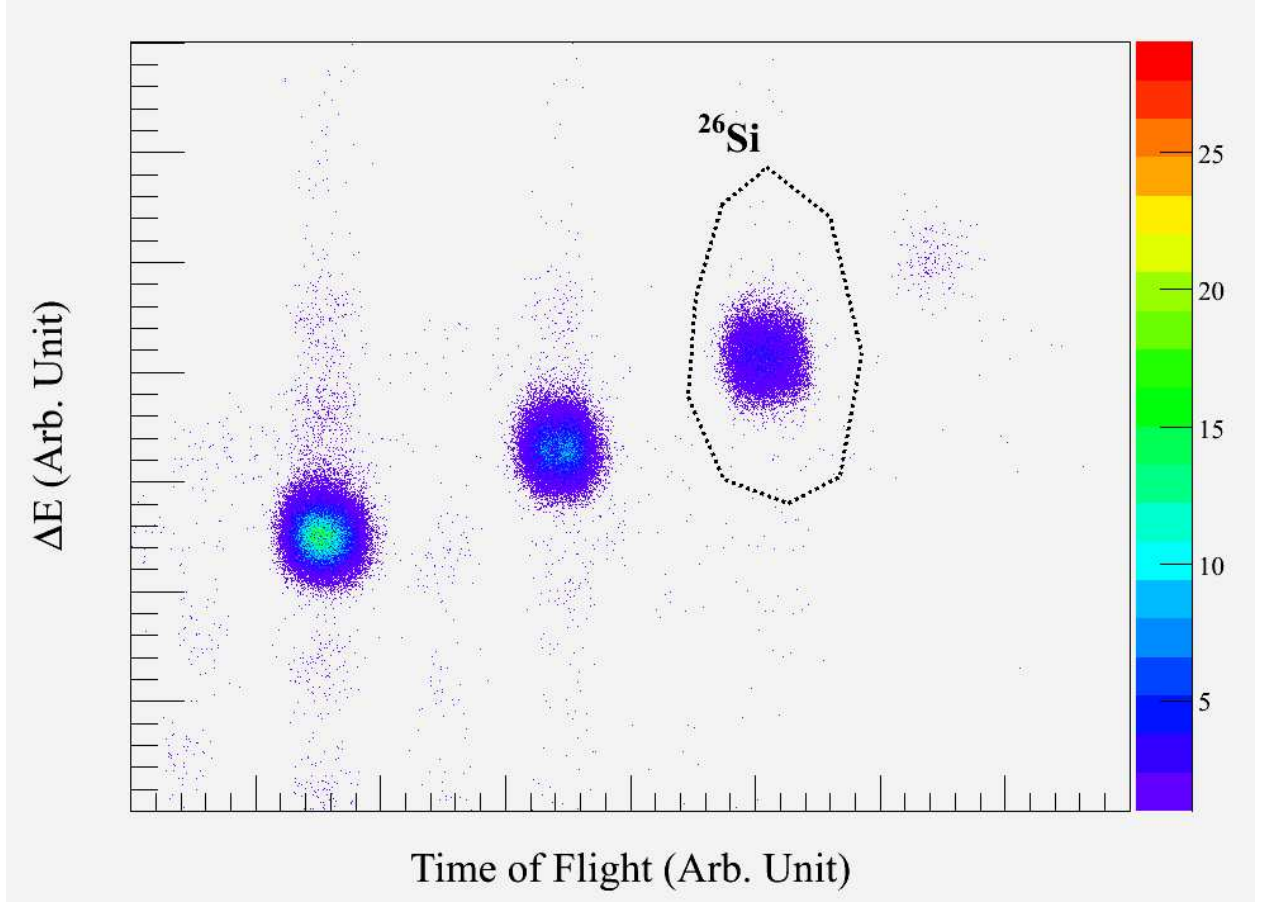


Figure 4.1: The particle identification spectrum of the  $^{26}\text{Si}$  secondary cocktail beam from a beam normalization run. The particle identification logic gate used in the  $^{26}\text{Si}$  beam normalization runs is shown.

particle identification spectrum of the  $^{25}\text{Si}$  fragmentation residues is shown in Fig. 4.2 and the time-of-flight spectrum for the identification of the  $^{26}\text{Si}$  incident particles is shown in Fig. 4.3. The average  $^{26}\text{Si}$  cocktail beam total particle rate per run as measured in the object plane scintillator is shown in Fig. 4.4, with an average per run beam rate for the full data set of  $2.40 \times 10^5$  counts per second.

The CRDC correction factor  $\eta_{crdc} = 1.21(6)$  was determined from the  $d_t$  spectrum as described in Sec. 3.2.4. The particle detection efficiency of the S800 detectors for the  $^{25}\text{Si}$  fragmentation runs is shown in Fig. 4.5, with an average total particle detection efficiency  $\varepsilon_f$  of 36.7(4)%. The live-time correction factors per run for the PS and COINC triggers are shown in Fig. 4.6. The average PS live-time correction factor  $\tau_f$  was 80.26(7)% with the

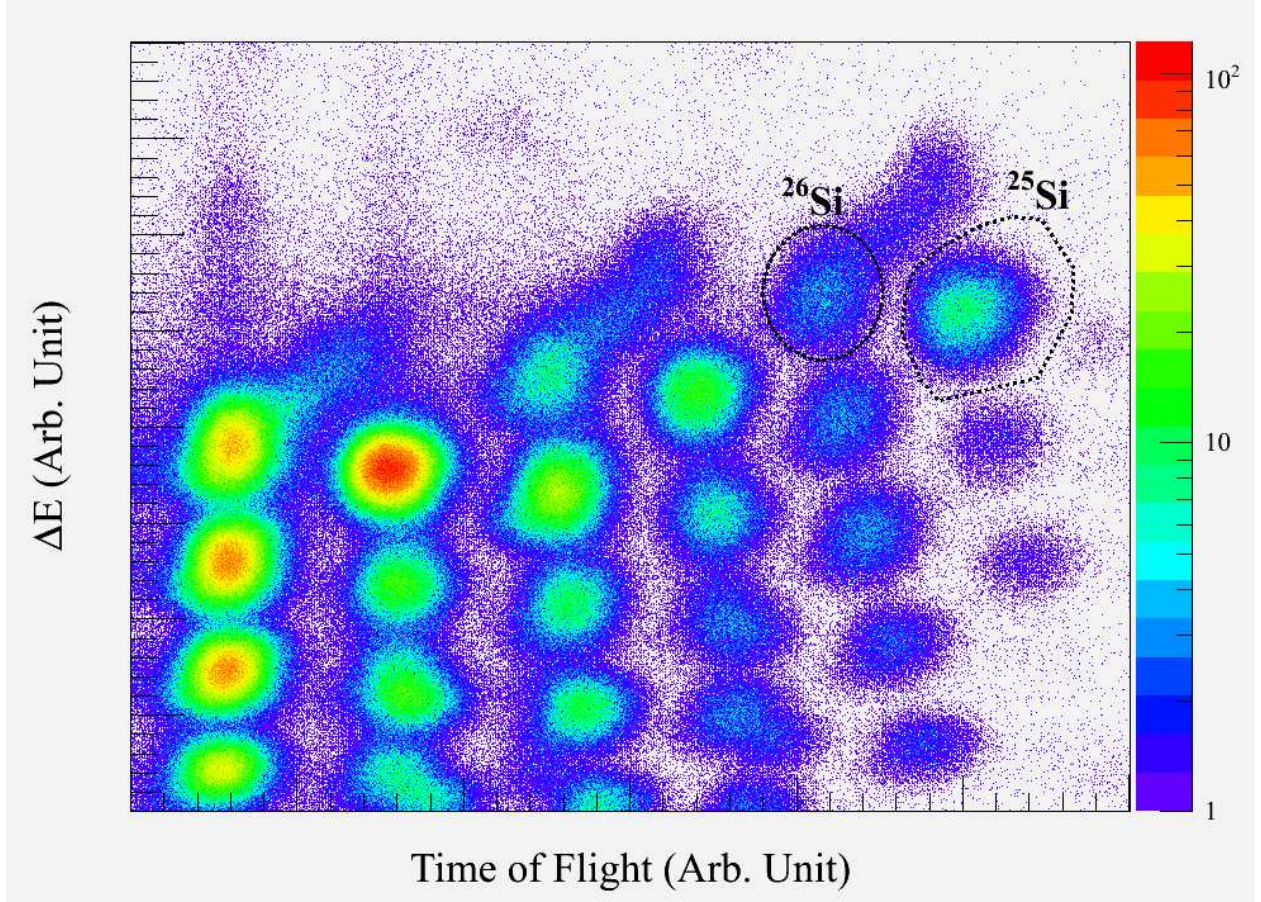


Figure 4.2: The particle identification spectrum of the  $^{25}\text{Si}$  fragmentation reaction data runs. The particle identification logic gate used is shown and labeled. As shown, some of the unreacted  $^{26}\text{Si}$  projectiles still make it into the S800’s focal plane detectors.

average COINC live-time correction factor  $\tau_\gamma$  of 58.39(2)%. The fragmentation reaction rate  $N_f$  per run is plotted in Fig. 4.7, with an error weighted average  $N_f = 5.87(8) \times 10^{-5}$ . Using Eq. 4.1 and the error weighted average values of  $N_b$  and  $N_f$ , the inclusive cross section for the  $^{26}\text{Si} \rightarrow ^{25}\text{Si}$  reaction is determined to be 26.1(3) mb.

#### 4.2.2 $\gamma$ -Ray Analysis

The pre-target  $B\rho$  was set to 2.973 Tm and the post-target  $B\rho$  was set to 2.973 Tm. Using Eq. 3.7, these settings correspond to velocities of  $\beta = 0.458$  for the pre-target  $^{26}\text{Si}$  projectiles and  $\beta = 0.425$  post-target  $^{25}\text{Si}$  projectile-like fragmentation residues. The  $^{26}\text{Si} \rightarrow ^{25}\text{Si}$  reaction was determined to have an optimal mid-target velocity of 44.6% of the speed of light for the  $\gamma$ -

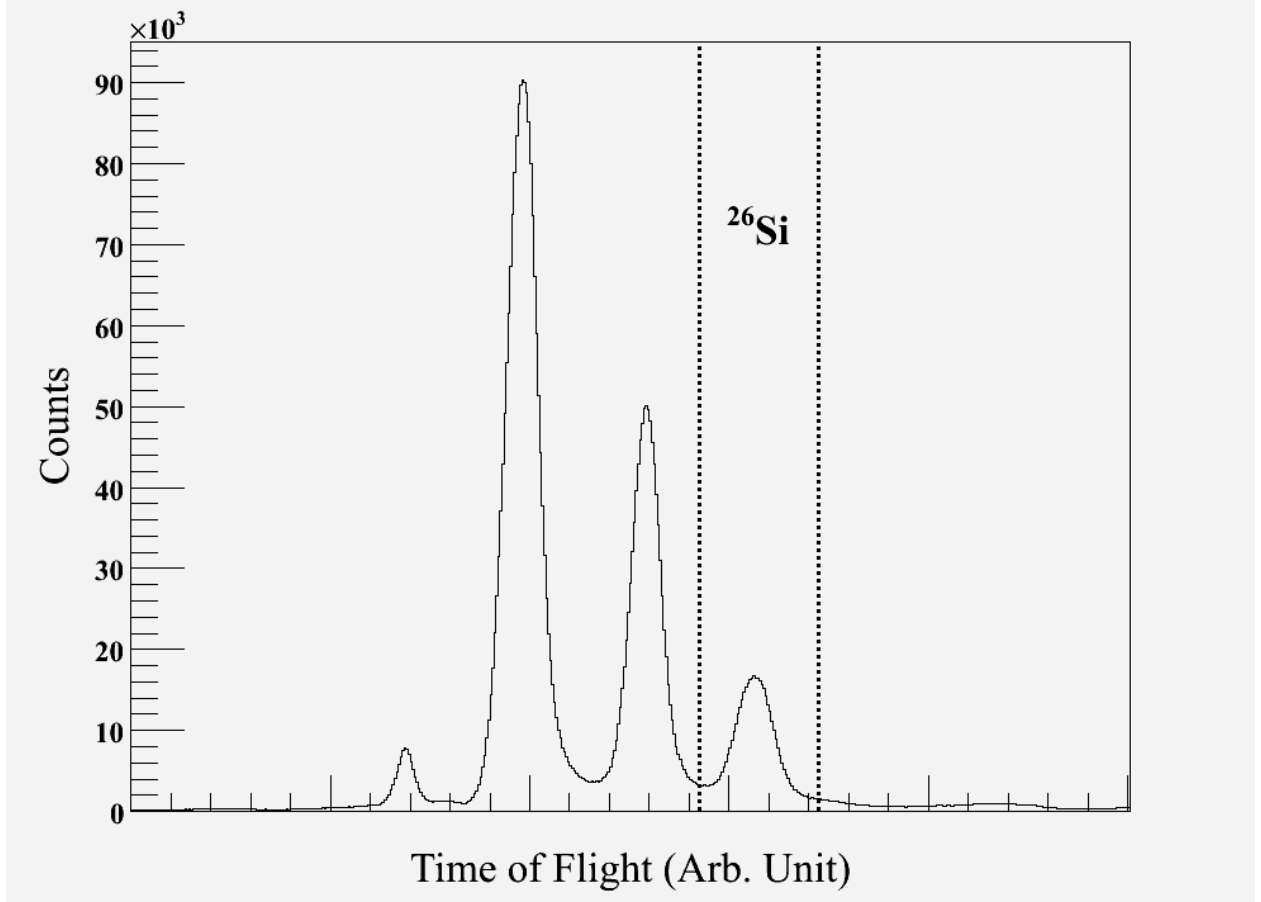


Figure 4.3: The time-of-flight difference spectrum between the extended focal plane and the object plane scintillators for the  $^{26}\text{Si}$  cocktail beam from the fragmentation data runs. There are four large visible peaks, each corresponding to a different isotope in the secondary beam. The  $^{26}\text{Si}$  identification logic gate is shown.

ray energy Doppler reconstruction. The Doppler corrected  $\gamma$ -ray energy spectrum is shown in Fig. 4.8. Two photopeaks are seen with energies of 821(15) keV and 1088(22) keV. GEANT simulations were created for the 821 keV and 1088 keV photopeak detection efficiencies. The simulations were fit to the data as shown in Fig. 4.9 and described in Sec. 4.1.2.2. The 821 keV photopeak had a measured emission rate of  $N_\gamma(821\text{keV}) = 1.15(5) \times 10^{-5}$  which corresponds to a  $\gamma$ -ray intensity from Eq. 4.8 of  $I_\gamma(821\text{keV}) = 0.196(9)$ . The 1088 keV photopeak was found to have  $N_\gamma(1088\text{keV}) = 2.37(3) \times 10^{-5}$  and  $I_\gamma(1088\text{keV}) = 0.040(6)$ .

Unfortunately the statistics were too low to perform particle- $\gamma$ - $\gamma$  coincidence measurements and the parallel momentum distributions for the populated excited states were

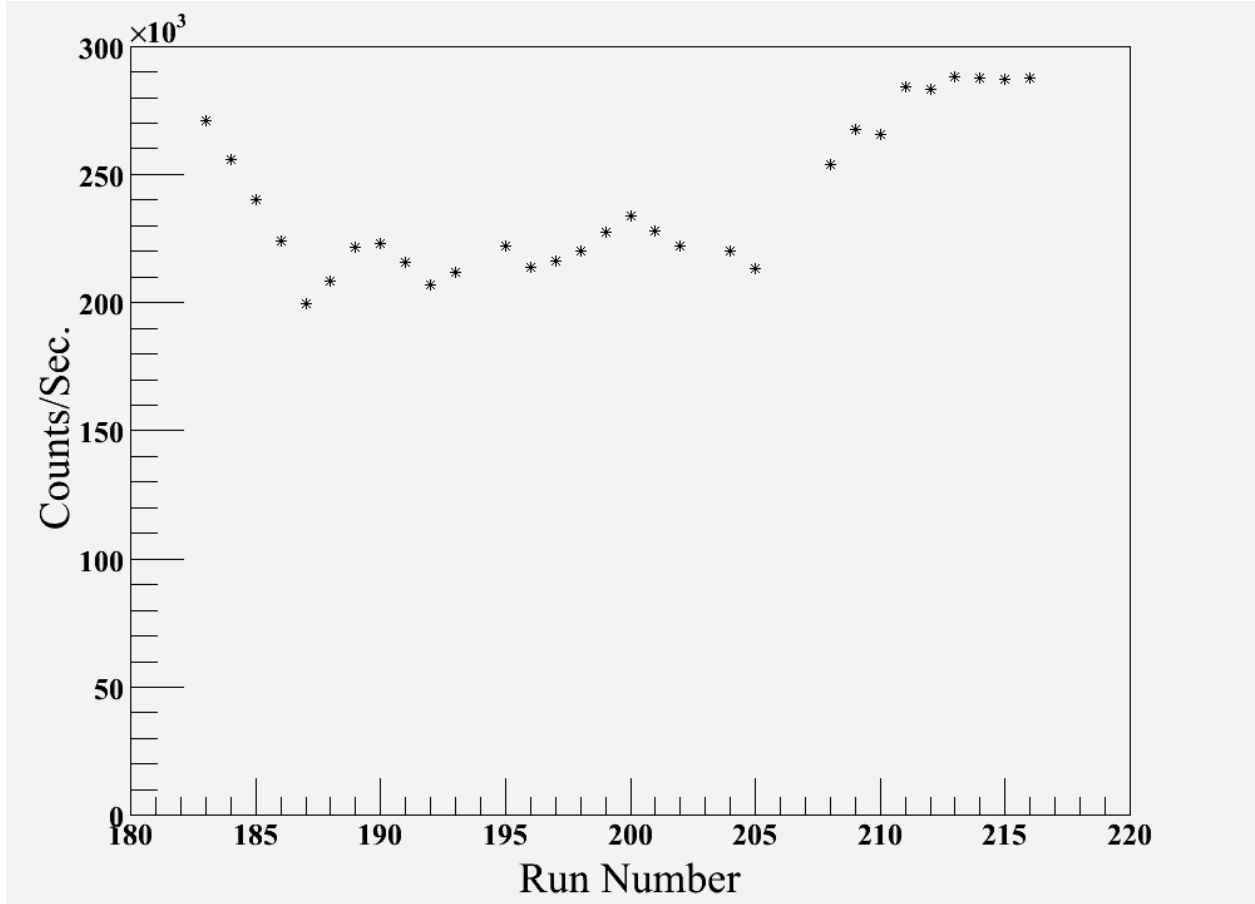


Figure 4.4: The average per run total beam rate measured in the object plane (OBJ) scintillator per run from the  $^{26}\text{Si} \rightarrow ^{25}\text{Si}$  fragmentation reaction data runs. The data is taken for all particles in the secondary beam passing through the object plane scintillator.

compromised too much by the damaged CRDC section to make reliable comparison's with theoretical distributions. Comparing the observed photopeaks with the expected values from Table 4.1, three possible decay schemes could be constructed, one in which the 1088 keV  $\gamma$ -ray feeds into the 821 keV state, another in which the 1088 keV and the 821 keV state are both de-excitation branches from the same state at 1088 keV, and the third being that the 821 keV and 1088 keV are distinct and separate decays from two different excited states. If the 821 keV and the 1088 keV  $\gamma$ -rays were both decaying from an excited state at 1088 keV, then the 821 keV  $\gamma$ -ray would have to decay into a state at 267 keV. If this were the case, there should be a  $\gamma$ -ray emitted from the 267 keV state's de-excitation to the ground state, and the corresponding photopeak should have an intensity at least equal to if not

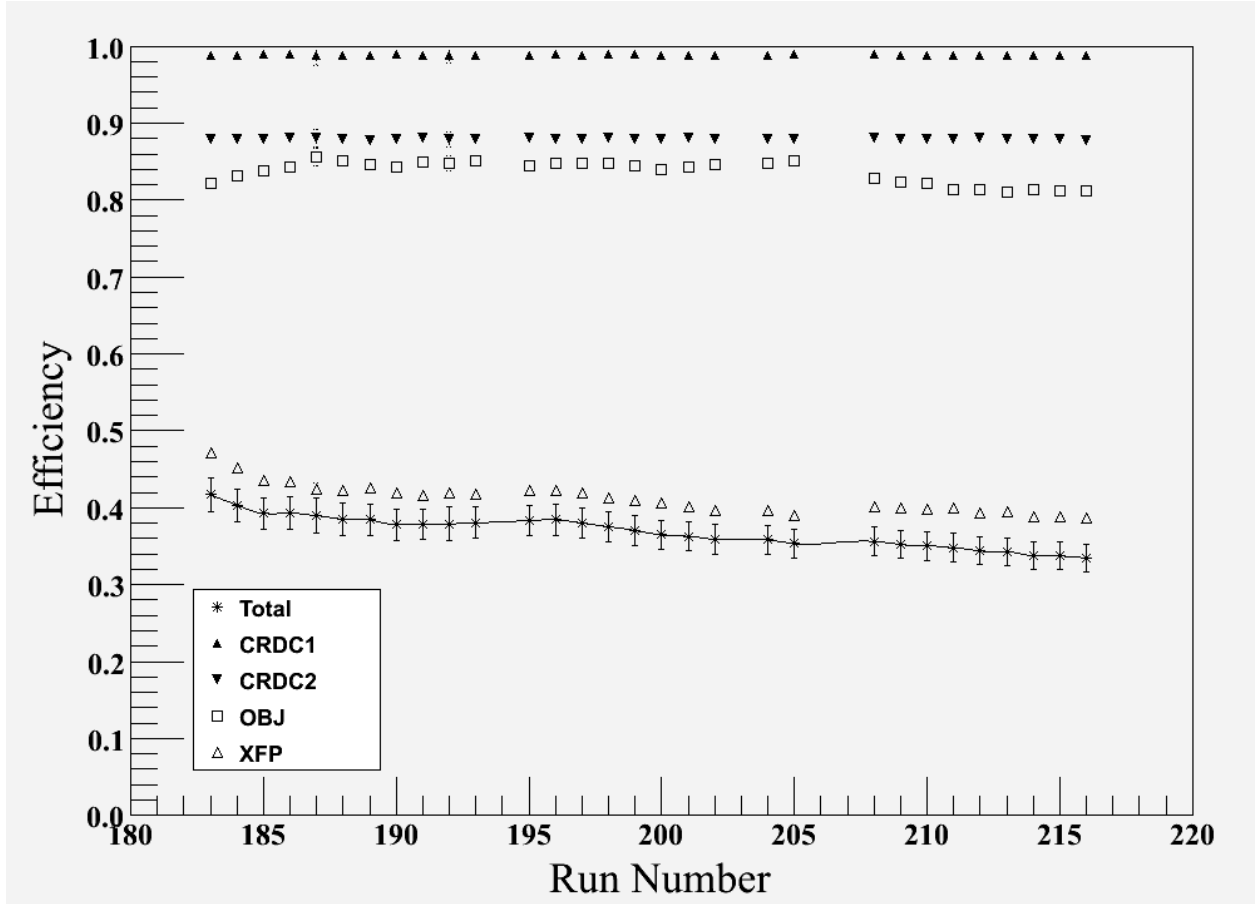


Figure 4.5: The particle detection efficiency values for each run used in the  $^{26}\text{Si} \rightarrow ^{25}\text{Si}$  fragmentation data set. The individual detector efficiencies are shown, along with the total detection efficiency. The total detection efficiency includes the CRDC correction factor  $\eta_{crdc}$ . Note that the horizontal axis is scaled by run number, not the total elapsed beam time for each run.

greater than 821 keV photopeak intensity. A photopeak simulation was created for the hypothetical 267 keV  $\gamma$ -ray, and it is shown in Fig. 4.10 that this scenario of the 1088 keV and 821 keV  $\gamma$ -rays being emitted from the same initial state is incorrect since the 821 keV to 267 keV  $\gamma$ -ray cascade would create a very large 267 keV photopeak that the experimental data does not corroborate. Of the other possible level schemes that can be constructed, the scenario in which the 1088 keV  $\gamma$ -ray is feeding into the 821 keV excited state from a higher energy state at 1909 keV provides a better agreement with the excited state energy levels previously measured for  $^{25}\text{Si}$  in Ref. [51] and also is in a better agreement with the

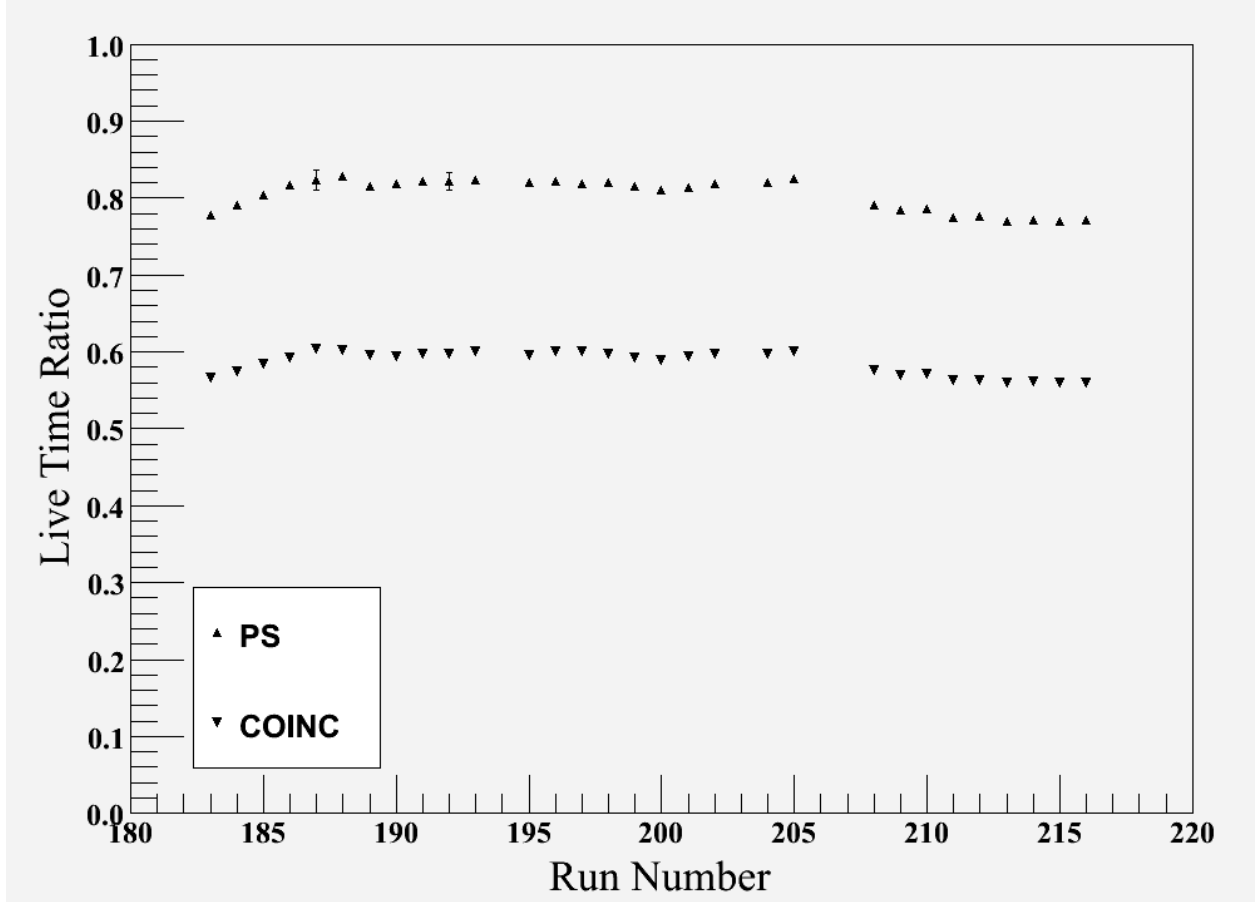


Figure 4.6: The PS and COINC trigger live-time corrections for each run used in the  $^{26}\text{Si} \rightarrow ^{25}\text{Si}$  fragmentation data set. Note that the horizontal axis is scaled by run number, not the elapsed beam time for each run.

shell-model calculations and the isospin mirror scheme. Fig. 4.10 also shows the photopeak simulation results for a 1909 keV  $\gamma$ -ray emission from  $^{25}\text{Si}$ . The simulated 1909 keV  $\gamma$ -ray emissions is scaled to the same intensity as the 1088 keV photopeak. Because there is no obvious photopeak in the experimental  $\gamma$ -ray energy spectrum around 1909 keV, it must be assumed that the intensity of this  $\gamma$ -ray must be too small for it to appear in the current data set. Judging from the results of the simulation, it can safely be said that the electromagnetic transition of the 1909 keV state to the ground state or the low lying 40 keV state must have a smaller or at most equal branching rate to that of the 1088 keV decay branch. The very low 40 keV energy state reported by Ref. [51] is below the SeGA energy threshold in this experimental set-up, so there is no way to make any measurements on this low lying excited

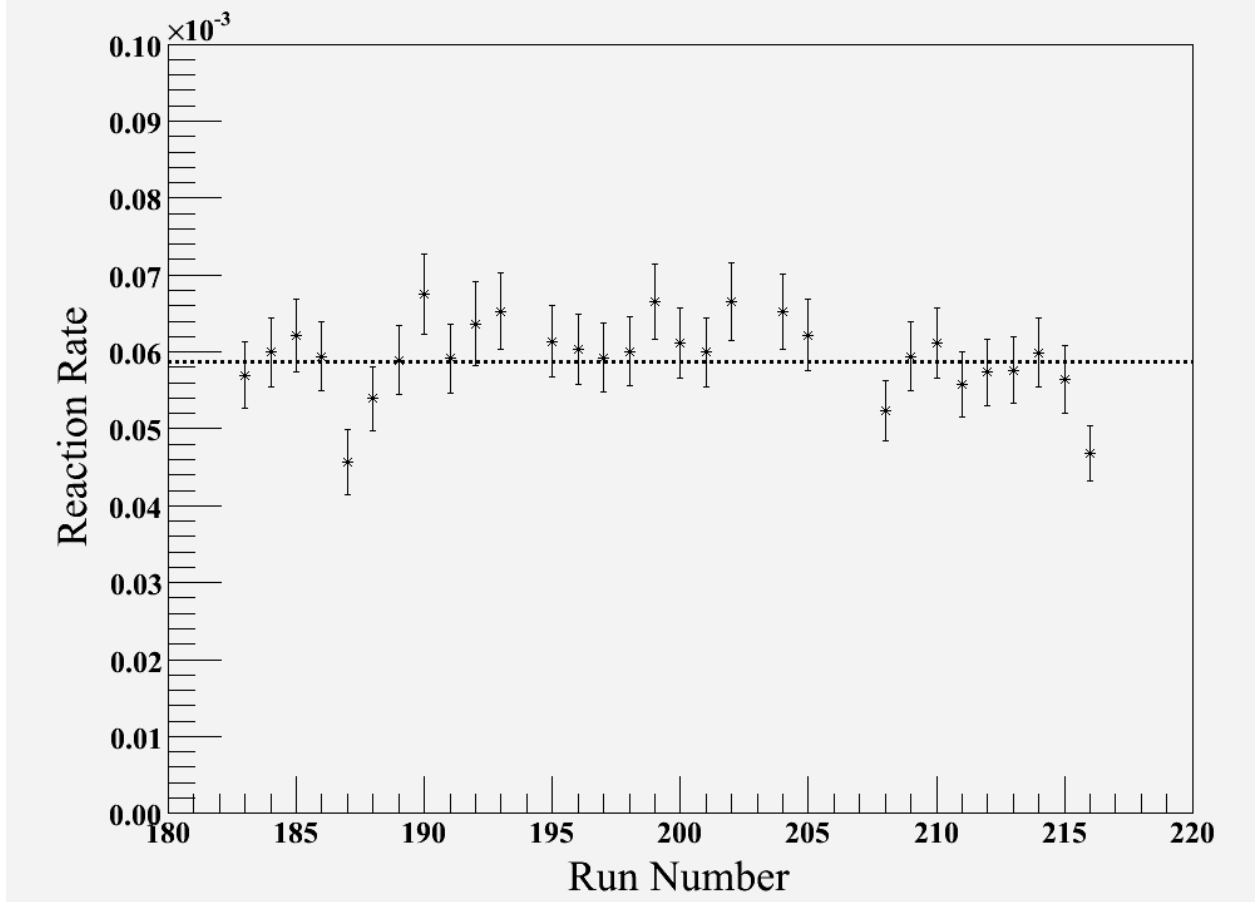


Figure 4.7: The fragmentation reaction rate for each run used in the  $^{26}\text{Si} \rightarrow ^{25}\text{Si}$  data set. Note that the horizontal axis is scaled by the run number, not the elapsed beam time for each run. A horizontal line is drawn for error weighted average of all of the data points at  $N_f = 5.87 \times 10^{-5}$ .

state. The 821 keV state is assumed to decay directly to the ground state because of the agreement this would have with the 815 keV level reported by Ref. [51]. There is also some evidence for this from the isospin mirror  $^{25}\text{Na}$ , in which the decay from the 1069 keV  $1/2^+$  state to the 89 keV  $3/2^+$  state is an order of magnitude more likely than the decay to the  $5/2^+$  ground state, which is indicative of an  $M1$  dominated electromagnetic transition. Since the decay branching is  $M1$  dominated in the isospin mirror, it is logical to assume that the  $E2$  transition will dominate the  $M1$  transition in  $^{25}\text{Na}$ 's mirror  $^{25}\text{Si}$ . This decay scheme is also in good agreement with the theoretical *USDB* electromagnetic transition calculations from Table 2.4.

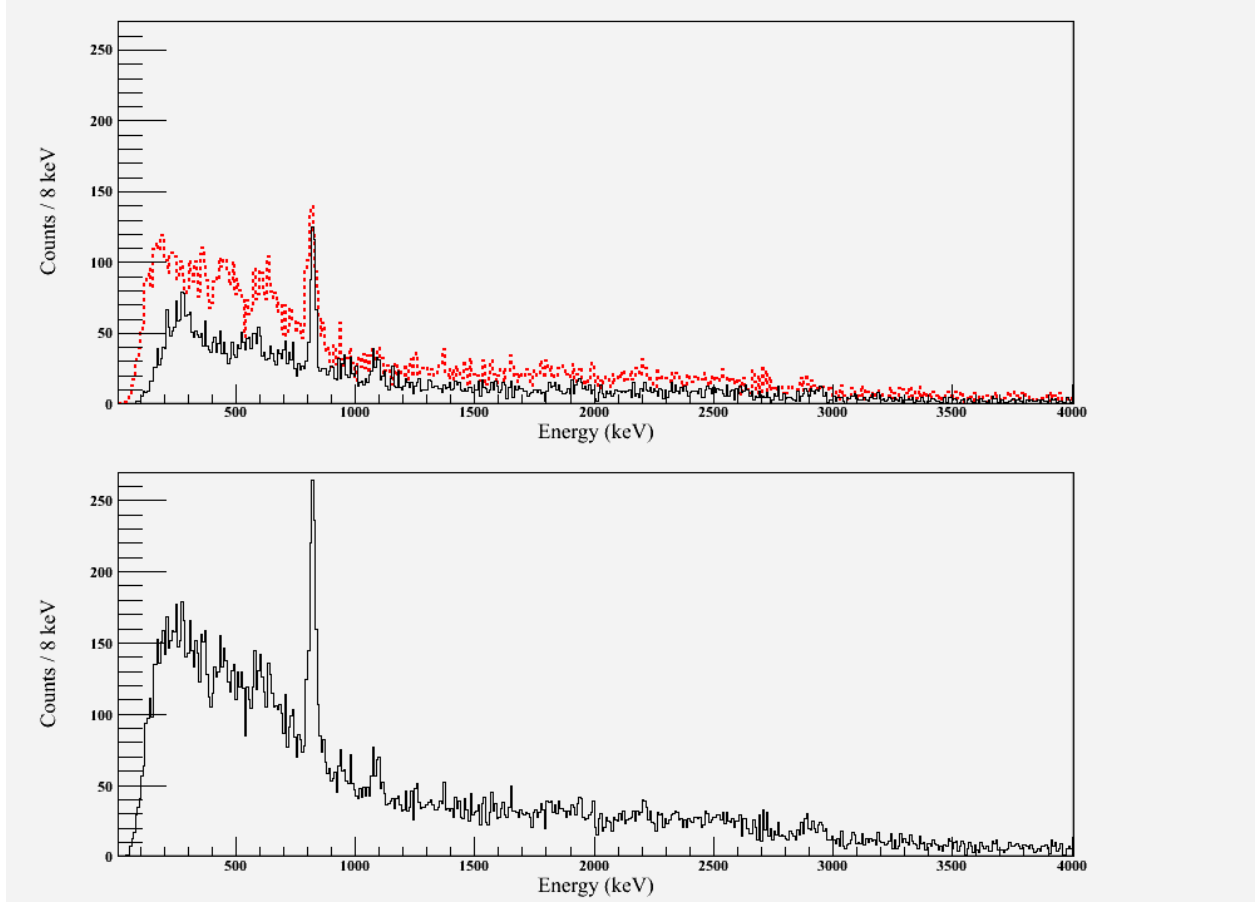


Figure 4.8: The Doppler reconstructed  $\gamma$ -ray energy spectrum of  $^{25}\text{Si}$  collected from all of the  $^{26}\text{Si} \rightarrow ^{25}\text{Si}$  fragmentation reaction data runs. The top figure compares the  $37^\circ$  SeGA detector ring (dashed red line) to the  $90^\circ$  SeGA detector ring (solid black line). The bottom figure shows the summed SeGA  $\gamma$ -ray energy spectrum for  $^{25}\text{Si}$ . The Doppler reconstruction was performed with a velocity of  $\beta = 0.446$ .

Correcting for feeding of the 821 keV excited state from the 1088 keV decay from the 1909 keV state, and approximating that the 1088 keV photo-decay accounts for all of the 1909 keV level's decay strength, the partial cross sections for the direct population of the excited states in  $^{25}\text{Si}$  from the neutron knockout from  $^{26}\text{Si}$  are  $\sigma_{822}^{\text{partial}} = 4.06(61)$  mb and  $\sigma_{1909}^{\text{partial}} = 1.06(21)$  mb. Since no distinction can be made in this experiment between the low lying 40 keV state and the ground state in  $^{25}\text{Si}$ , the calculation of the direct ground state population cross section using Eq. 4.10 is actually the combined cross section to the low lying 40 keV state and the ground state. The direct reaction cross section of the 40 keV

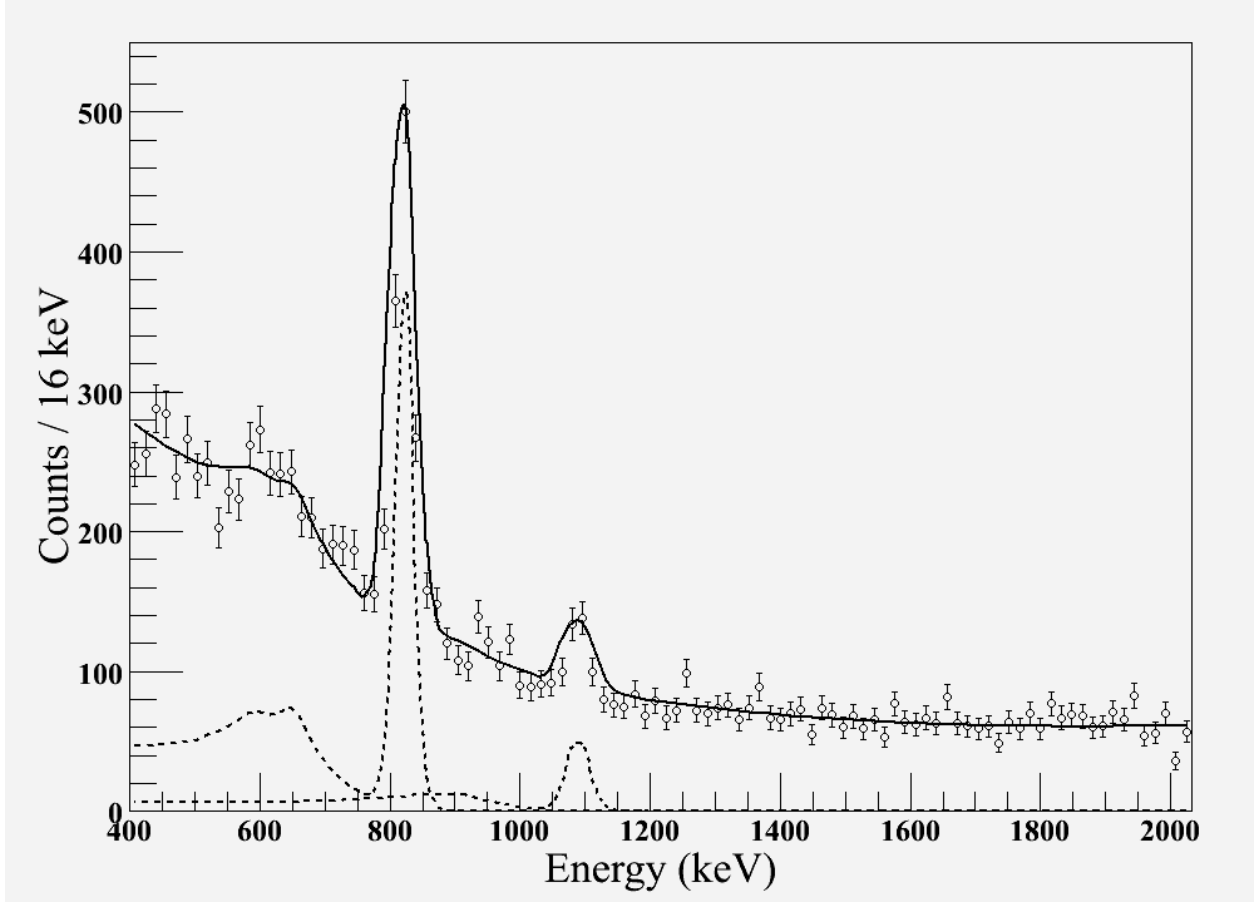


Figure 4.9: The simulated photopeaks (shown as dashed lines) are added to a background noise function as described in Sec. 4.1.2.2 and then fit to the  $^{25}\text{Si}$   $\gamma$ -ray energy spectrum. The fitted function is shown as a solid line.

state and the ground state is  $\sigma_{\text{GS}+40} = 21.0(35)$  mb, however the contributions from the 40 keV state's reaction channel should only be a small fraction of the ground state's reaction channel. A level scheme diagram of  $^{25}\text{Si}$  along with appropriate experimental and theoretical comparisons is provided in Fig. 4.11.

### 4.2.3 Longitudinal Momentum Distributions

The longitudinal momentum distributions are shown in Fig. 4.12, the inclusive  $^{25}\text{Si}$  momentum distribution shows a good agreement with the  $\ell = 2$ ,  $d_{5/2}$  ground state, which should be expected since it is a very dominant reaction channel. There was not enough quality data to make any positive identification of the orbital angular momentum values for any of the

excited states from their pure momentum distributions.

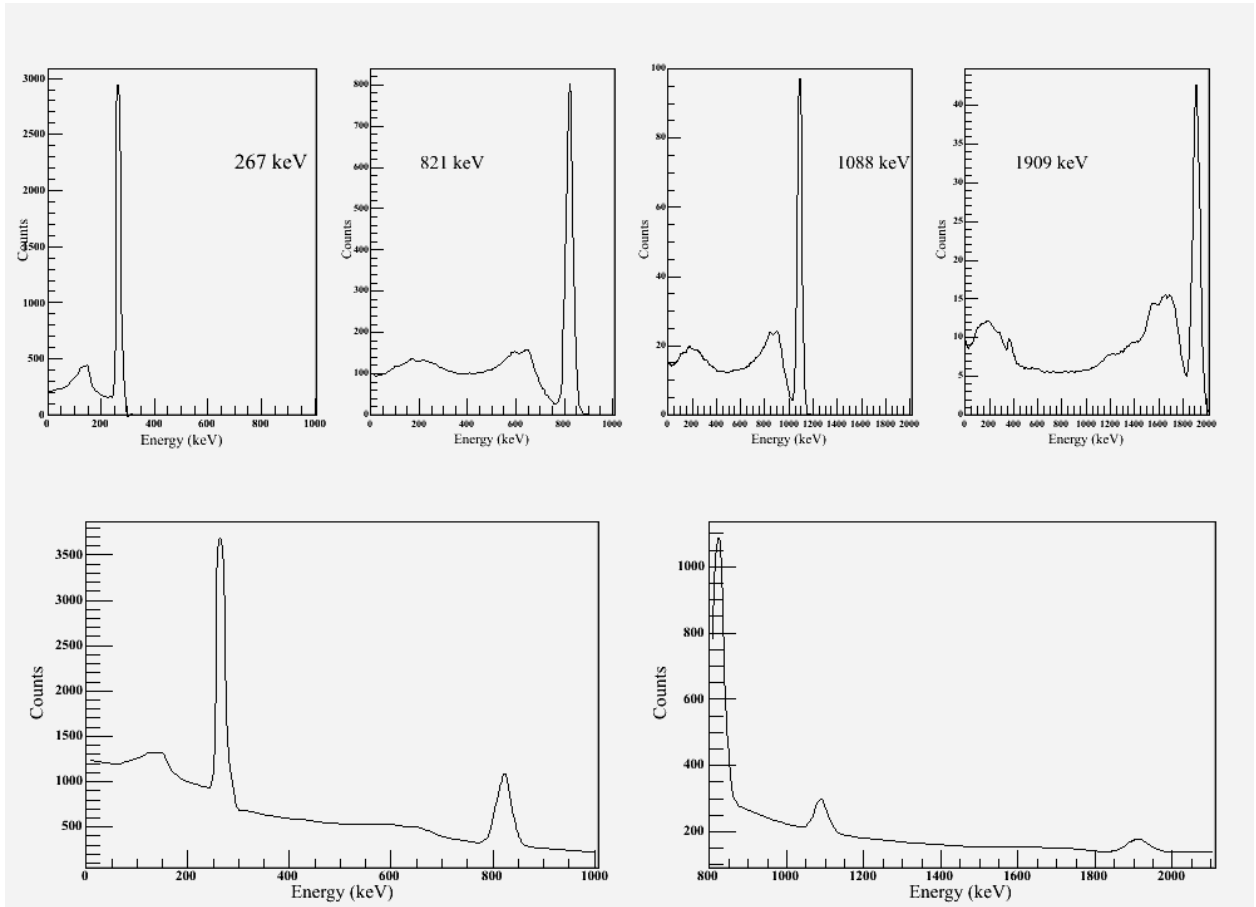


Figure 4.10: The top row shows the photopeak detection simulations for a 267 keV, 821 keV, 1088 keV, and 1909 keV  $\gamma$ -ray emission from the  $^{25}\text{Si}$  fragment residue. The 267 keV simulation is efficiency scaled to the same  $\gamma$ -ray intensity as the 821 keV photopeak, and the 1909 keV simulation is scaled to the same intensity as the 1088 keV photopeak. The bottom two figures show the peaks from the top row added to the background function that was fit to the experimental data. The bottom left figure is focused on the 267 keV and 821 keV photopeaks, while the bottom right figure is focused on the 1088 keV and 1909 keV photopeaks. If the 267 keV photopeak existed it would have easily been observed, because it was not seen in the experimental energy spectrum the possibility of the 1088 keV and 821 keV  $\gamma$ -rays decaying from an excited state at 1088 keV can be ruled out. The 1909 keV photopeak would have been just barely observable at an equal intensity to the 1088 keV photopeak, because the 1909 keV photopeak was not observed in the experimental energy spectrum, it is safe to assume that the decay branch of the 1909 keV excited state directly to the ground state is less than or at most equal to the decay branch to the 821 keV excited state via the 1088 keV  $\gamma$ -ray.

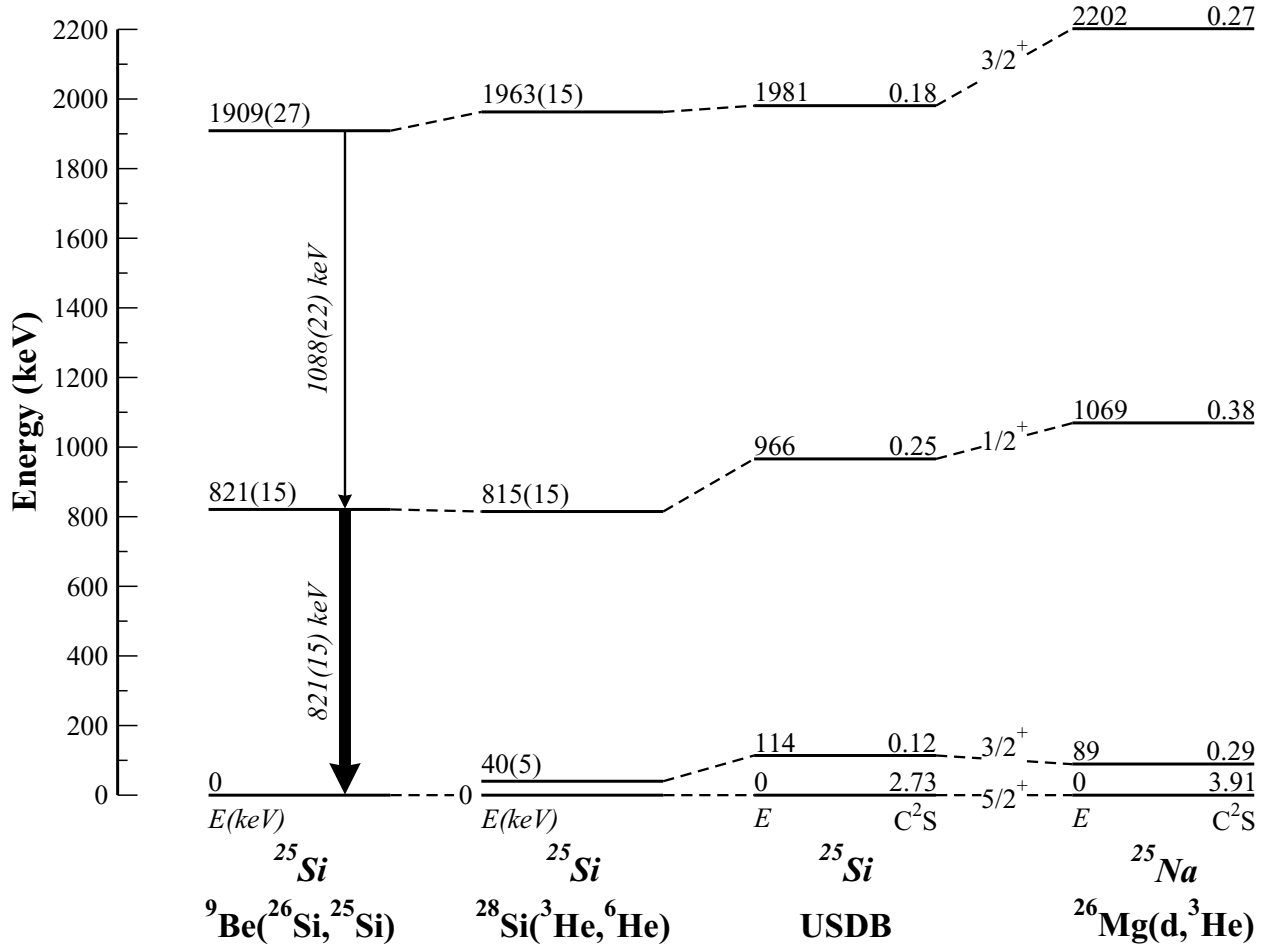


Figure 4.11: Four level diagrams are presented. From left to right:  $^{25}\text{Si}$  from the present work;  $^{25}\text{Si}$  from the previous work in Ref. [51];  $^{25}\text{Si}$  from the *USDB* shell-model calculations; and the isospin mirror  $^{25}\text{Na}$  from experimental evidence collected in Ref. [52]. The spectroscopic factor ( $C^2S$ ) for  $^{26}\text{Si} \rightarrow ^{25}\text{Si}$  is shown for each excited state in the *USDB* shell-model calculation and the available  $C^2S$  values from the  $^{26}\text{Mg}(d, ^3\text{He})^{25}\text{Na}$  reaction are given for the  $^{25}\text{Na}$  energy levels. The electromagnetic transitions observed in the present study are also shown.

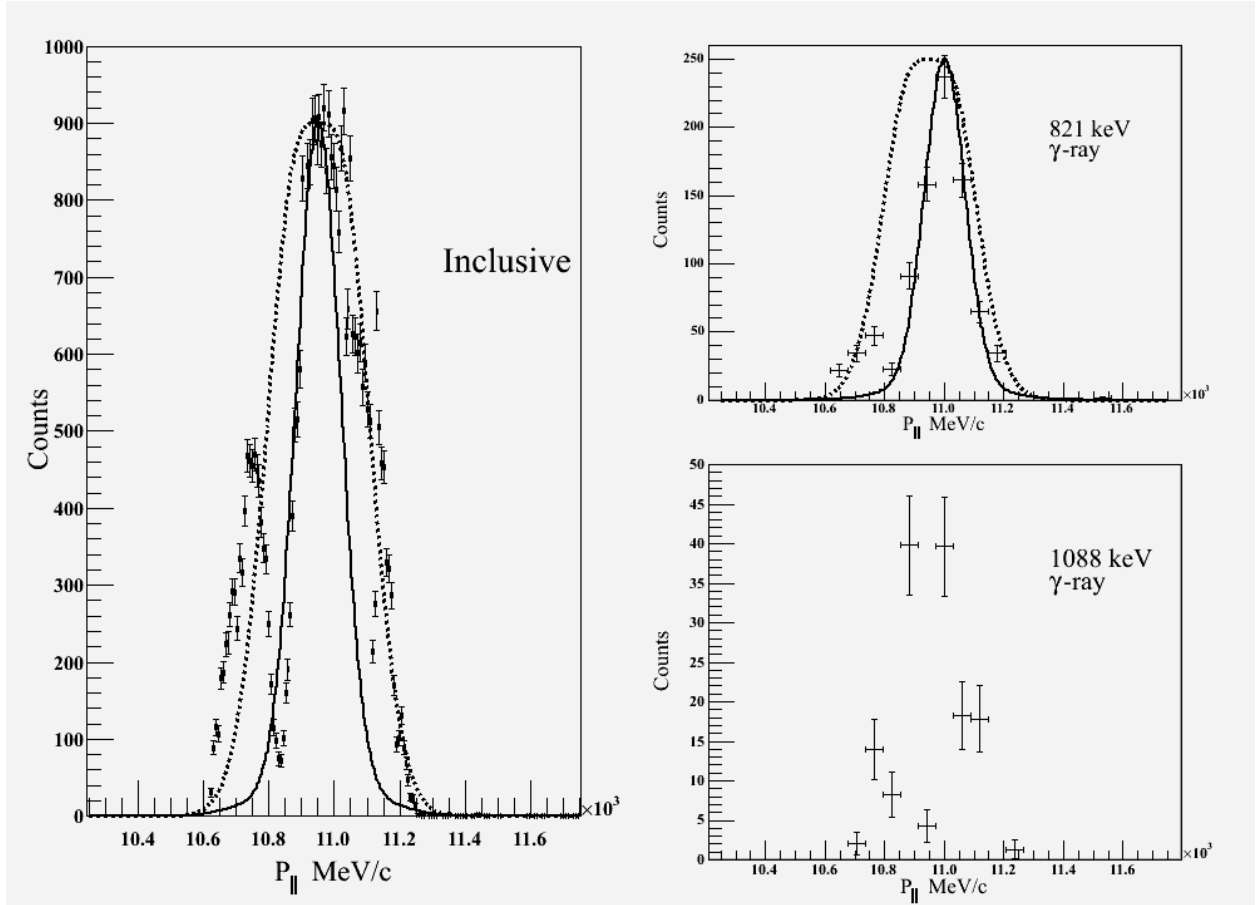


Figure 4.12: The longitudinal momentum distributions of  $^{25}\text{Si}$ . The theoretical momentum distributions are shown as lines for comparison with the experimental momentum distributions. The solid line is for the  $\ell = 0$ ,  $s_{1/2}$  theoretical distribution and the dashed line is for the  $\ell = 2$ ,  $d_{5/2}$  and  $d_{3/2}$  theoretical distribution. The figure on the left hand side is the inclusive momentum distribution, it is in fairly good agreement with the  $\ell = 2$  distribution line, which is expected from the  $d_{5/2}$  ground state dominated reaction cross section. The top right figure is the pure momentum distribution of the 821 keV photopeak, and the bottom right is the pure momentum distribution of the 1088 keV photopeak.

### 4.3 Analysis of ${}^9\text{Be}({}^{30}\text{S}, {}^{29}\text{S}+\gamma)$

The  ${}^{30}\text{S}\rightarrow{}^{29}\text{S}$  single neutron knockout reaction experiment is the first study of  ${}^{29}\text{S}$ 's excited state structural properties. There have been several previous studies done of the isospin mirror  ${}^{29}\text{Al}$  collected in Ref. [54] that were used along with shell-model calculations as comparisons to assist in determining the level scheme of  ${}^{29}\text{S}$  from the single neutron knockout reaction. The first seven lowest energy states and corresponding angular momentum values of  ${}^{29}\text{S}$  from shell-model calculations and  ${}^{29}\text{Al}$  from previous experimental studies are shown in Table 4.3. The level scheme of the isospin mirror  ${}^{29}\text{Al}$  seems to be in fair agreement with

Table 4.3: The energies and angular momentum values of the lowest seven bound states in  ${}^{29}\text{Al}$  from previous studies and  ${}^{29}\text{S}$  from shell model calculations. The values shown for  ${}^{29}\text{Al}$  are taken from Ref. [54] and represent the results of several different reaction studies. The shell model calculations are calculated using Ref. [53].

$J^\pi$	Energy (keV)			
	${}^{29}\text{Al}$	<i>USD</i>	<i>USDA</i>	<i>USDB</i>
$5/2^+$	0.0	0.0	0.0	0.0
$1/2^+$	1398.05(16)	1214	1301	1214
$7/2^+$	1754.28(16)	1799	1854	1858
$3/2^+$	2224.10(19)	1959	2193	2076
$3/2^+$	2865.70(22)	2735	2617	2704
$5/2^+$	3061.81(23)	2801	3091	2993
$5/2^+$	3184.54(18)	3017	3116	3095

the *USD*, *USDA*, and *USDB* shell-model calculations. A diagram comparing the shell-model calculations has been presented as in Sec. 2.1.1.1 as Fig. 2.7.

#### 4.3.1 Inclusive Reaction Measurements

The  ${}^{30}\text{S}$  radioactive isotope beam was created from a primary beam of 150 MeV/nucleon  ${}^{36}\text{Ar}$  as described in Sec. 3.1. The full data set was broken up into two separate smaller data sets. The reason for this was that only a limited amount of beam time for experiment 03021 could be used for each experimental reaction (three two-neutron knockout reactions and two single-neutron knockout reactions). On the last day of beam time for experiment 03021, it was decided to extend the beam time for the  ${}^{30}\text{S}\rightarrow{}^{29}\text{S}$  knockout reaction. In the time between the initial data set and the second data set, the timing signals had been changed

and the extended focal plane scintillator had degraded quit a bit, so the particle detection information of the first and second data set had to be analyzed as separately and the results of each data set averaged together for the final result. It was necessary to perform the  $\gamma$ -ray analysis on the entire data set as a whole, however the calculations for the partial state cross sections are performed separately for each data set and then averaged. The first data set was collected for 8.6 hours of beam time on target on Nov. 25, 2004, with a PS trigger downscale factor of 100. The second data set was collected over 4.4 hours of beam on target on Nov. 30, 2004, with a PS trigger downscale factor of 50. The secondary cocktail beam had a  $^{30}\text{S}$  beam purity in the focal plane of roughly 10.5% for the first data set and 11.7% in the second set. The particle identification of the  $^{30}\text{S}$  secondary cocktail beam for both data sets is shown in Fig. 4.13.

Beam normalization runs were performed around each of the  $^{29}\text{S}$  fragmentation reaction run data sets for a total of three beam normalization runs per reaction data set. The calculated values of  $\tau_b$ ,  $\varepsilon_b$ , and  $N_b$  from Sec. 4.1.1.1 for each run are shown in Table 4.4. The

Table 4.4: The beam normalization run data for the  $^{30}\text{S}$  secondary cocktail beam. The live-time correction factor  $\tau_b$ , the total particle detection efficiency  $\varepsilon_b$ , and the beam normalization rate  $N_b$  calculations are described in Sec. 4.1.1.1. The first three runs were used for the first data set and the last three runs were used for the second data set.

Run #	Live Time $\tau_b$	Efficiency $\varepsilon_b$	Beam Rate $N_b$
72	0.44	0.987	$8.66(18) \times 10^{-2}$
73	0.45	0.988	$8.87(8) \times 10^{-2}$
108	0.87	0.991	$8.91(15) \times 10^{-2}$
287	0.75	0.997	$8.56(14) \times 10^{-2}$
300	0.79	0.996	$7.34(12) \times 10^{-2}$
301	0.78	0.997	$7.66(12) \times 10^{-2}$

weighted average unreacted beam normalization rates  $N_b$  for the first and second data sets respectively are  $8.85(7) \times 10^{-2}$  and  $7.80(7) \times 10^{-2}$   $^{30}\text{S}$  particles per raw count in the objective plane scintillator.

The particle identification spectrum of the  $^{29}\text{S}$  fragmentation residues is shown in Fig. 4.14 and the time-of-flight spectrum for the identification of the  $^{30}\text{S}$  incident particles is shown in Fig. 4.15.

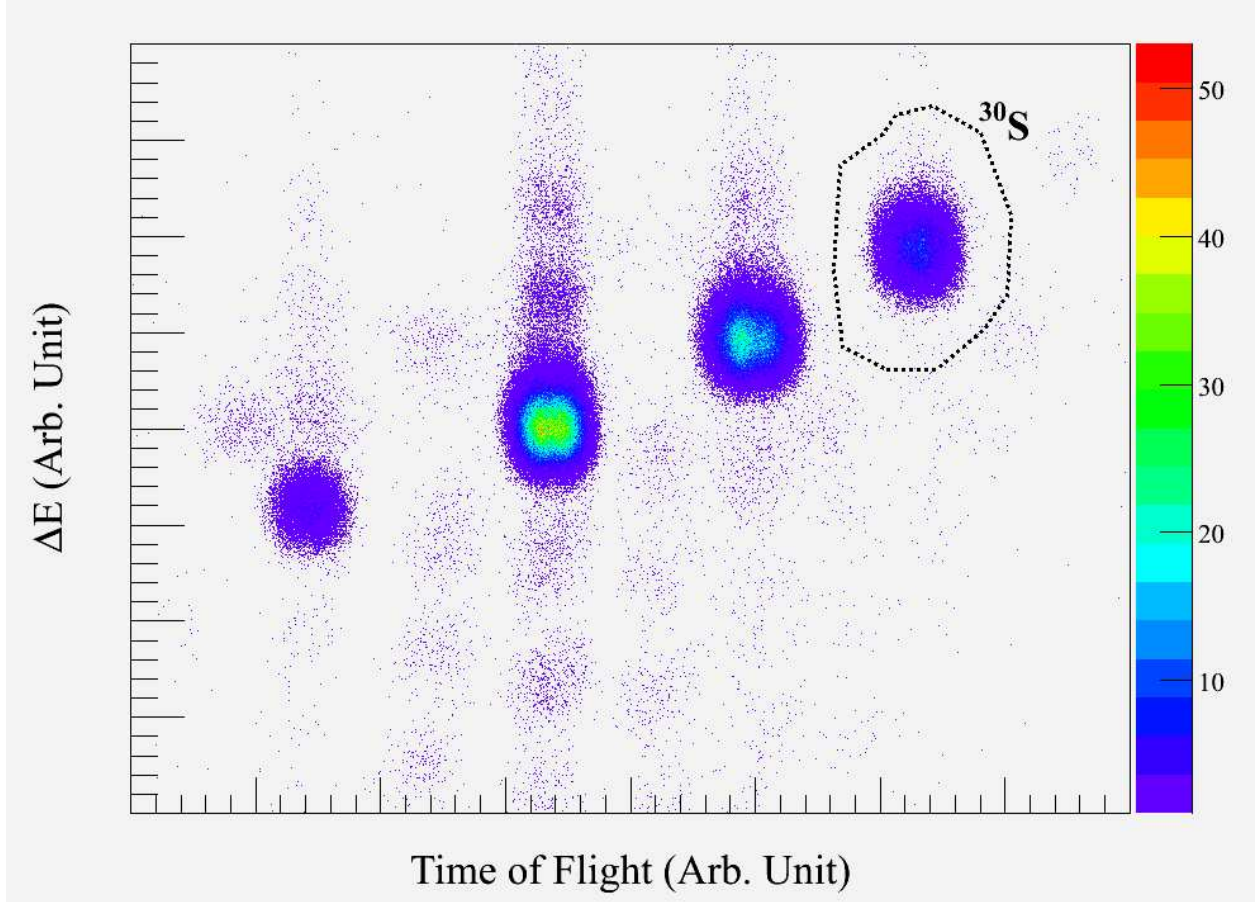


Figure 4.13: The particle identification spectrum of the  $^{30}\text{S}$  secondary cocktail beam from a beam normalization run. The particle identification logic gate used in the  $^{30}\text{S}$  beam normalization runs is shown.

The average  $^{30}\text{S}$  cocktail beam particle rate per run as measured in the object plane scintillator is shown in Fig. 4.16. The average beam particle rate per run for the first data set is  $1.81 \times 10^5$  counts per second, and the second data set has an average beam particle rate per run of  $4.10 \times 10^5$  counts per second.

The particle detection efficiencies of the S800 detectors per run during both of the  $^{29}\text{S}$  fragmentation runs is shown in Fig. 4.17. The average total particle detection efficiency  $\varepsilon_f$  of the first data set is 84.5(12)% and 32.3(8)% for the second data set. As discussed earlier and shown in Fig. 4.17, the extended focal plane scintillator's degraded detection efficiency was the main cause of the particle detection efficiency loss. The object plane scintillator has also degraded some between the first data set and the second data set, but this is also partially

caused by a higher beam intensity on the object plane scintillator. The noticeable dip in the extended focal plane and the object plane scintillators' detection efficiency was caused by an increase in the beam intensity between run numbers 86 and 89. The CRDC correction factor  $\eta_{crdc} = 1.24(7)$  was determined from the  $d_t$  spectrum of the combined data set and as described in Sec. 3.2.4. The live-time correction factors per run for the PS and COINC triggers are shown in Fig. 4.18. For the first data set, the average live-time correction factors of the PS and COINC triggers are 75.2(1)% and 67.08(3)% respectively. The second data set had average live-time correction factors of 61.3(1)% for the PS trigger and 53.34(3)% for the COINC trigger. The fragmentation reaction rate  $N_f$  per run is plotted in Fig. 4.19, with an error weighted average  $N_f$  for the first and second data set respectively of  $5.94(12) \times 10^{-5}$  and  $5.59(20) \times 10^{-5}$  reaction residues per object scintillator count. Using Eq. 4.1 and the error weighted average values of  $N_b$  and  $N_f$ , the inclusive cross section for the  $^{30}\text{S} \rightarrow ^{29}\text{S}$  reaction is determined to be 27.5(26) mb. This is the weighted average of the calculations from the first data set of 26.7(36) mb and the second data set of 28.5(40) mb.

### 4.3.2 $\gamma$ -Ray Analysis

The pre-target  $B\rho$  was set to 3.05 Tm and the post-target  $B\rho$  was set to 2.67 Tm. Using Eq. 3.7, these settings correspond to velocities of  $\beta = 0.464$  for the pre-target  $^{30}\text{S}$  projectiles and  $\beta = 0.429$  post-target  $^{29}\text{S}$  projectile-like fragmentation residues. The  $^{30}\text{S} \rightarrow ^{29}\text{S}$  reaction was determined to have an optimal mid-target velocity of 43.5% of the speed of light for the  $\gamma$ -ray energy Doppler reconstruction. The Doppler corrected  $\gamma$ -ray energy spectrum is shown in Fig. 4.20. Three photopeaks are seen with energies of 1160(16) keV, 1222(30) keV, and 1727(37) keV. Three GEANT simulations were performed to determine the SeGA's detection efficiency of the observed photopeaks, one simulation per photopeak. The simulations were fit to the data as shown in Fig. 4.21 and described in Sec. 4.1.2.2. The  $\gamma$ -ray energy spectrum is taken as the summed spectrum of both data sets. This summed spectrum is used to determine the total number of efficiency corrected photopeak emissions from the reaction residues. Because of the differences between the two  $^{29}\text{S}$  fragmentation data sets, it is necessary to split the total number of efficiency adjusted photopeak counts for the combined data sets into the appropriate separate counts for each data set. The total efficiency adjusted photopeak count rate from the GEANT simulated photopeak fits, is split into the counts for the first data set and the counts for the second data set in accordance

Table 4.5: The  $\gamma$ -ray emission rates  $N_\gamma$  per count in the object plane scintillator and the relative  $\gamma$ -ray intensity  $I_\gamma$  per fragmentation reaction for the  $^{30}\text{S} \rightarrow ^{29}\text{S}$  knockout reaction. The calculations are performed according to Eq. 4.6 and Eq. 4.8 for both  $^{29}\text{S}$  data sets separately. The far left column is the observed photopeak energy.

Energy (keV)	First Set		Second Set	
	$N_\gamma$	$I_\gamma$	$N_\gamma$	$I_\gamma$
1160(16)	$3.62(33) \times 10^{-6}$	6.10(56)%	$3.51(32) \times 10^{-6}$	6.29(62)%
1222(30)	$6.58(40) \times 10^{-6}$	11.1(7)%	$6.39(41) \times 10^{-6}$	11.4(8)%
1727(37)	$4.47(38) \times 10^{-6}$	7.51(65)%	$4.33(38) \times 10^{-6}$	7.75(72)%

with the ratios of the particle gated COINC triggers from each data set. Once the efficiency adjusted photopeak counts for each data set is determined, the  $\gamma$ -ray emission rates and intensities are determined for each data set separately. These calculations for the first and second  $^{29}\text{S}$  data sets are performed using Eq. 4.6 and Eq. 4.8 for each photopeak and the results are shown in Table 4.5.

Unfortunately the statistics were too low to perform particle- $\gamma$ - $\gamma$  coincidence measurements and the parallel momentum distributions for the populated excited states were compromised too much by the damaged CRDC section to make reliable comparison's with theoretical distributions.

The electromagnetic decay schemes and excited state energy levels for  $^{29}\text{S}$  were determined by comparing the observed photopeaks with the expected values from the *USDB* shell-model calculations and the experimental values of the isospin mirror  $^{29}\text{Al}$ . Judging from the theoretical calculations, it would appear that the possibility of having three distinct states at 1160 keV, 1222 keV, and 1727 keV is not a possibility and there is feeding from one excited state into another. The observed 1727 keV  $\gamma$ -ray matches up well with the predicted energy of the first  $7/2^+$  state at 1858 keV, however the direct population of this state is forbidden for the direct neutron knockout reaction from the ground state of  $^{30}\text{S}$ . This can be explained by a direct feeding of the 1727 keV state from a state at 2887 keV via the observed 1160 keV  $\gamma$ -ray, rationalized by the similar  $\gamma$ -ray intensities of the observed 1727 keV photopeak and the 1160 keV photopeak. The population of an excited state at 2887 keV also corroborates well with the  $5/2^+$  state predicted at 2993 keV by the *USDB* shell-model. The assumption that the experimentally determined 2887 keV state corresponds to the 2993

keV *USDB* state is the relative strength of this states theoretical spectroscopic factor to that of the other states in this energy region as shown in Table 2.2. This accounts for both the 1727 keV and the 1160 keV observed  $\gamma$ -rays, leaving only the 1222 keV  $\gamma$ -ray to be assigned a corresponding state. The observed 1222 keV photopeak is most likely the decay from the first  $1/2^+$  state predicted at 1214 keV to the ground state.

To summarize, it is determined that two excited states are populated in the  $^{29}\text{S}$  reaction residue, a  $1/2^+$  state at 1222(20) keV and a  $5/2^+$  state at 2887(40) keV. The populated  $1/2^+$  excited state decays directly to the ground state. The populated  $5/2^+$  state decays by an 1160(16) keV  $\gamma$ -ray to the  $7/2^+$  state at 1727(37) keV which then decays directly to the ground state. This decay scheme is in good agreement with the theoretical *USDB* electromagnetic transition calculations given in Table 2.4. The possibility of a direct decay of the 2887 keV state directly to the ground state is a possibility, however there was no observed 2887 keV photopeak. A GEANT simulated response function was created for a 2887 keV photopeak. As shown in Fig. 4.22, a 2887 keV  $\gamma$ -ray should have been observed if this decay branch had an equal intensity to that of the 1727  $\gamma$ -ray. The simulated 2887 keV photopeak becomes difficult to distinguish from the background noise at an intensity equal to roughly half that of the measured 1727 keV photopeak, so it is safe to assume that the 2887 keV  $\gamma$ -ray decay branch is less than or at most equal to half of the 1160 keV  $\gamma$ -ray decay branch for the populated  $5/2^+$  state.

Using the proposed energy level and  $\gamma$ -ray decay scheme, the partial state cross sections are determined for the direct population of the 1222 keV and 2887 keV excited states. The partial state branching reaction ratio  $b_i$  from Eq. 4.9 for the 1222 keV state is just equal to the 1222 keV  $\gamma$ -ray's intensity  $I_\gamma$ . It is approximated that the 2887 keV state is completely accounted for by the 1160 keV  $\gamma$ -ray decay branch, resulting in both the individual 1160 keV and 1727 keV photopeak intensities being equal to the partial cross section's branching ratio for the direct population of the state at 2887 keV. Because of this the 2887 keV state's partial cross section is determined as the error weighted average of the individual calculations using both the 1160 keV photopeak's intensity and the 1727 keV photopeak's intensity in Eq. 4.9 and Eq. 4.2.

As previously stated, the partial state cross sections were calculated for each data set independently and then averaged together to determine the final results. The final calculations of the partial cross sections for the direct population of the excited state in

$^{29}\text{S}$  from the neutron knockout from  $^{30}\text{S}$  are  $\sigma_{1222}^{\text{partial}} = 3.09(33)$  mb and  $\sigma_{2887}^{\text{partial}} = 1.86(15)$  mb. The partial cross section to the ground state was calculated using the averaged results from both data sets and Eq. 4.10. The direct reaction cross section to the ground state is  $\sigma_{\text{GS}} = 22.6(27)$  mb. A level scheme diagram of  $^{29}\text{S}$  along with appropriate experimental and theoretical comparisons is provided in Fig. 4.23.

### 4.3.3 Longitudinal Momentum Distributions

The longitudinal momentum distributions are shown in Fig. 4.24, the inclusive  $^{29}\text{S}$  momentum distribution shows a good agreement with the  $\ell = 2$ ,  $d_{5/2}$  ground state, which should be expected since it is a very dominant reaction channel. The 1160 keV and 1222 keV photopeaks were too close in energy to untangle their respective momentum distributions from coincidence measurements, so only the momentum distribution in coincidence with the combined 1160 keV and 1222 keV  $\gamma$ -rays could be obtained as well as the momentum distribution in coincidence with the 1727 keV photopeak. There was not enough quality data to make any positive identification of the orbital angular momentum values for any of the excited states from their pure momentum distributions.

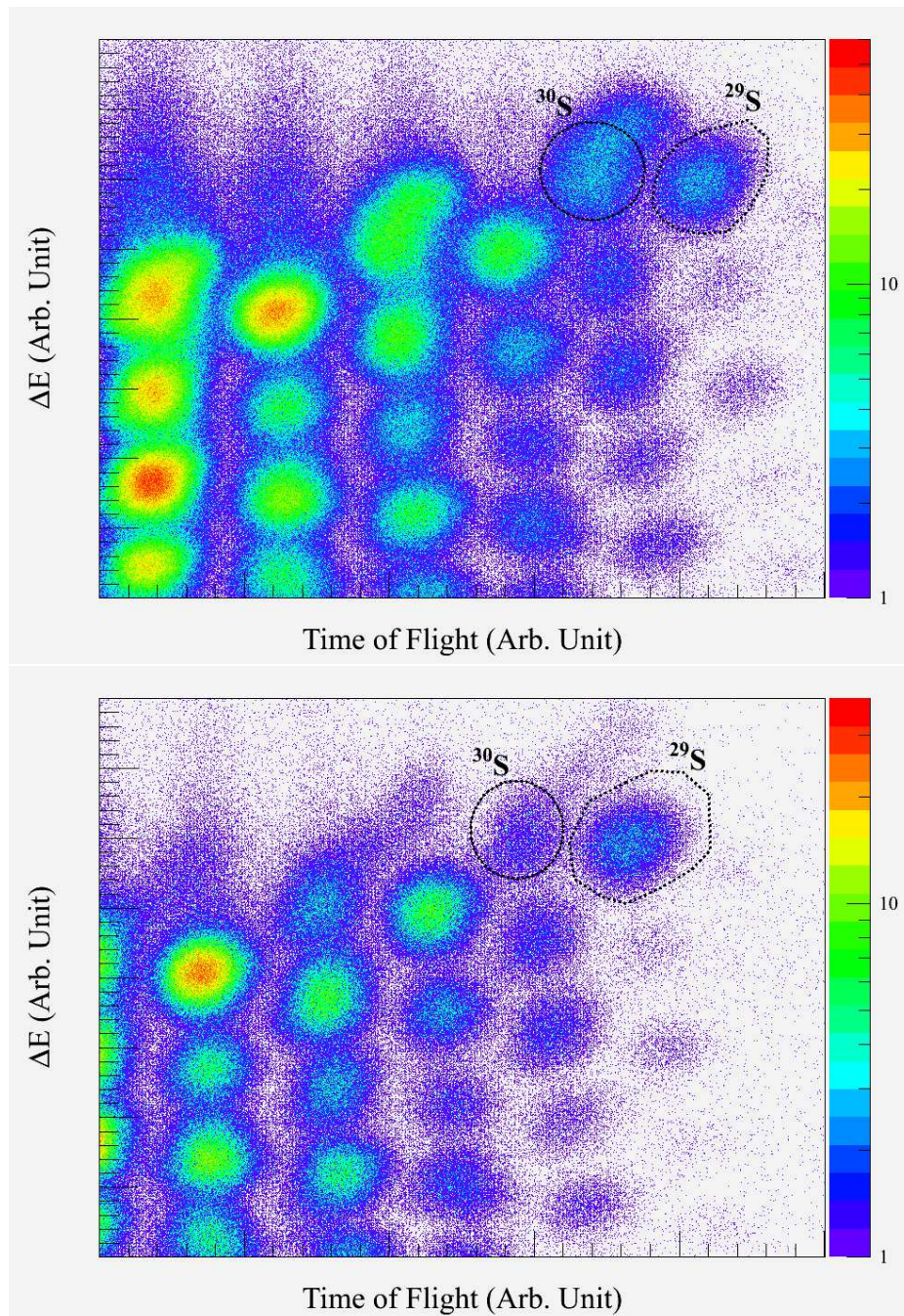


Figure 4.14: The particle identification spectrum of the  $^{29}\text{S}$  fragmentation reaction data runs. The top figure is from the first data set and the bottom figure is from the second data set. The particle identification logic gate used is shown and labeled. As shown, some of the unreacted  $^{30}\text{S}$  projectiles still make it into the S800's focal plane detectors.

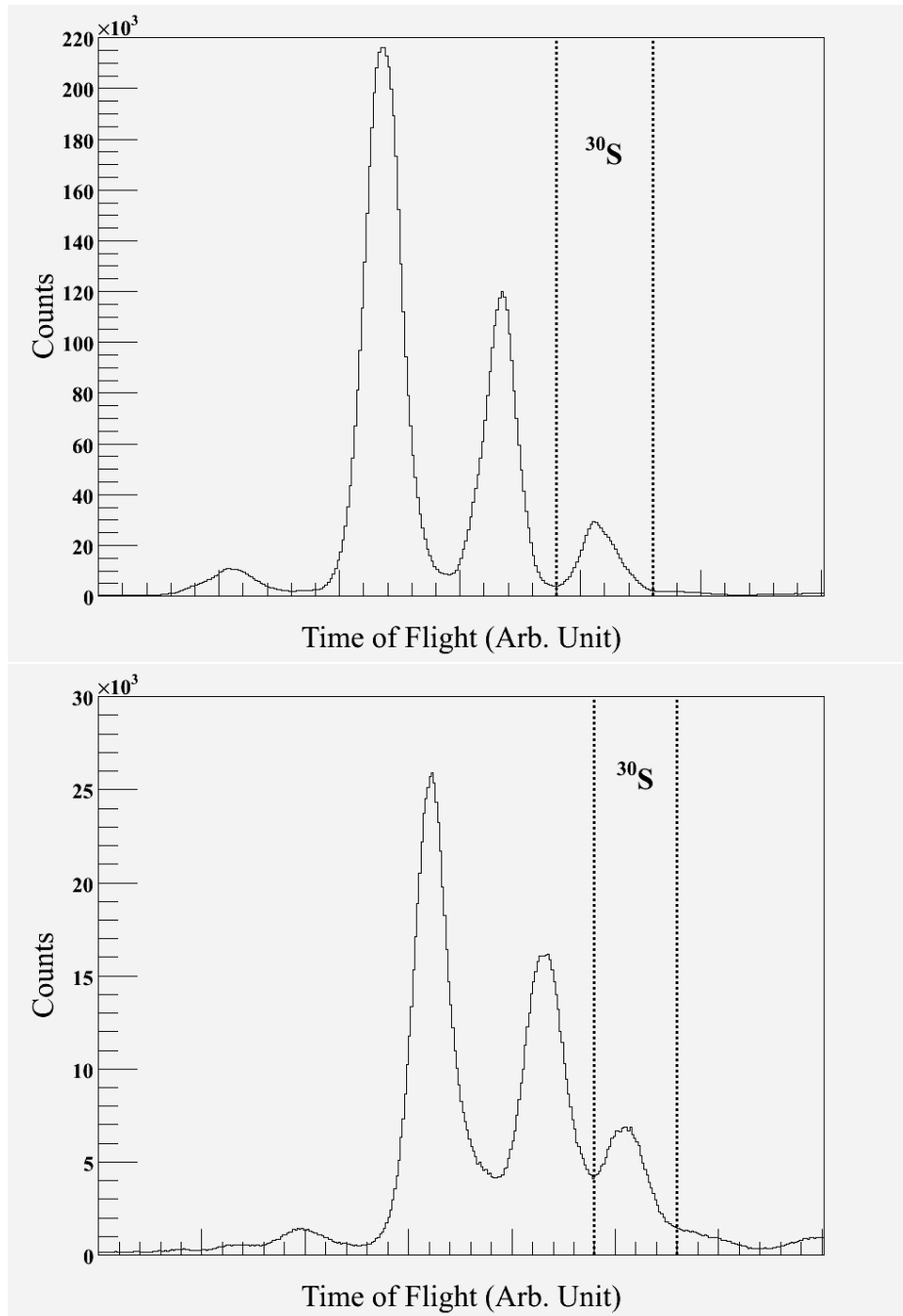


Figure 4.15: The time-of-flight difference spectrum between the extended focal plane and the object plane scintillators for the  $^{30}\text{S}$  cocktail beam from the fragmentation data runs. The top figure is from the first data set and the bottom figure is from the second data set. There are four large visible peaks, each corresponding to a different isotope in the secondary beam. The  $^{30}\text{S}$  identification logic gate is shown.

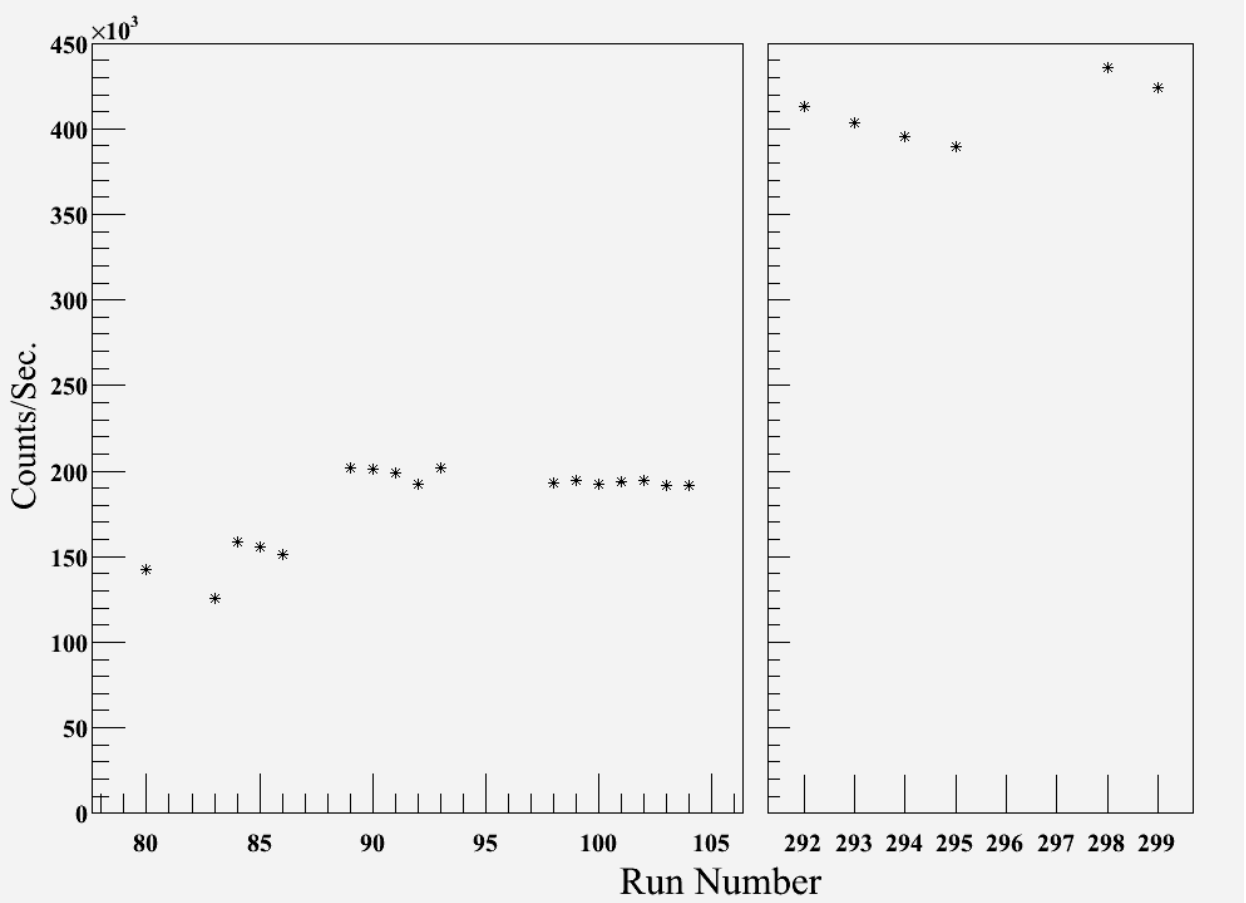


Figure 4.16: The average per run total beam rate measured in the object plane (OBJ) scintillator per run from the  $^{30}\text{S} \rightarrow ^{29}\text{S}$  fragmentation reaction data runs. The data is taken for all particles in the secondary beam passing through the object plane scintillator.

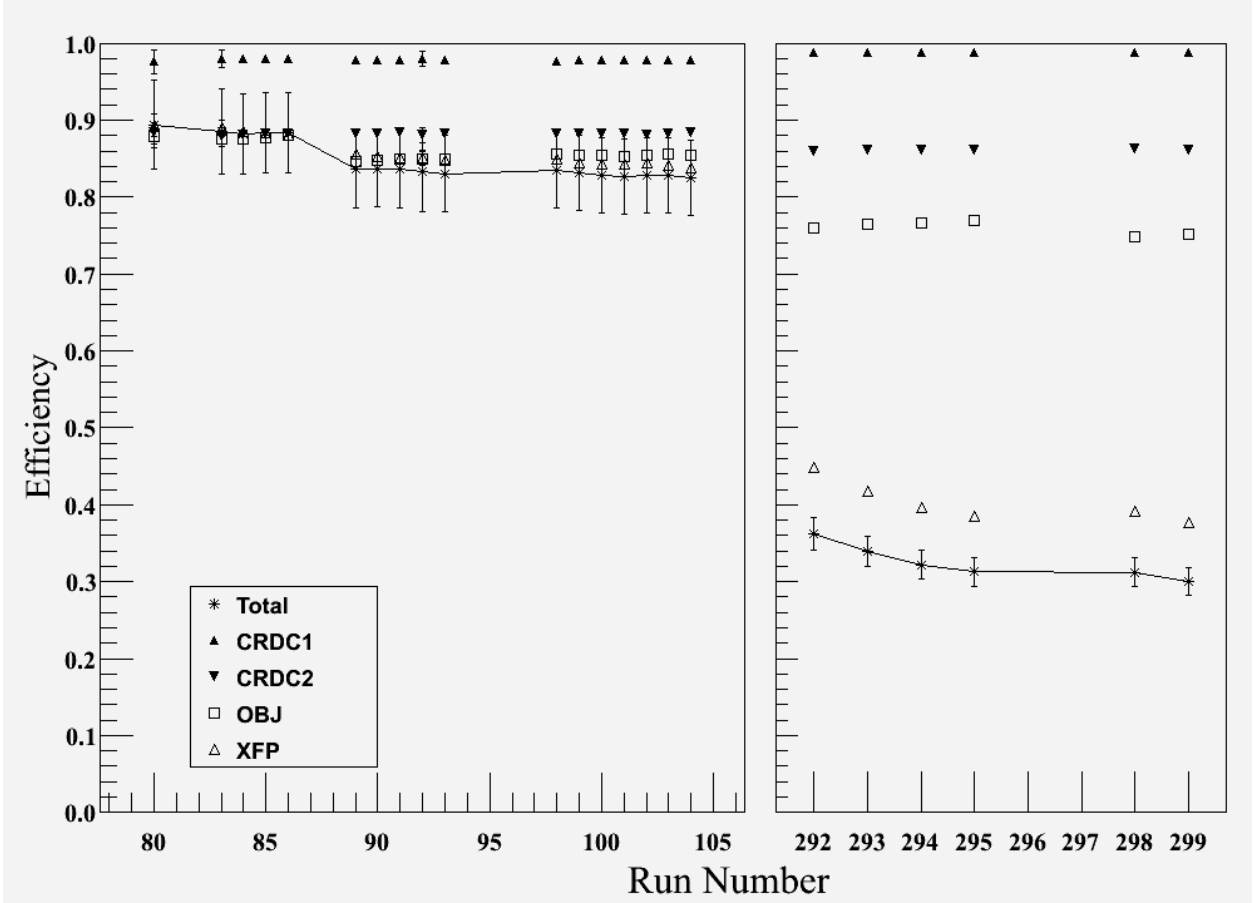


Figure 4.17: The particle detection efficiency values for each run used in the  $^{30}\text{S} \rightarrow ^{29}\text{S}$  fragmentation data sets. The figure is broken horizontally to separate the runs in the first data set on the left-hand side from the runs of the second data set on the right-hand side. The individual detector efficiencies are shown, along with the total detection efficiency. The total detection efficiency includes the CRDC correction factor  $\eta_{crdc}$ . Note that the horizontal axis is scaled by run number, not the total elapsed beam time for each run.

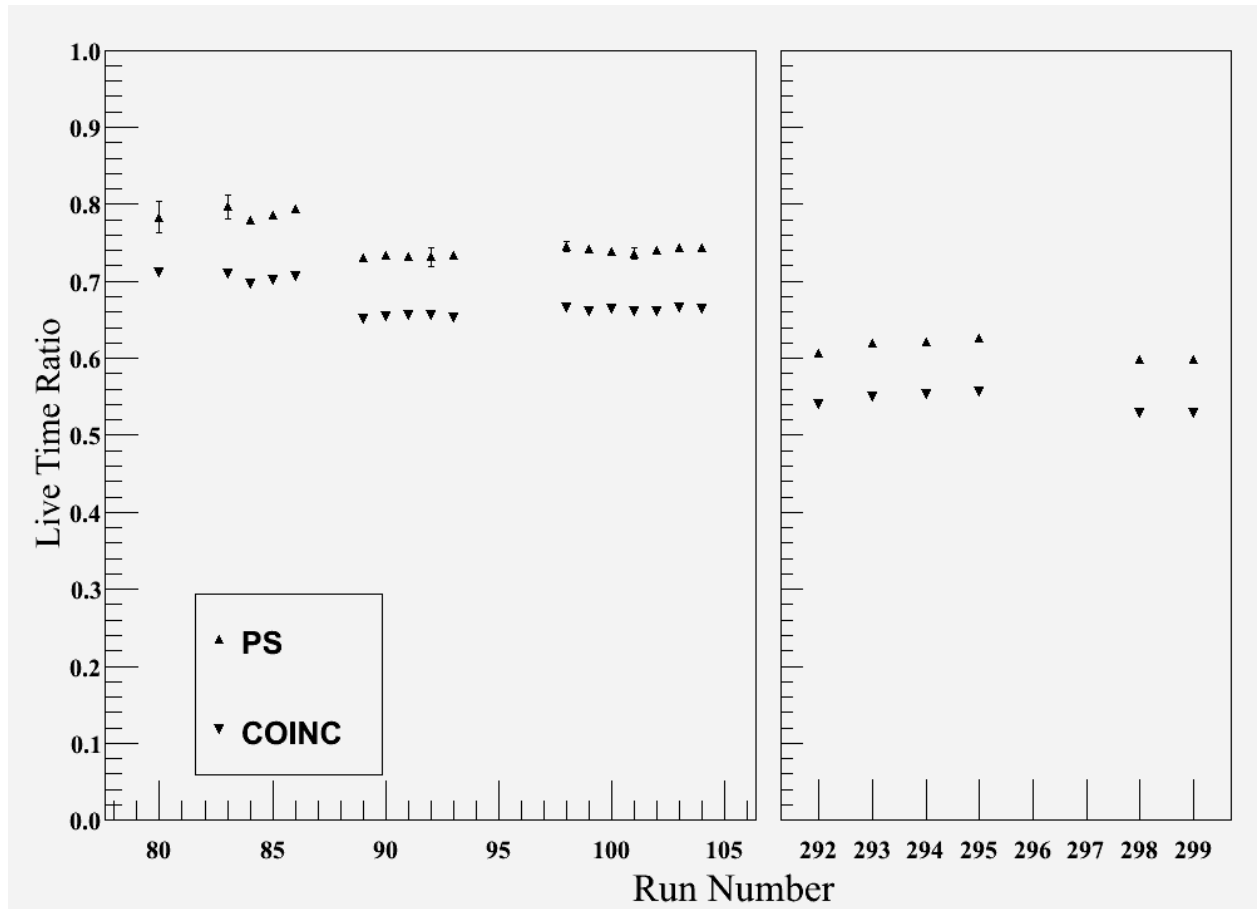


Figure 4.18: The PS and COINC trigger live-time corrections for each run used in the  $^{30}\text{S} \rightarrow ^{29}\text{S}$  fragmentation data sets. The figure is broken horizontally to separate the runs in the first data set on the left-hand side from the runs of the second data set on the right-hand side. Note that the horizontal axis is scaled by run number, not the elapsed beam time for each run.

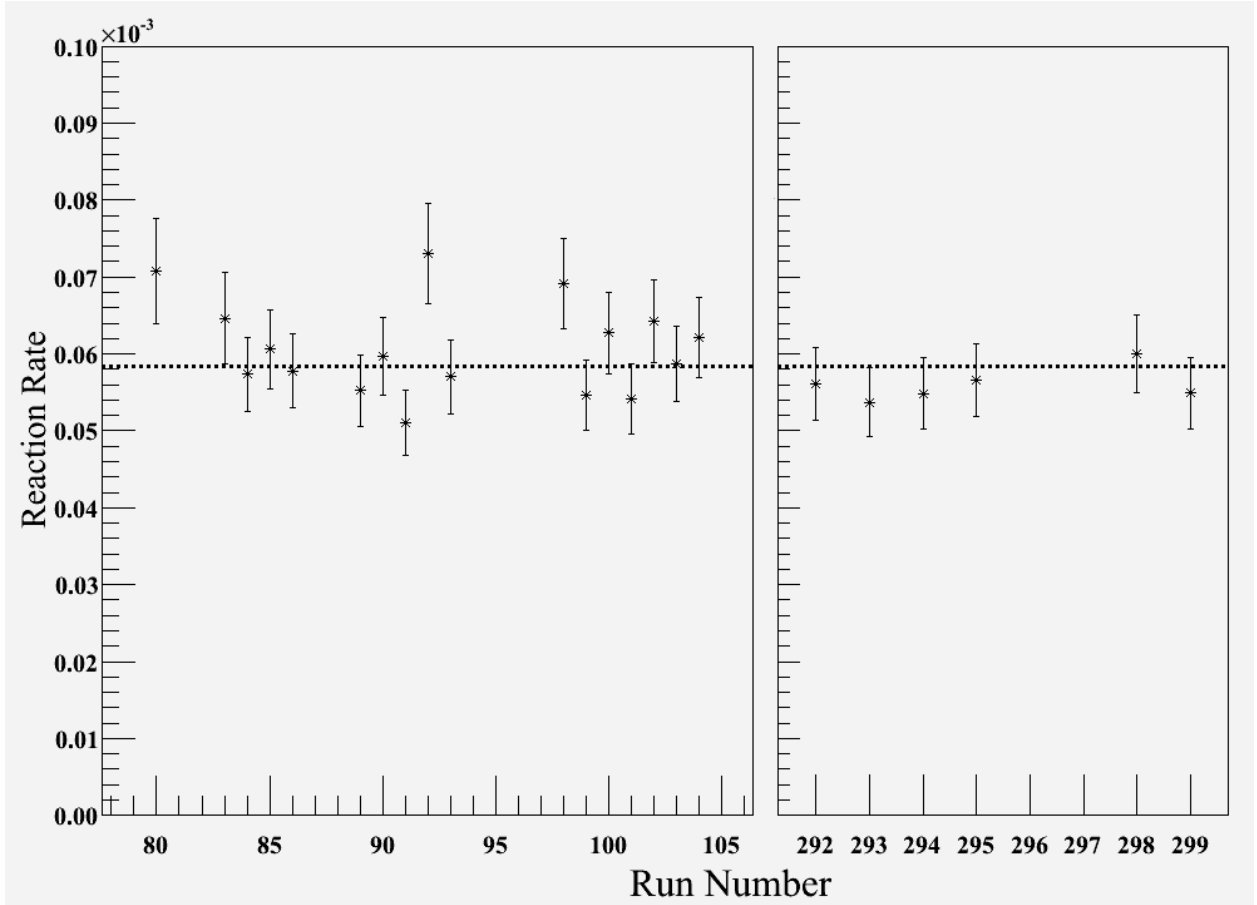


Figure 4.19: The fragmentation reaction rate for each run used in the  $^{30}\text{S} \rightarrow ^{29}\text{S}$  data sets. The figure is broken horizontally to separate the runs in the first data set on the left-hand side from the runs of the second data set on the right-hand side. Note that the horizontal axis is scaled by the run number, not the elapsed beam time for each run. A horizontal line is drawn for error weighted average of all of the data points at  $N_f = 5.84 \times 10^{-5}$ .

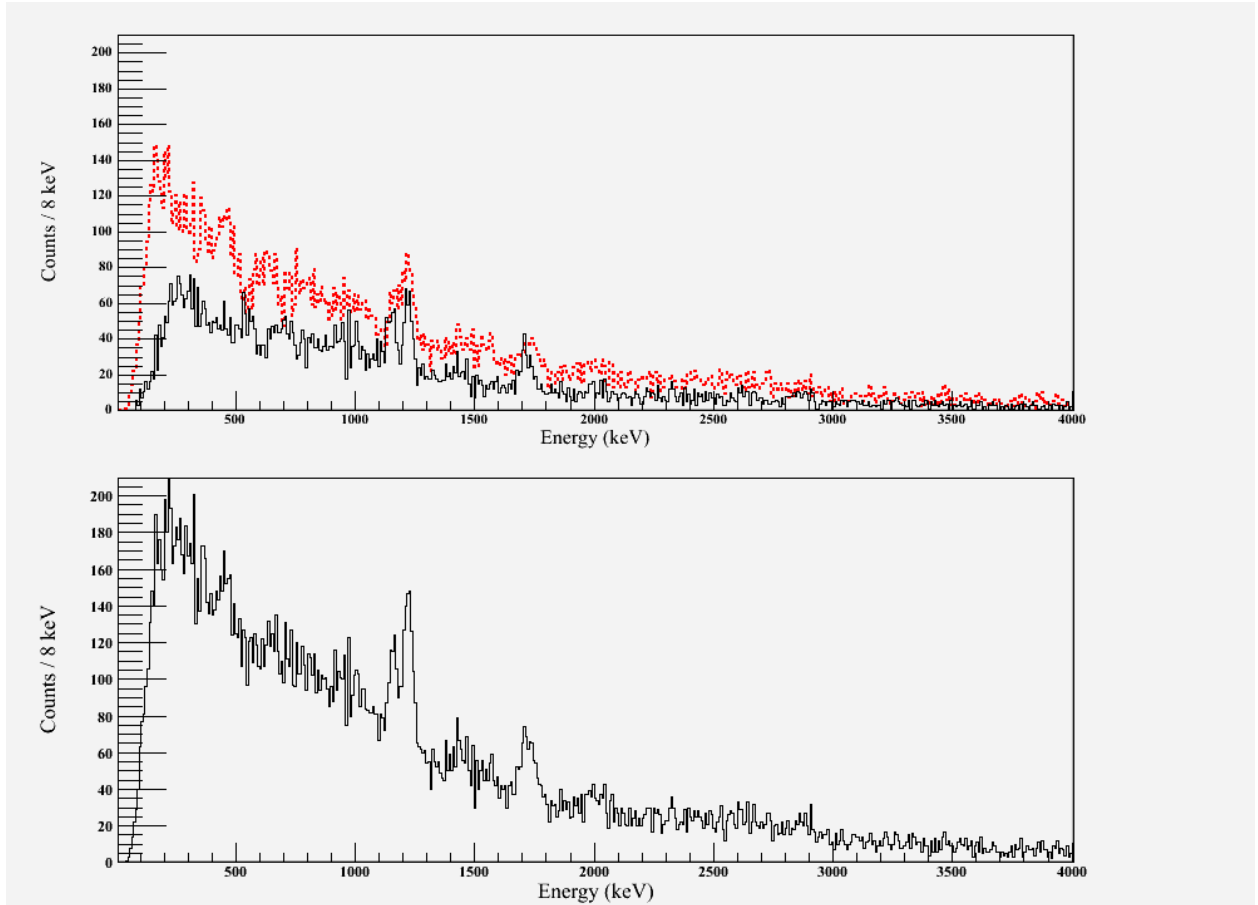


Figure 4.20: The Doppler reconstructed  $\gamma$ -ray energy spectrum of  $^{29}\text{S}$  collected from all of the  $^{30}\text{S} \rightarrow ^{29}\text{S}$  fragmentation reaction data runs. The top figure compares the  $37^\circ$  SeGA detector ring (dashed red line) to the  $90^\circ$  SeGA detector ring (solid black line). The bottom figure shows the summed SeGA  $\gamma$ -ray energy spectrum for  $^{29}\text{S}$ . The Doppler reconstruction was performed with a velocity of  $\beta = 0.435$ .

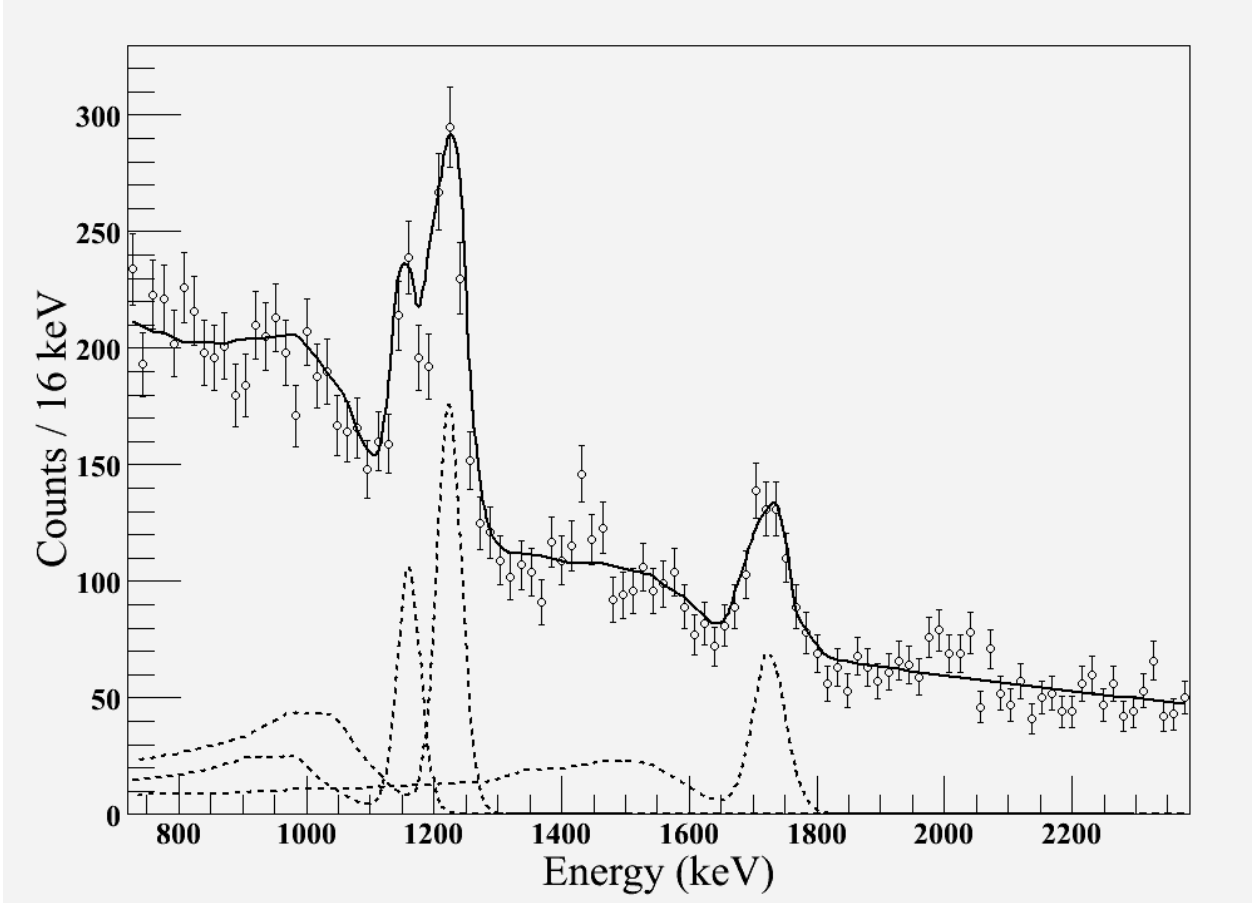


Figure 4.21: The simulated photopeaks (shown as dashed lines) are added to a background noise function as described in Sec. 4.1.2.2 and then fit to the  $^{29}\text{S}$   $\gamma$ -ray energy spectrum. The fitted function is shown as a solid line.

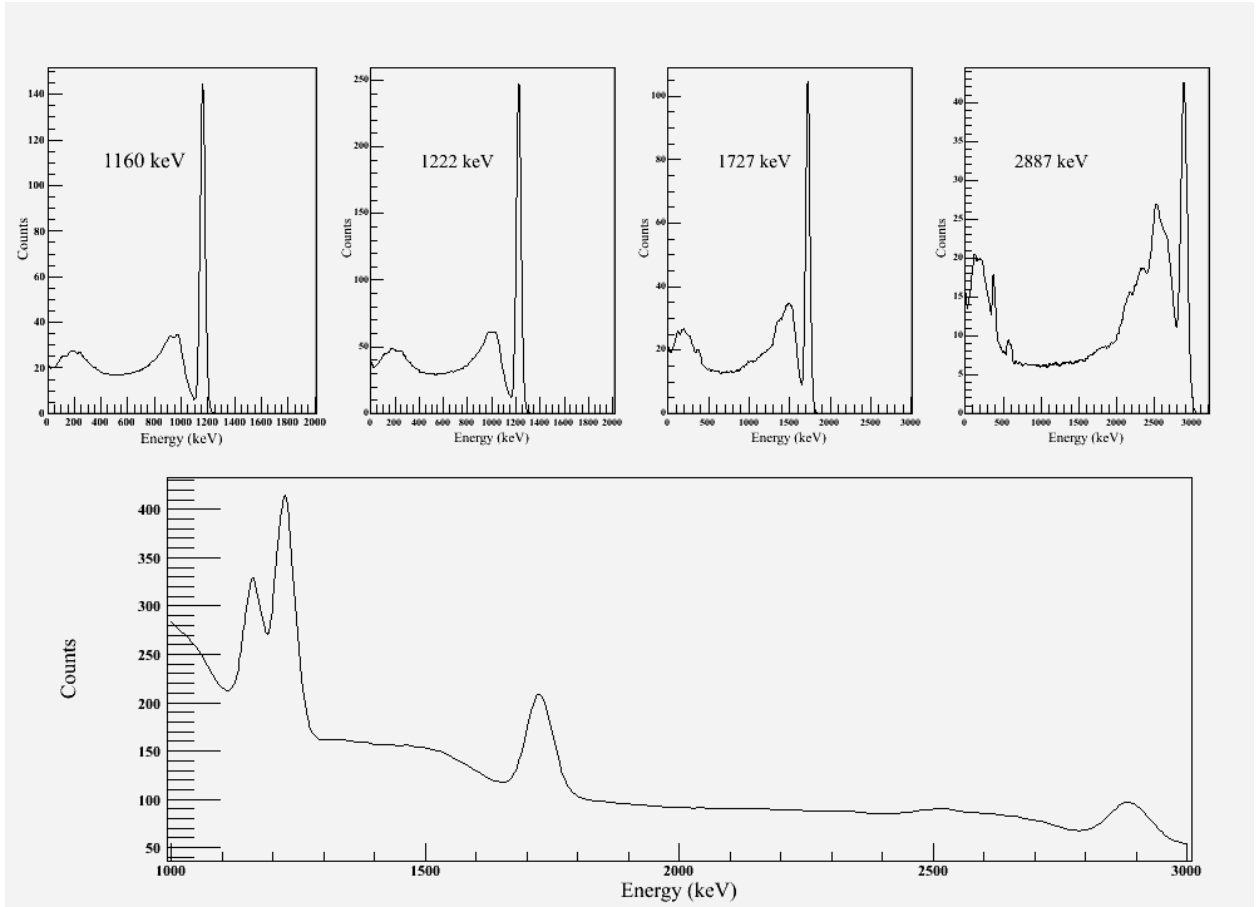


Figure 4.22: The top row shows the photopeak detection simulations for a 1160 keV, 1222 keV, 1727 keV, and 2887 keV  $\gamma$ -ray emission from the  $^{29}\text{S}$  fragment residue. The 2887 keV simulation is efficiency scaled to the same  $\gamma$ -ray intensity as the 1727 keV photopeak. The bottom figure shows the peaks from the top row added to the background function that was fit to the experimental data. It can be seen that the 2887 keV photopeak should have been observable if it was at an equal intensity to the 1727 keV photopeak.

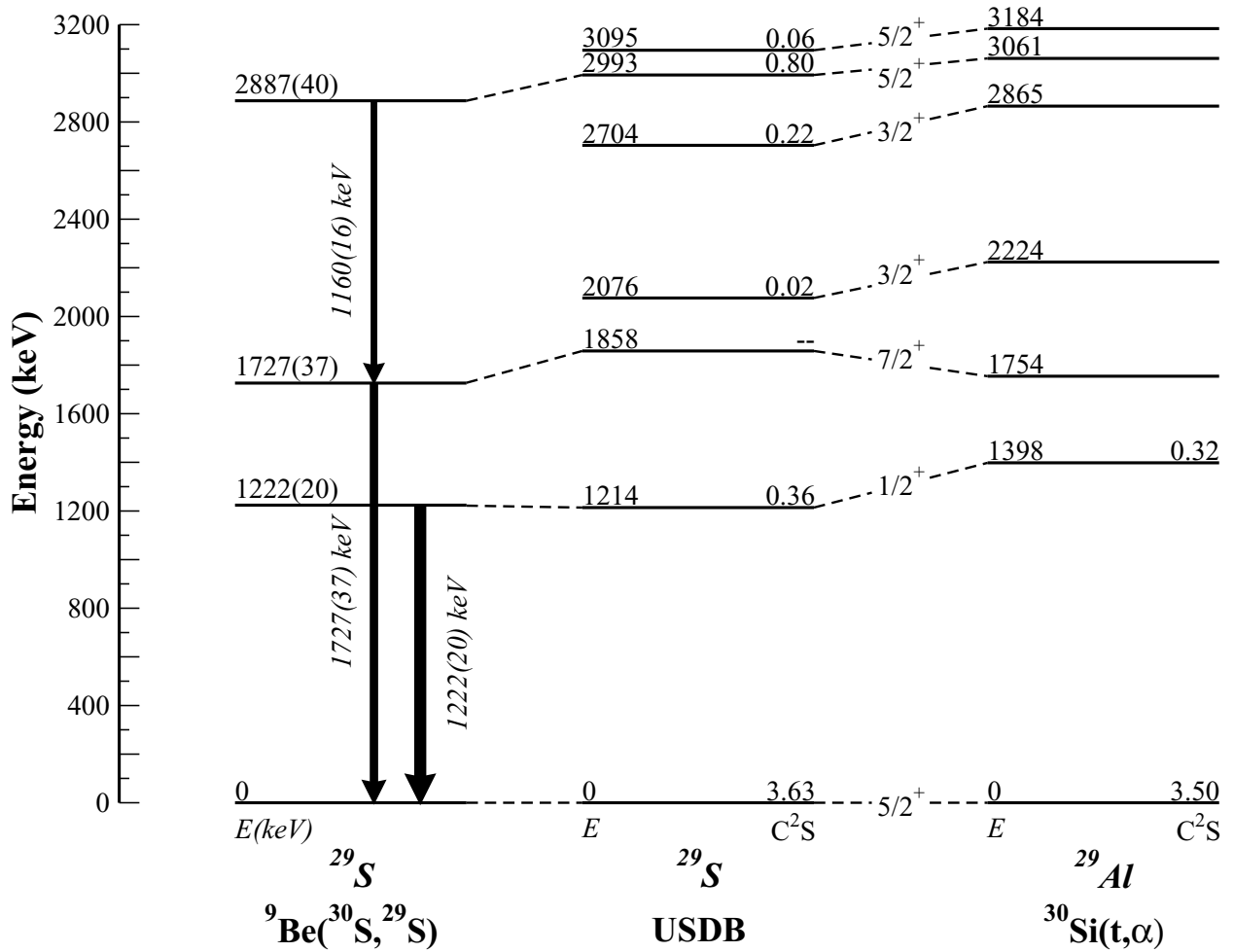


Figure 4.23: Three level diagrams are presented. From left to right:  $^{29}\text{S}$  from the present work;  $^{29}\text{S}$  from the *USDB* shell-model calculations; and the isospin mirror  $^{29}\text{Al}$  from experimental evidence collected in Ref. [54] and Ref. [55]. The electromagnetic transitions observed in the present study are also shown.

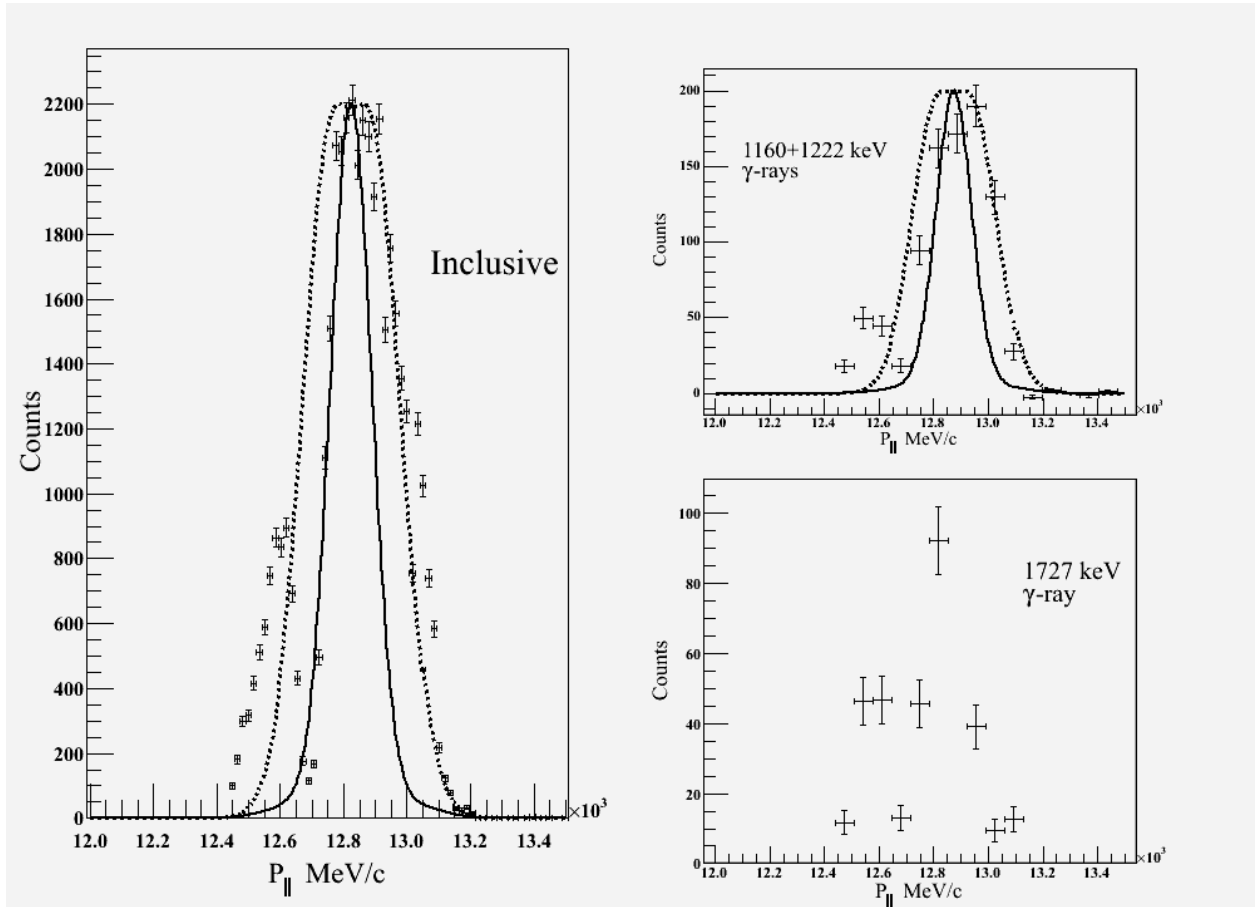


Figure 4.24: The longitudinal momentum distributions of  $^{29}\text{S}$ . The theoretical momentum distributions are shown as lines for comparison with the experimental momentum distributions. The solid line is for the  $\ell = 0$ ,  $s_{1/2}$  theoretical distribution and the dashed line is for the  $\ell = 2$ ,  $d_{5/2}$  and  $d_{3/2}$  theoretical distribution. The figure on the left hand side is the inclusive momentum distribution, it is in fairly good agreement with the  $\ell = 2$  distribution line, which is expected from the  $d_{5/2}$  ground state dominated reaction cross section. The top right figure is the pure momentum distribution in coincidence with the 1160 keV and 1222 keV photopeaks, and the bottom right figure is the pure momentum distribution of the 1727 keV photopeak.

## CHAPTER 5

### DISCUSSION AND CONCLUSIONS

The results obtained for both  $^{25}\text{Si}$  and  $^{29}\text{S}$  represent the first observations of electromagnetic decays from either isotope and the first observation of any excited states of  $^{29}\text{S}$ . In each of the two nuclei measured here, we have observed one state that the USDB shell model calculation indicates should be connected to the ground state by a strong  $E2$  transition. These states, at 821 keV in  $^{25}\text{Si}$  and 1727 keV in  $^{29}\text{S}$ , can be interpreted as rotational excitations of the ground state. Since the single neutron knockout reaction very selectively populates states that represent a neutron-hole coupled to the projectile, it would be beneficial to run future Coulomb excitation measurements, as described in Refs. [56, 57, 6], to determine the full electromagnetic transition spectrum up to the proton separation energy cut-off of 3.4 MeV in  $^{25}\text{Si}$  and 3.3 MeV in  $^{29}\text{S}$ .

Using the measured cross sections from Chap. 4 and the theoretical single particle cross sections presented in Table 2.5 and Table 2.6, it is possible to calculate the inclusive and individual state quenching reduction factors ( $R_S$ ) from Eq. 2.5. The  $R_S$  values are given in Table 5.1 as well as a summary of the pertinent results obtained in the present study.

The separation energy difference,  $\Delta S$  from Eq. 2.6 and Sec. 2.1.2.1, is 13.5 MeV for  $^{26}\text{Si}$  with  $S_n = 19041(10)$  keV and  $S_p = 5518(3)$  keV.  $^{30}\text{S}$ , with  $S_n = 18980(50)$  keV and  $S_p = 4400(3)$  keV, has  $\Delta S = 14.6$  MeV. The observed reduction in spectroscopic strength in relationship to  $\Delta S$  is in good agreement with other results obtained from  $(e, e'p)$ , proton knockout, and other neutron knockout results as shown in Fig. 5.1, and Table 5.2, Table 5.3, and Table 5.4. Fig. 5.1, is an update of Fig.6 in Ref. [20], to include all nucleon knockout data to date. There has been some recent debate proposed in Ref. [67] as to the accuracy of the reaction model used here. The experiment in Ref. [67] used a DWBA reaction model to calculate spectroscopic strengths from a  $(p, d)$  neutron transfer reaction for several Ar

Table 5.1: The table presents a summary of the relevant results from the present study. The methods used to determine or calculate all of the quantities are discussed in the text. The shell model spectroscopic factors  $C^2S_{\text{SM}}$  are from the USDB Hamiltonian calculations, and these are used to determine the theoretical single reaction cross section  $\sigma_{th}$  from Eq. 2.8. The quenching reduction factors  $R_S$  are calculated using Eq. 2.5. The angular momentum and parity  $J^\pi$  values in parentheses are tentatively assigned based on comparisons with shell model calculations as described in Chap. 4.

Residue	$E_{level}$ (keV)	$E_\gamma$ (keV)	$\sigma_{exp}$ (mb)	$J^\pi$	$C^2S_{\text{SM}}$	$\sigma_{th}$ (mb)	$R_S$
$^{25}\text{Si}$	1909(27)	1088(22)	1.06(21)	(3/2 <sup>+</sup> )	0.18	2.36	0.45(9)
	821(15)	821(15)	4.06(61)	(1/2 <sup>+</sup> )	0.25	3.64	1.12(17)
	40(5)[Ref. [51]]			(3/2 <sup>+</sup> )	0.12	1.65	
	G.S.			5/2 <sup>+</sup>	2.73	40.0	
	G.S.+40keV		21.0(35)			41.6	0.50(9)
	<i>inclusive</i>		26.1(35)			47.6	0.55(7)
$^{29}\text{S}$	2887(40)	1160(16)	1.86(15)	(5/2 <sup>+</sup> )	0.80	9.32	0.20(2)
	1727(37)	1727(37)		(7/2 <sup>+</sup> )			
	1222(20)	1222(20)	3.09(33)	(1/2 <sup>+</sup> )	0.36	4.89	0.63(7)
	G.S.		22.6(27)	5/2 <sup>+</sup>	3.63	45.9	0.49(4)
	<i>inclusive</i>		27.5(26)			60.1	0.46(4)

isotopes that had been measured in neutron knockout reactions. The large reductions seen in the neutron knockout reactions were not observed in the transfer reactions. On the other hand, a recent  $^9\text{C}$  and  $^9\text{B}$  proton knockout experiment presented in Ref. [24], measured separately, both the stripping and the diffraction cross sections as described in Sec. 2.2. The results were in excellent agreement with theory. In light of these studies and the implications that the reduction factors have on the current state of shell model and nuclear structure in both exotic and stable nuclei, it is important to test the reaction models that are being created for a the new generations of exotic beam experiments. As discussed in Refs. [6, 10] and shown in the present work, the systematic reduction of spectroscopic strengths from the theoretical predictions provides valuable insight into a deviation from current standard shell model theories that will hopefully help in creating the next generation of nuclear structure models.

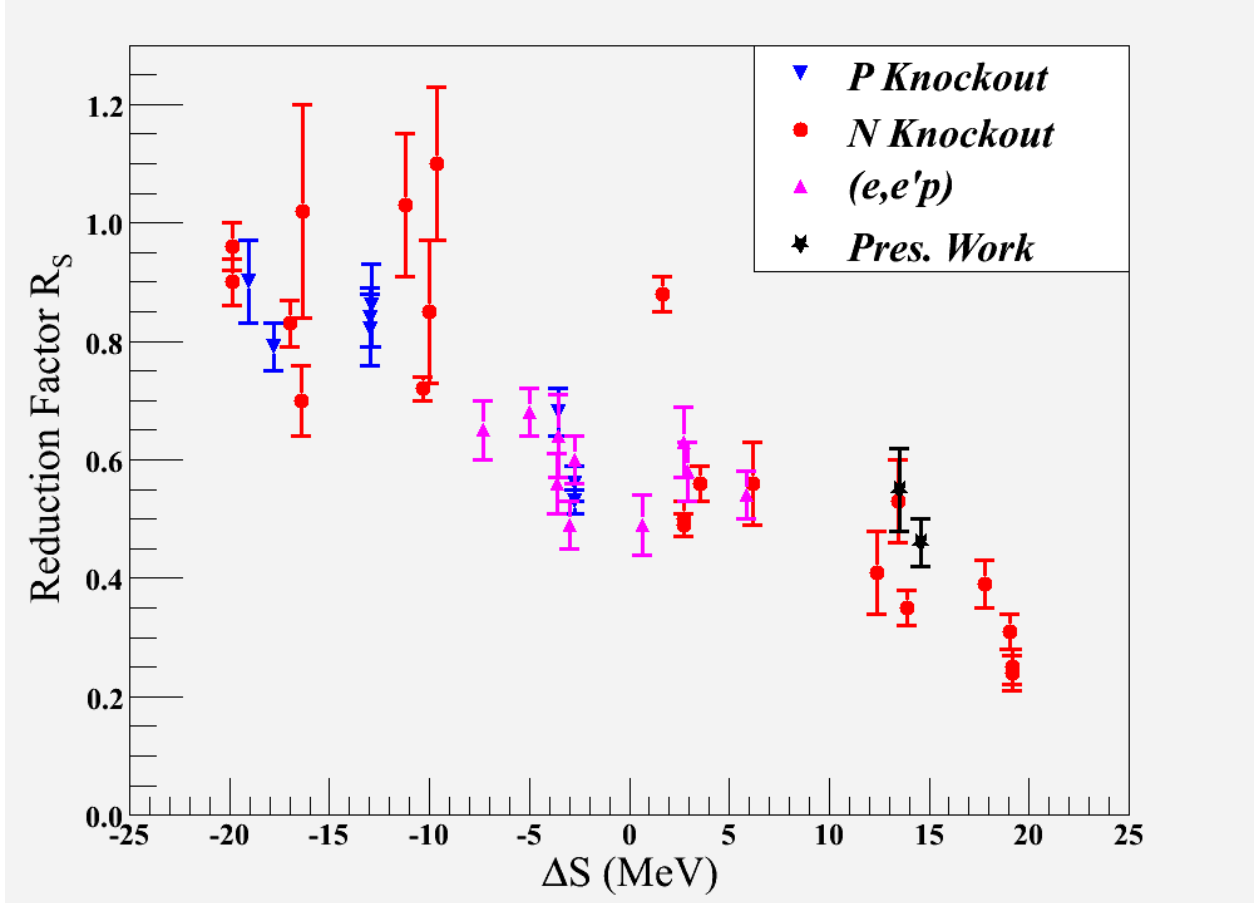


Figure 5.1: A cumulative plot of inclusive quenching reduction factors  $R_S$  versus their respective separation energy differences  $\Delta S$ . This is an update to Fig.6 in Ref. [20]. The values for the  $(e, e'p)$  reaction data points are given in Table 5.2. The values used for the proton knockout data points are given in Table 5.3. The values used for the neutron knockout data points are given in Table 5.4.

Table 5.2: The inclusive reduction factors  $R_S$  and separation energy differences  $\Delta S$  calculated from several  $(e, e'p)$  experiments. Ref. [58] recalculated the reduction factors from their original results.

$(e, e'p)$ Reaction			
$\Delta S$ (MeV)	$R_s$	Parent Nuclei	Reference
5.86	0.54(4)	$^{48}\text{Ca}$	Ref. [58]
2.90	0.58(5)	$^{30}\text{Si}$	Ref. [58]
2.73	0.63(6)	$^7\text{Li}$	Ref. [58]
0.64	0.49(5)	$^{208}\text{Pb}$	Ref. [58]
-2.76	0.60(4)	$^{12}\text{C}$	Ref. [58]
-2.99	0.49(4)	$^{51}\text{V}$	Ref. [58]
-3.54	0.64(7)	$^{16}\text{O}$	Ref. [58]
-3.62	0.56(5)	$^{90}\text{Zr}$	Ref. [58]
-5.01	0.68(4)	$^{31}\text{P}$	Ref. [58]
-7.31	0.65(5)	$^{40}\text{Ca}$	Ref. [58]

Table 5.3: The inclusive reduction factors  $R_S$  and separation energy differences  $\Delta S$  calculated from several proton knockout experiments.

$p$ -Knockout Reaction			
$\Delta S$ (MeV)	$R_s$	Parent Nuclei	Reference
-2.76	0.56(3)	$^{12}\text{C}$	Ref. [21]
-2.76	0.53(2)	$^{12}\text{C}$	Ref. [58]
-3.54	0.68(4)	$^{16}\text{O}$	Ref. [21]
-3.54	0.68(4)	$^{16}\text{O}$	Ref. [58]
-12.88	0.86(7)	$^8\text{B}$	Ref. [58]
-12.88	0.86(7)	$^8\text{B}$	Ref. [24]
-12.96	0.82(6)	$^9\text{C}$	Ref. [58]
-12.96	0.84(5)	$^9\text{C}$	Ref. [24]
-17.79	0.79(4)	$^{24}\text{Si}$	Ref. [20]
-19.04	0.90(7)	$^{28}\text{S}$	Ref. [20]

Table 5.4: The inclusive reduction factors  $R_S$  and separation energy differences  $\Delta S$  calculated from several neutron knockout experiments.

<i>n</i> -Knockout Reaction			
$\Delta S$ (MeV)	$R_s$	Parent Nuclei	Reference
19.14	0.24(3)	<sup>32</sup> Ar	Ref. [59]
19.14	0.25(3)	<sup>32</sup> Ar	Ref. [58]
19.04	0.31(3)	<sup>28</sup> S	Ref. [20]
17.79	0.39(4)	<sup>24</sup> Si	Ref. [20]
14.58	0.46(4)	<sup>30</sup> S	Pres. Work
13.88	0.35(3)	<sup>22</sup> Mg	Ref. [60]
13.52	0.55(7)	<sup>26</sup> Si	Pres. Work
13.47	0.53(7)	<sup>33</sup> Cl	Ref. [61]
12.41	0.41(7)	<sup>34</sup> Ar	Ref. [61]
12.41	0.41(7)	<sup>34</sup> Ar	Ref. [58]
6.18	0.56(7)	<sup>32</sup> S	Ref. [61]
3.54	0.56(3)	<sup>16</sup> O	Ref. [21]
3.54	0.56(3)	<sup>16</sup> O	Ref. [58]
2.76	0.50(3)	<sup>12</sup> C	Ref. [21]
2.76	0.49(2)	<sup>12</sup> C	Ref. [58]
1.64	0.88(3)	<sup>8</sup> Be	Ref. [21]
-9.63	1.10(13)	<sup>37</sup> S	Ref. [62]
-10.03	0.85(12)	<sup>46</sup> Ar	Ref. [63]
-10.03	0.85(12)	<sup>46</sup> Ar	Ref. [58]
-10.34	0.72(2)	<sup>45</sup> Cl	Ref. [64]
-11.20	1.03(12)	<sup>34</sup> Si	Ref. [62]
-16.32	1.02(18)	<sup>35</sup> Si	Ref. [62]
-16.41	0.70(6)	<sup>22</sup> O	Ref. [58]
-16.98	0.83(4)	<sup>44</sup> S	Ref. [65]
-19.86	0.90(4)	<sup>15</sup> C	Ref. [66]
-19.86	0.96(4)	<sup>15</sup> C	Ref. [58]

## REFERENCES

- [1] E. Rutherford. The Scattering of  $\alpha$  and  $\beta$  Particles by Matter and the Structure of the Atom. *Phil. Mag.*, 21:669, 1911. 1
- [2] E. Rutherford. Collision of Alpha Particles with Light Atoms. *Phil. Mag.*, 37:537–587, 1919. 1
- [3] J. Chadwick. Possible Existence of a Neutron. *Nature*, 129:312, 1932. 1
- [4] P. G. Hansen and J. A. Tostevin. Direct Reactions with Exotic Nuclei. *Ann. Rev. Nucl. Part. Sci.*, 53:219, 2003. 1, 2.1.2.1, 2.1.2.1, 2.2, 2.2.1, 2.2.1, 2.2.1, 2.2.1.1
- [5] G. J. Kramer, H. P. Blok, and L. Lapikás. A consistent analysis of (e,e'p) and (d,<sup>3</sup>He) experiments. *Nucl. Phys. A*, 679:267, 2001. 1, 2.1.2.1
- [6] A. Gade and T. Glasmacher. In-beam nuclear spectroscopy of bound states with fast exotic ion beams. *Prog. in Part. and Nucl. Phys.*, 60:161, 2008. 1, 2.1.1, 2.1.2.1, 2.1.2.1, 2.2, 2.2.1, 2.2.1, 5, 5
- [7] M. G. Mayer. On Closed Shells in Nuclei. *Phys. Rev.*, 74:235, 1948. 2.1
- [8] M. G. Mayer. On Closed Shells in Nuclei. II. *Phys. Rev.*, 75:1969, 1949. 2.1
- [9] O. Haxel, J. H. D. Jensen, and H. E. Suess. On the Magic Numbers in Nuclear Structure. *Phys. Rev.*, 75:1766, 1949. 2.1
- [10] O. Sorlin and M.-G. Porquet. Nuclear magic numbers: New features far from stability. *Prog. in Part. and Nucl. Phys.*, 61:602, 2008. 2.1, 2.1.1, 5
- [11] C. Mahaux and H. A. Weidenmüller. *Shell-Model Approach to Nuclear Reactions*. John Wiley & Sons, Inc., New York, 1969. 2.1.1, 2.1.2.1
- [12] A. Bohr and B. R. Mottelson. *Nuclear Structure*, volume 1. W. A. Benjamin, Inc., New York, 1969. 2.1.1, 2.1.3
- [13] E. Segrè. *Nuclei and Particles*. W.A. Benjamin, Inc., Reading, MA, 2nd edition, 1977. 2.1.1, 2.1.3, 3.1.2
- [14] E. Caurier, G. Martinez-Pinedo, F. Nowacki, A. Poves, and A. P. Zuker. The shell model as a unified view of nuclear structure. *Rev. Mod. Phys.*, 77:427, 2005. 2.1.1

- [15] W. Chung. *Empirical Renormalization of Shell-Model Hamiltonians and Magnetic Dipole Moments of sd-Shell Nuclei*. PhD thesis, Michigan State University, 1979. 2.1.1.1
- [16] B. H. Wildenthal. Empirical strengths of spin operators in nuclei. *Prog. in Part. and Nucl. Phys.*, 11:5, 1984. 2.1.1.1
- [17] B. A. Brown and B. H. Wildenthal. Status of the nuclear shell model. *Ann. Rev. Nucl. Part. Sci.*, 38:29, 1988. 2.1.1.1
- [18] B. A. Brown and W. A. Richter. New “USD” Hamiltonians for the *sd* shell. *Phys. Rev. C*, 74:034315, 2006. 2.1.1.1, 2.1.1.1, 2.4
- [19] A. E. L. Dieperink and T. de Forest. Center-of-mass effects in single-nucleon knock-out reactions. *Phys. Rev. C*, 10:543, 1974. 2.1.2.1, 2.2
- [20] A. Gade, P. Adrich, D. Bazin, M. D. Bowen, B. A. Brown, C. M. Campbell, J. M. Cook, T. Glasmacher, P. G. Hansen, K. Hosier, S. McDaniel, D. McGlinchery, A. Obertelli, K. Siwek, L. A. Riley, J. A. Tostevin, and D. Weisshaar. Reduction of spectroscopic strength: Weakly-bound and strongly-bound single-particle states studied using one-nucleon knockout reactions. *Phys. Rev. C*, 77:044306, 2008. 2.1.2.1, 2.1.2.1, 2.2.1, 2.2.1, 5, 5.1, 5.3, 5.4
- [21] B. A. Brown, P. G. Hansen, B. M. Sherrill, and J. A. Tostevin. Absolute spectroscopic factors from nuclear knockout reactions. *Phys. Rev. C*, 65:061601, 2002. 2.1.2.1, 2.2, 2.2.1, 5.3, 5.4
- [22] W. D. Hamilton, editor. *The Electromagnetic Interaction in Nuclear Spectroscopy*. North-Holland Pub. Co., Amsterdam, 1975. 2.1.3, 2.1.3
- [23] M. E. Rose. *Elementary Theory of Angular Momentum*. John Wiley & Sons, New York, 1957. 2.1.3
- [24] D. Bazin, R. J. Charity, R. T. de Souza, M. A. Famiano, A. Gade, V. Henzl, D. Henzlova, S. Hudan, J. Lee, S. Lukyanov, W. G. Lynch, S. McDaniel, M. Mocko, A. Obertelli, A. M. Rogers, L. G. Sobotka, J. R. Terry, J. A. Tostevin, M. B. Tsang, and M. S. Wallace. Mechanisms in Knockout Reactions. *Phys. Rev. Lett.*, 102:232501, 2009. 2.2.1, 5, 5.3
- [25] R. J. Glauber. *Lectures in Theoretical Physics*, volume 1, chapter High-Energy Collision Theory, page 315. Interscience Publishers, New York, 1959. 2.2.1
- [26] J. A. Tostevin. Single-nucleon knockout reactions at fragmentation beam energies. *Nucl. Phys. A*, 682:320c, 2001. 2.2.1, 2.2.1
- [27] B. A. Brown. New Skyrme interaction for normal and exotic nuclei. *Phys. Rev. C*, 58:220, 1998. 2.2.1
- [28] C. A. Bertulani and P. G. Hansen. Momentum distributions in stripping reactions of radioactive projectiles at intermediate energies. *Phys. Rev. C*, 70:034609, 2004. 2.2.1.1, 2.2.1.1

- [29] H. Esbensen. Momentum distributions in stripping reactions of single-nucleon halo nuclei. *Phys. Rev. C*, 53:2007, 1996. 2.2.1.1
- [30] C. A. Bertulani and A. Gade. MOMDIS: a Glauber model computer code for knockout reactions. *Computer Phys. Commun.*, 175:372, 2006. 2.2.1.1
- [31] D. J. Morrissey, B. M. Sherrill, M. Steiner, A. Stolz, and I. Wiedenhoever. Commissioning the A1900 projectile fragment separator. *Nucl. Inst. Meth. Phys. Res. B*, 204:90, 2003. 3.1.2, 3.2
- [32] J. D. Jackson. *Classical Electrodynamics*. John Wiley & Sons, Inc., New York, 1999. 3.1.2
- [33] J. Lindhard and A. H. Sørensen. Relativistic theory of stopping for heavy ions. *Phys. Rev. A*, 53:2443, 1996. 3.1.2, 3.3.1
- [34] D. Bazin, J. A. Caggiano, B. M. Sherrill, J. Yurkon, and A. Zeller. The S800 spectrograph. *Nucl. Inst. Meth. Phys. Res. B*, 204:629, 2003. 3.3, 3.2, 3.2.2.2
- [35] J. Yurkon, D. Bazin, W. Benenson, D. J. Morrissey, B. M. Sherrill, D. Swan, and R. Swanson. Focal plane detector for the S800 high-resolution spectrometer. *Nucl. Inst. Meth. Phys. Res. A*, 422:291, 1999. 3.2.2, 3.4, 3.2.2.1
- [36] Y. Fuchi, M. H. Tanaka, S. Kubono, H. Kawashima, and S. Takaku. High-Resolution, Two-Dimensional Focal-Plane Detectors for Intermediate-Energy Heavy Ions. In *Nuclear Science Symposium and Medical Imaging Conference, 1992., Conference Record of the 1992 IEEE*, volume 1, page 172, Oct 1992. 3.2.2.1
- [37] W. R. Leo. *Techniques for Nuclear and Particle Physics Experiments*. Springer-Verlag, New York, 2nd edition, 1994. 3.2.2.1, 3.3
- [38] K. Makino and M. Berz. COSY INFINITY computer software. [http://bt.pa.msu.edu/index\\_cosy.htm](http://bt.pa.msu.edu/index_cosy.htm), 2010. 3.2.2.2
- [39] M. Berz, K. Joh, J. A. Nolen, B. M. Sherrill, and A. F. Zeller. Reconstructive correction of aberrations in nuclear particle spectrographs. *Phys. Rev. C*, 47:537, 1993. 3.2.2.2
- [40] G. F. Knoll. *Radiation Detection and Measurement*. J. Wiley, New York, 3rd edition, 2000. 3.3
- [41] W. F. Mueller, J. A. Church, T. Glasmacher, D. Gutknecht, G. Hackman, P. G. Hansen, Z. Hu, K. L. Miller, and P. Quirin. Thirty-two-fold segmented germanium detectors to identify  $\gamma$ -rays from intermediate-energy exotic beams. *Nucl. Inst. Meth. Phys. Res. A*, 466:492, 2001. 3.3.1, 3.3.1, 3.16
- [42] O. B. Tarasov and D. Bazin. LISE++: Radioactive beam production with in-flight separators. *Nucl. Inst. Meth. Phys. Res. B*, 266:4657, 2008. 3.3.1

- [43] D. Bazin, O. Tarasov, M. Lewitowicz, and O. Sorlin. The program LISE: a simulation of fragment separators. *Nucl. Inst. Meth. Phys. Res. B*, 482:307, 2002. <http://groups.nsl.msu.edu/lise/lise.html>. 3.3.1
- [44] H. Weick. ATIMA computer software. <http://www-linux.gsi.de/~weick/atima>, 2010. 3.3.1
- [45] P. M. Endt. Energy levels of  $A = 21-44$  nuclei (VII). *Nucl. Phys. A*, 521:1, 1990. 3.3.1
- [46] Huo Junde. Nuclear Data Sheets for  $A = 56$ . *Nuclear Data Sheets*, 86:315, 1999. 3.1
- [47] D. Radford. RadWare computer software. <http://radware.phy.ornl.gov>, 2009. 3.3.2, 3.3
- [48] GEANT: Detector Description and Simulation Tool. *CERN Program Library Long Writup*, W5013, 1993. 3.3.3
- [49] A. Obertelli, A. Gade, D. Bazin, C. M. Campbell, J. M. Cook, P. D. Cottle, A. D. Davies, D.-C. Dinca, T. Glasmacher, P. G. Hansen, T. Hoagland, K. W. Kemper, J.-L. Lecouey, W. F. Mueller, R. R. Reynolds, B. T. Roeder, J. R. Terry, J. A. Tostevin, K. Yoneda, and H. Zwahlen. Population of bound excited states in intermediate-energy fragmentation reactions. *Phys. Rev. C*, 73:044605, 2006. 4.1
- [50] K. Yoneda, A. Obertelli, A. Gade, D. Bazin, B. A. Brown, C. M. Campbell, J. M. Cook, P. D. Cottle, A. D. Davies, D.-C. Dinca, T. Glasmacher, P. G. Hansen, T. Hoagland, K. W. Kemper, J.-L. Lecouey, W. F. Mueller, R. R. Reynolds, B. T. Roeder, J. R. Terry, J. A. Tostevin, and H. Zwahlen. Two-neutron knockout from neutron-deficient  $^{34}\text{Ar}$ ,  $^{30}\text{S}$ , and  $^{26}\text{Si}$ . *Phys. Rev. C*, 74:021303, 2006. 4.1
- [51] W. Benenson, J. Driesbach, I. D. Proctor, G. F. Trentelman, and B. M. Preedom. Energy Levels of  $^{25}\text{Si}$  from the Reaction  $^{28}\text{Si}(^3\text{He}, ^6\text{He})^{25}\text{Si}$  at 70.4 MeV. *Phys. Rev. C*, 5(4):1426, 1972. 4.2, 4.1, 4.2.2, 4.11, 5.1
- [52] R. B. Firestone. Nuclear Data Sheets for  $A = 25$ . *Nuclear Data Sheets*, 110(8):1691, 2009. 4.2, 4.1, 4.11
- [53] D. Morris and A. Volya. CoSMo. <http://cosmo.volya.net>, 2009. 4.1, 4.3
- [54] P. M. Endt. Supplement to energy levels of  $A = 21-44$  nuclei (VII). *Nucl. Phys. A*, 633:1, 1998. 4.3, 4.3, 4.23
- [55] J. S. Hanspal, K. I. Pearce, N. M. Clarke, R. J. Griffiths, R. E. Brown, R. A. Hardekopf, and W. Gruebler. The interaction of 17 MeV polarised tritons with  $^{30}\text{Si}$ . *Nucl. Phys. A*, 455:494, 1986. 4.23
- [56] T. Glasmacher. Coulomb excitation at intermediate energies. *Annu. Rev. Nucl. Part. Sci.*, 48:1, 1998. 5

- [57] J. M. Cook, T. Glasmacher, and A. Gade. Accuracy of  $b(e2; 0_1^+ \rightarrow 2_1^+)$  transition rates from intermediate-energy Coulomb excitation experiments. *Phys. Rev. C*, 73:024315, 2006. 5
- [58] J. Lee, J. A. Tostevin, B. A. Brown, F. Delaunay, W. G. Lynch, M. J. Saelim, and M. B. Tsang. Reduced neutron spectroscopic factors when using potential geometries constrained by hartree-fock calculations. *Phys. Rev. C*, 73:044608, 2006. 5.2, 5.3, 5.4
- [59] A. Gade, D. Bazin, B. A. Brown, C. M. Campbell, J. A. Church, D. C. Dinca, J. Enders, T. Glasmacher, P. G. Hansen, Z. Hu, K. W. Kemper, W. F. Mueller, H. Olliver, B. C. Perry, L. A. Riley, B. T. Roeder, B. M. Sherrill, J. R. Terry, J. A. Tostevin, and K. L. Yurkewicz. Reduced Occupancy of the Deeply Bound  $0d_{5/2}$  Neutron State in  $^{32}\text{Ar}$ . *Phys. Rev. Lett.*, 93:042501, 2004. 5.4
- [60] C. Aa. Diget, P. Adrich, D. Bazin, M. D. Bowen, B. A. Brown, C. M. Campbell, J. M. Cook, A. Gade, T. Glasmacher, K. Hosier, S. McDaniel, D. McGlinchery, A. Obertelli, L. A. Riley, K. Siwek, J. R. Terry, J. A. Tostevin, and D. Weisshaar. Structure of excited states in  $^{21}\text{Mg}$  studied in one-neutron knockout. *Phys. Rev. C*, 77:064309, 2008. 5.4
- [61] A. Gade, D. Bazin, B. A. Brown, C. M. Campbell, J. A. Church, D. C. Dinca, J. Enders, T. Glasmacher, P. G. Hansen, Z. Hu, K. W. Kemper, W. F. Mueller, H. Olliver, B. C. Perry, L. A. Riley, B. T. Roeder, B. M. Sherrill, J. R. Terry, J. A. Tostevin, and K. L. Yurkewicz. One-neutron knockout reactions on proton-rich nuclei with  $N=16$ . *Phys. Rev. C*, 69:034311, 2004. 5.4
- [62] J. Enders, A. Bauer, D. Bazin, A. Bonaccorso, B. A. Brown, T. Glasmacher, P. G. Hansen, V. Maddalena, K. L. Miller, A. Navin, B. M. Sherrill, and J. A. Tostevin. Single-neutron knockout from  $^{34,35}\text{Si}$  and  $^{37}\text{S}$ . *Phys. Rev. C*, 65:034318, 2002. 5.4
- [63] A. Gade, D. Bazin, C. A. Bertulani, B. A. Brown, C. M. Campbell, J. A. Church, D. C. Dinca, J. Enders, T. Glasmacher, P. G. Hansen, Z. Hu, K. W. Kemper, W. F. Mueller, H. Olliver, B. C. Perry, L. A. Riley, B. T. Roeder, B. M. Sherrill, J. R. Terry, J. A. Tostevin, and K. L. Yurkewicz. Knockout from  $^{46}\text{Ar}$ :  $\ell=3$  neutron removal and deviations from eikonal theory. *Phys. Rev. C*, 71:051301, 2005. 5.4
- [64] L. Riley, P. Adrich, T. R. Baugher, D. Bazin, B. A. Brown, J. M. Cook, P. D. Cottle, C. Aa. Diget, A. Gade, D. A. Garland, T. Glasmacher, B. A. Hartl, K. E. Hosier, K. W. Kemper, A. Ratkiewicz, K. P. Siwek, D. C. Stoken, J. A. Tostevin, and D. Weisshaar. Selectivity of the one-neutron knockout reaction on  $^{45}\text{Cl}$  and the collapse of the  $N=28$  shell closure. *Phys. Rev. C*, 79:051303, 2009. 5.4
- [65] L. A. Riley, P. Adrich, T. R. Baugher, D. Bazin, B. A. Brown, J. M. Cook, P. D. Cottle, C. Aa. Diget, A. Gade, D. A. Garland, T. Glasmacher, K. E. Hosier, K. W. Kemper, A. Ratkiewicz, K. P. Siwek, J. A. Tostevin, and D. Weisshaar. Rotational and neutron-hole states in  $^{43}\text{S}$  via the neutron knockout and fragmentation reactions. *Phys. Rev. C*, 80:037305, 2009. 5.4

- [66] J. R. Terry, D. Bazin, B. A. Brown, J. Enders, T. Glasmacher, B. M. Sherrill, and J. A. Tostevin. Absolute spectroscopic factors from neutron knockout on the halo nucleus  $^{15}\text{C}$ . *Phys. Rev. C*, 69:054306, 2004. 5.4
- [67] J. Lee, M. B. Tsang, D. Bazin, D. Coupland, V. Henzl, D. Henslova, M. Kilburn, W. G. Lynch, A. M. Rogers, A. Sanetullaev, A. Signoracci, Z. Y. Sun, M. Youngs, K. Y. Chae, R. J. Charity, H. K. Cheung, M. Famiano, S. Hudan, P. O'Malley, W. A. Peters, K. Schmitt, D. Shapira, and L. G. Sobotka. Neutron-Proton Asymmetry Dependence of Spectroscopic Factors in Ar Isotopes. *Phys. Rev. Lett.*, 104:112701, 2010. 5

## BIOGRAPHICAL SKETCH

### **Robert R. Reynolds, Jr.**

Robert R. Reynolds, Jr. was born on January 13, 1981, in Gainesville, Georgia. He graduated from North Hall High School in the Spring of 1999. He received his Bachelor of Science degree in physics from North Georgia College and State University in May of 2003. He began graduate school at The Florida State University in the Fall of 2003, where he studied nuclear physics under Dr. Paul Cottle. Robert graduated with a Masters of Science from The Florida State University in August of 2007, and upon a successful dissertation defense, he was awarded his Doctor of Philosophy degree in August of 2010.